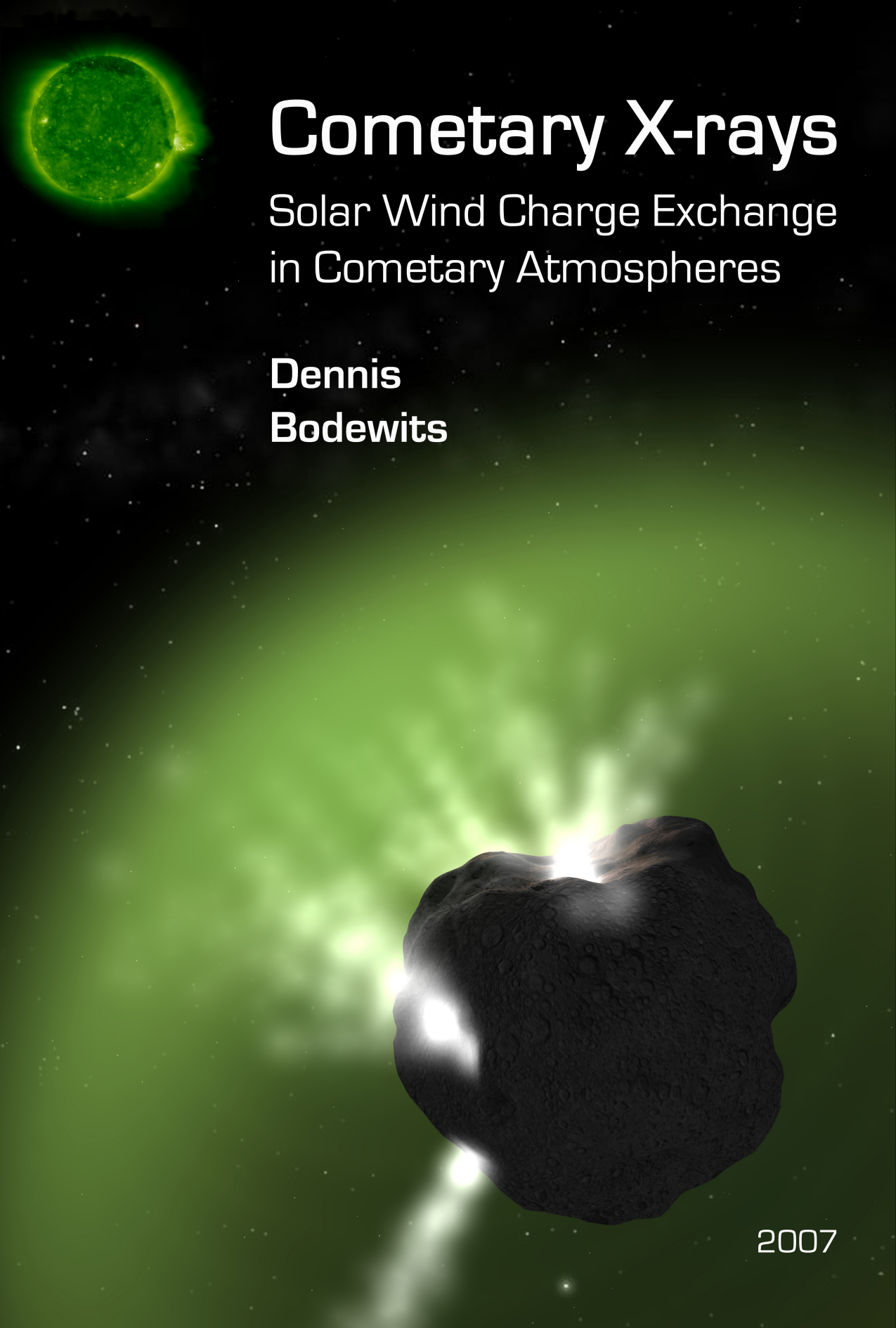

Cometary X-rays

Solar Wind Charge Exchange in Cometary Atmospheres

Dennis Bodewits

2007

RIJKSUNIVERSITEIT GRONINGEN

Cometary X-rays

Solar Wind Charge Exchange in Cometary Atmospheres

Proefschrift

ter verkrijging van het doctoraat in de
Wiskunde en Natuurwetenschappen
aan de Rijksuniversiteit Groningen
op gezag van de
Rector Magnificus, dr. F. Zwarts,
in het openbaar te verdedigen op
vrijdag 8 juni 2007
om 13:15 uur

door

Dennis Bodewits

geboren op 28 augustus 1979
te Hoogezand–Sappemeer

Promotores:	Prof. dr. ir. R. Hoekstra Prof. dr. A. G. G. M. Tielens
Beoordelingscommissie:	Prof. dr. R. W. McCullough Prof. dr. R. Morgenstern Prof. dr. E. F. van Dishoeck

ISBN: 9789036729499 Printed version
ISBN: 9789036729505 Electronic version

COVER: Artist impression of the X-ray emission following solar wind charge exchange with the neutral gas ejected by the comet's nucleus. Cover design by Tibor Balint.

This work is sponsored by the 'Stichting voor Fundamenteel Onderzoek der Materie' (FOM) which is financially supported by the 'Nederlandse organisatie voor Wetenschappelijk Onderzoek' (NWO).

PRINTED BY: Drukkerij Alba, Groningen

Contents

1 Introduction

Highly charged ions are amongst if not the most reactive species in the universe. These ions are produced in hot gases of several millions of degrees. When colliding with a neutral gas, the ions are neutralized via charge exchange reactions. These interactions are therefore a key aspect in many astrophysical environments. In the solar system, collisions between a hot plasma and a neutral gas occur when the solar wind interacts with planets, moons, comets and the in streaming neutral interstellar medium. Charge exchange processes might also occur around other stars with even more violent stellar winds, in planetary nebulae (e.g. interaction of the fast post Asymptotic Giant Branch wind with the slowly-moving wind), when supernova remnants interact with the interstellar medium (e.g. the venting of supernova remnants into the lower galactic halo) and on a truly galactic scale, the interaction of winds - associated with starbursts - with the interstellar medium.

Charge exchange reactions are quasi-resonant processes, and depend strongly on properties of both the neutral and the ionized gas. The resulting emission therefore provides a unique window on their interactions. As such, charge exchange emission (CXE) has an important application in controlled fusion experiments, as both Doppler shifts of CXE lines and their absolute and relative intensities can provide information on local plasma parameters such as temperatures, velocities and abundances and charge state of the interacting plasmas (Isler, 1994; von Hellermann et al., 1991; Hoekstra et al., 1998; Anderson et al., 2000).

1.1 Cometary X-ray and EUV emission

X-ray and Extreme Ultraviolet (EUV) emission is usually associated with high temperature environments. The discovery that comets are bright emitters in this spectral regime was therefore a big surprise (Lisse et al., 1996; Mumma et al., 1997), because comets are generally considered dirty snowballs surrounded by a gaseous coma with a temperature of approximately 50 K. After the first discovery by ROSAT of the X-ray emission from comet C/1996 B2 (Hyakutake), a search through the observatory's archives proved that in fact all comets in the inner solar system (≤ 3 AU) were emitting X-rays (Dennerl et al., 1997). The total X-ray power in the 0.2 – 1.0 keV band was between 0.2 – 1 GW, the emission was

highly variable in time and many of the observed comets displayed a characteristic crescent shape.

To explain these surprising observations, numerous possible scenarios were proposed. Amongst them were scattering/fluoresence of solar X-rays (Krasnopolsky, 1997), thermal bremsstrahlung associated with collisions of solar wind electrons with cometary neutral gas or dust (Bingham et al., 1997; Northrop et al., 1997; Uchida et al., 1998), electron/proton K- and L-shell ionization (Krasnopolsky, 1997), and Rayleigh-scattering of solar X-rays by attogram dust particles (Wickramasinghe and Hoyle, 1996; Owens et al., 1998; Schulz et al., 2000) and charge exchange between highly ionized solar wind minor ions and cometary neutral species (Cravens, 1997). A thorough comparative study by Krasnopolsky (1997) demonstrated that none of these mechanisms except for the charge exchange emission (CXE) model could account for more than 5% of the observed luminosities.

The launch of a new generation of X-ray observatories (*Chandra* and XMM-*Newton*) allowed for a definitive answer of the comet-X-ray enigma. The observations of comet C/1999 S4 (LINEAR) in July 2000 demonstrated the presence of carbon and oxygen emission lines in the comet's X-ray spectrum, thereby underpinning the CXE mechanism (Lisse et al., 2001).

Before space probes that to monitor the solar wind became available, cometary ion tails were the only solar wind probes in space. Even nowadays, they largely remain so for regions outside the ecliptic plane. Cometary X-rays in particular have proven to be excellent probes to study solar wind – neutral gas interactions, because comets have no magnetic field and the wind therefore interacts directly with the neutral gas surrounding the nucleus, the coma. Secondly, the size of the cometary atmosphere (in the order of $10^4 - 10^5$ km) allows remote tracking of the ions as they penetrate into the comet's atmosphere, offering a close-up view on the interaction of the two plasmas. Thirdly, since the first observations of cometary X-ray emission, more than 20 comets have been observed with various X-ray and Far-UV observatories (Lisse et al., 2004; Krasnopolsky et al., 2004). This observational sample contains a broad variety of comets, solar wind environments and observational conditions. The observations clearly demonstrate that cometary charge exchange emission provides a wealth of diagnostics, which are visible as spatial, temporal and spectral emission features.

First of all, the emission morphology is a tomography of the distribution of neutral gas around the nucleus (Wegmann et al., 2004), see Fig. 1.1. In active comets, the X-ray emission clearly maps a spherical gas distribution. This resulted in a characteristic crescent shape for the larger and hence collisionally thick comets, observed at phase angles of roughly 90 degrees. Good examples are the observations of the comets Hyakutake (Lisse et al., 1996), LINEAR S4 (Lisse et al., 2001) and C/2000 WM1 (Wegmann and Dennerl, 2005). Macroscopic features of the plasma interaction such as the bow shock are observable, too (Wegmann and Dennerl, 2005). In less active comets, gaseous structures in the collisionally thin parts of the coma brighten, as is illustrated in Fig. 1.1 for the jets in 2P/2003 (Encke) (Lisse et al., 2005). The morphology of the emission is not crescent-like, but maps the optical coma, which was faint and dominated by a sunward fan composed of two bright jets. Other examples are the Deep Impact triggered plume in 9P/Tempel 1 (Lisse et al., 2007) and the unusual morphology of comet 6P/d'Arrest (Mumma et al., 1997).

Secondly, by observing the temporal behavior of the comet's X-ray emission, the ac-

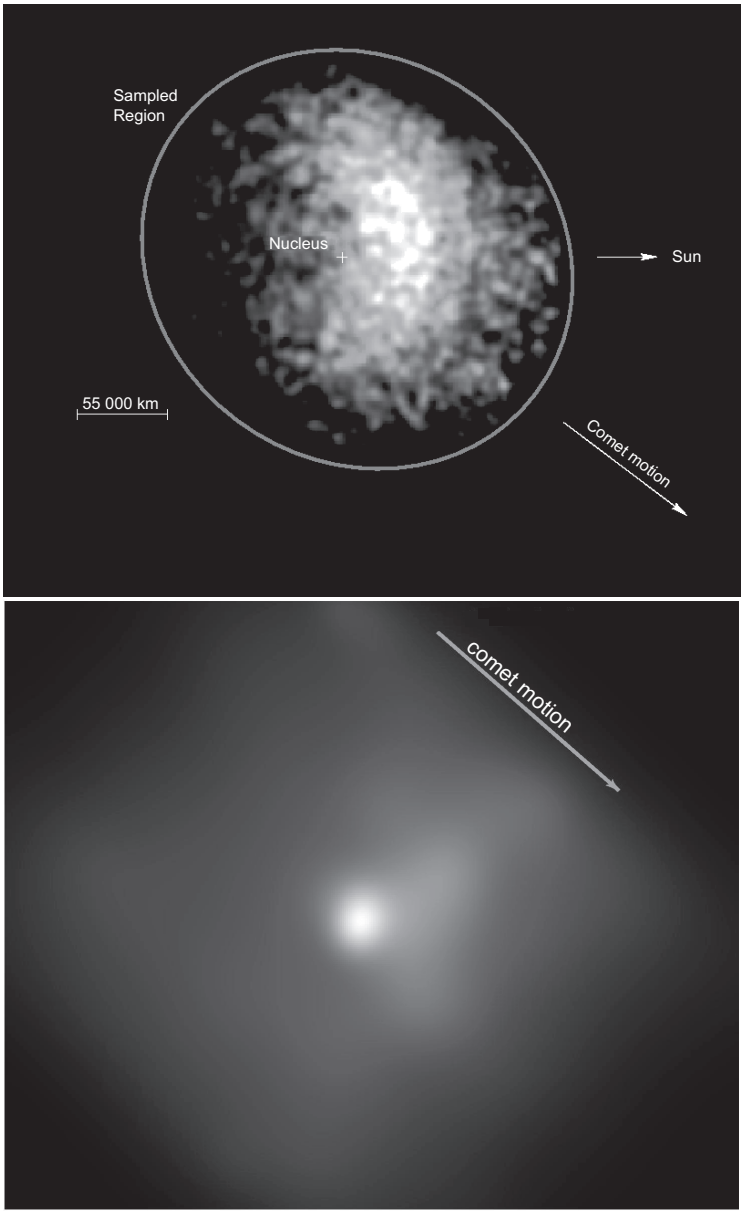

Figure 1.1: ***Top panel:*** *Comet Hyakutake in 1996, observed with ROSAT (Lisse et al., 1996). The comet produced enormous amounts of gas during the observations and was therefore collisionally thick for solar wind ions, resulting in a characteristic crescent shape.* ***Bottom panel:*** *Chandra X-ray image of comet 2P/2003 (Encke) from Lisse et al. (2005). The nucleus is in the center of the image. The image in lower panel corresponds to a square of* 9×10^4 *km on the sides, the image in the upper panel is 7.5 times larger. In both images, the direction to the Sun is approximately towards the right.*

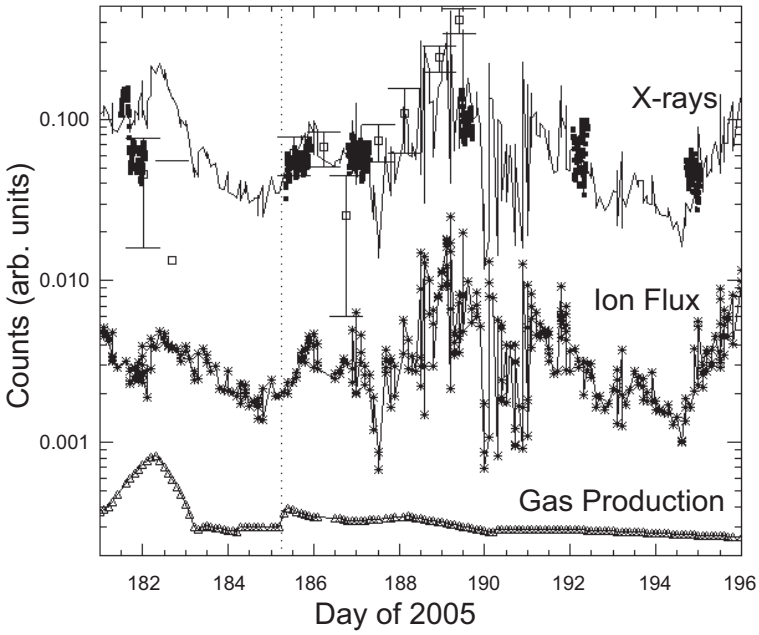

Figure 1.2: *X-ray light curve of comet 9P/2005 (Tempel 1) for the period June 30 – July 14, 2005, observed by Chandra (■–Lisse et al., 2007) and Swift (□–Willingale et al., 2006) in the 0.3 – 1.0 keV band. The light curve follows the combined temporal behavior of neutral gas (comet gas production, △) and solar wind ion flux (⋆). This product is indicated with a solid line. All parameters are plotted on an arbitrary scale.*

tivity of the solar wind and comet can be monitored. This was first shown for comet C/1996 B2 (Hyakutake) (Neugebauer et al., 2000) and recently in great detail by long term observations of comet 9P/2005 (Tempel 1) (Willingale et al., 2006; Lisse et al., 2007) and 73P/2006 (Schwassmann-Wachmann 3C) (Brown et al., prep), where cometary X-ray flares could be assigned to either cometary outbursts and/or solar wind enhancements (see Fig. 1.2).

Thirdly, cometary spectra reflect the physical characteristics of the solar wind; e.g. spectra resulting from either fast, cold (polar) wind and slow, warm equatorial solar wind should be clearly different (Schwadron and Cravens, 2000; Kharchenko and Dalgarno, 2001; Bodewits et al., 2004). Several attempts were made to extract ionic abundances from the X-ray spectra. The first generation spectral models have all made strong assumptions when modeling the X-ray spectra (Haberli et al., 1997; Wegmann et al., 1998; Kharchenko and Dalgarno, 2000; Schwadron and Cravens, 2000; Lisse et al., 2001; Kharchenko and Dalgarno, 2001; Krasnopolsky et al., 2002; Beiersdorfer et al., 2003; Wegmann et al., 2004; Bodewits et al., 2004; Krasnopolsky, 2004; Lisse et al., 2005). Because many different analytical methods were used, it has been very difficult to study the existing spectra compar-

atively.

1.2 Thesis Outline

This thesis discusses the diagnostic use of charge exchange emission, in particular applied to the interaction between comets and the solar wind. In Chapter 2, an overview is given of the fundamental concepts of comets, the solar wind, and their interaction. In Chapter 3, the main charge exchange processes relevant to comet – solar wind interactions are introduced and explained by means of the Classical Over-the-Barrier and Bohr-Lindhard models. In Chapter 4, the experimental set up is described, together with the main features of the experimental techniques used throughout this thesis. Experimental results for collisions between solar wind ions and species which are abundant in the inner coma of cometary atmospheres are presented in Chapters 5 – 7. In Chapter 8, an interaction model is introduced which uses state selective electron capture cross sections to predict and explain cometary charge exchange emission. This model is then applied to EUV (Chapter 9) and X-ray observations (Chapter 10). Finally, a summary and outlook are given in Chapter 11.

2 Comets and the Solar Wind

Cometary X-ray and Far UV emission depend on properties of the comet and solar wind, and on the characteristics of their interaction. This chapter presents a brief overview of the fundamental concepts relevant in cometary and solar wind studies. In Chapter 8, these will be used as the foundations of our comet-wind interaction model.

2.1 Solar Wind

The solar wind is the expansion of the solar corona into the interplanetary medium. Every second, approximately 10^9 kg of material is ejected by the Sun as solar wind. Around Earth, the solar wind consists of circa 9 protons, 10 electrons and 0.5 alpha-particles per cm^3. It also contains a small fraction of heavier ions (C, N, O, Ne, ...). They pass Earth with an average velocity of 450 km s^{-1}. To most people, the solar wind is best known for its harmless manifestation in the northern light. The Sun's solar wind may have been about 1000 times more massive in the distant past, which must then have affected the history of our solar system. It has even been suggested that Mars' atmosphere has been eroded by the solar wind. Nowadays, space weather effects can still disrupt power grids, disturb radio communication, cause the failure of spacecraft electronics or impose a health hazard for astronauts or even airline passengers.

The solar wind was first predicted when in the early 50's, Biermann (1951) and others tried to explain the kinematics of cometary ion tails. In the next decades, space exploration led to the actual discovery of the solar wind and many experiments were performed to measure its composition and its temporal and spatial behavior. Currently, the solar wind is continuously monitored by a small armada of space crafts. SOHO and ACE are positioned at the Lagrangian point L1, roughly one million kilometers upstream the solar wind, and provide real time solar wind data such as the proton velocity and density, but also compositional data on helium and minor ions. *Ulysses*, launched in 1990, orbits the Sun in a polar orbit and thus measures latitudinal structures in the wind. Recently, the STEREO instrument was launched, which will provide accurate observations of the outflow directions of coronal mass ejections.

The solar wind is a collisionless plasma of which the composition and charge state

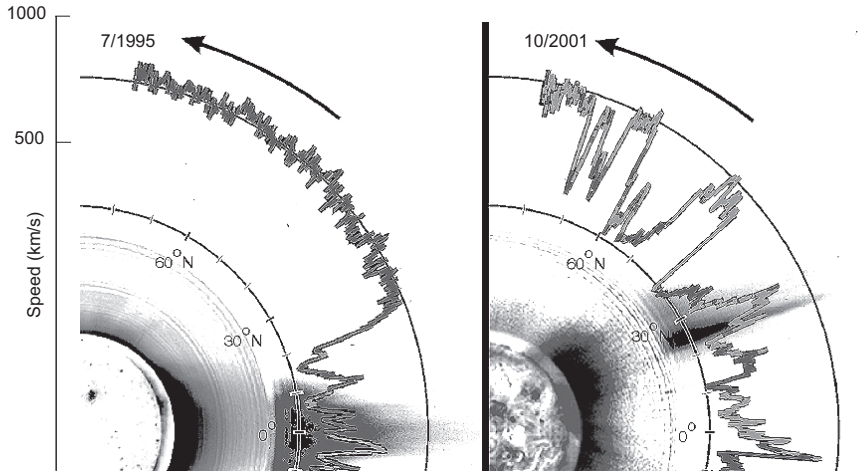

Figure 2.1: *Solar wind velocities during solar minimum (**left panel**) and maximum (**right panel**). During most of the solar cycle, the wind is organized in a bimodal structure with slow, variable wind around the helioequator and fast, steady wind at higher latitudes. During solar maximum, the slow irregular wind is dominant at all latitudes (Courtesy of Southwest Research Institute and the Ulysses/SWOOPS team).*

are frozen in within a few solar radii from the Sun. The composition of the solar wind is therefore a measure of its source region. A parameter often used is the freeze-in (or freezing-in) temperature of two charge states of an ionic species. This quantity is defined as the electron temperature at which the abundance ratio of two neighboring charge states is in ionizational/recombinational equilibrium (Hundhausen et al., 1968). This freeze-in temperature is different for each element, because due to different ionization and recombination time scales, their charge states are frozen in in different parts of the corona. For

Table 2.1: *Characteristics of the two types of solar wind, after Axford and McKenzie (1997).*

Parameter	Slow wind	Fast wind
Speed	300-400 km s^{-1}	700 – 800 km s^{-1}
Density	10 cm^{-3}	3 cm^{-3}
Flux	3×10^8 cm^{-2} s^{-1}	2×10^8 cm^{-2} s^{-1}
Structure	highly variable	uniform, slow changes only
He/H	1-30%	5%
Minor ions	highly variable	almost constant
T_f (O^{7+}/O^{6+})	1.2 – 1.7 MK	$\leq$ 1.2 MK
Coronal source	Streamer belt	Coronal holes
Latitude at minimum	$\leq 15°$	$> 30°$
Latitude at maximum	all latitudes	less common, often transient

ion pairs of the same element however, a single freeze-in temperature often describes the charge state distribution well (Geiss et al., 1995).

During solar minimum, the solar wind is organized in a bimodal structure with a slow, 300 km s^{-1} wind around the solar equator, and a fast, 700 km s^{-1} wind at latitudes above 30 degrees that is associated with polar coronal holes. This is illustrated in Fig. 2.1, which summarizes solar wind velocities measured by the *Ulysses* spacecraft. The fast and slow wind not only differ in velocity, but also in their charge state composition, reflecting the different origins of these wind types. The different properties of the two wind types are summarized in Table 2.1. The freeze-in temperature T_f (O^{7+}/O^{6+}) for the fast wind is approximately 1.2 MK and relatively constant. For the slow wind, it is around 1.7 MK and highly variable (Geiss et al., 1995; Zurbuchen et al., 2002). The fast, polar wind is thus 'colder' than the slow, equatorial wind and its heavy ions are on average of lower charge state than those in the equatorial wind.

Looking in more detail to the solar wind, this simple bimodal picture turns out to be more complex. During solar minimum, the slow wind is highly variable and structured. Coronal holes around the equator eject streams of faster wind, which are generally slower than the polar fast wind. When these streams interact with the slow (background) solar wind, corotating interaction regions (CIRs) are formed. In addition, bubbles of gas and energy called coronal mass ejections (CMEs), shooting away from the Sun in any direction, provide very hot, very fast streams of solar wind. During solar maximum, the bimodality seems to disappear completely and although the general condition of the wind resembles that of the slow wind around solar minimum, the 3D structure of the solar wind is chaotic and highly variable. Also, CMEs are far more common around solar maximum.

2.1.1 Corotational Mapping

The two solar wind observatories ACE and SOHO are both located near Earth, at its Lagrangian point L1 (roughly 10^6 km upstream the solar wind). In order to get an idea about local solar wind conditions at the position of a comet, the solar wind information obtained by the space probes needs to be extrapolated to the position of the comet, i.e. the time difference between solar wind observation and the actual interaction with a distant comet, has to be determined. A first approximation for this time difference is described by Neugebauer et al. (2000). Their calculations are based on the comet ephemeris, the location of L1 and the measured wind speed. With this procedure, the time difference between an element of the corotating solar wind arriving at L1 and at the comet (or of any object of interest) can be predicted. Structures in the solar wind move radially outward, but also follow the rotation of the Sun, which rotates around its axis in 27 days (T_{sun}). This results in an Archimedean spiral, and the time shift Δt between comet and L1 has a radial and corotational component:

$$\Delta t = \Delta t_{rad} + \Delta t_{rot} \tag{2.1}$$

where the radial time shift Δt_{rad} is determined by the radial separation between comet and L1, Δd, and the velocity of the solar wind, v_{sw}:

$$\Delta t_{rad} = \frac{\Delta d}{v_{sw}} \tag{2.2}$$

The velocity of the comet is negligible, because it is very low compared to the speed of the solar wind. The corotational time shift Δt_{rot} is found by dividing the heliolongitudinal separation of comet and L1 (ΔLon) by the rotational frequency of the Sun:

$$\Delta t_{rot} = \frac{T_{sun} \Delta Lon}{2\pi} \tag{2.3}$$

This method works well for a quiet, smooth solar wind interacting with a comet near to Earth. However, a disadvantage of this procedure is that it cannot account for latitudinal structures in the wind or the magnetohydrodynamical behavior of the wind (i.e. the propagation of shocks and CMEs). These shortcomings imply that especially for comets observed at large longitudinal, latitudinal and/or radial separations from the observatories located at L1, the solar wind data is at best an estimate of the local wind conditions.

2.2 Comets

Comets are generally considered dirty snowballs, sized 1 – 15 km and consist of a mixture of non-volatile ices and frozen grains. Close encounters with spacecraft showed irregularly shaped bodies, with surfaces that suggest a complex history of wearing, collisions and chemical processing (Fig. 2.2). Comets that revolve around the Sun in less than 200 y are called 'short period' comets, those with longer orbital periods are referred to as 'long period' comets. Long period comets are classically associated with the Oort-cloud (Oort, 1950), a reservoir at at least 10^3 AU from the Sun that has been estimated to contain between 10^{11} – 10^{12} cometary nuclei, with a total mass between 1-50 earth masses (Stern, 2003; Dones et al., 2004). Short period comets originate in the Kuiper belt (Kuiper, 1951), which starts beyond Neptune (30 AU) and hosts many different objects, amongst which the dwarf planets Pluto and its moon Charon. This second reservoir is more disc-like and as a consequence, comets from the Kuiper-belt typically have lower inclinations (<30°) than comets from the spherical Oort-cloud.

When a comet approaches the Sun, gases start to sublimate from the nucleus, forming a cloud of gas and dust known as the coma. Because the comet's gravity is far too weak to bind these gases, the atmosphere expands until the gases are ionized or fragmented by sun light.

Depending on its outgassing activity, the comet will form its characteristic tails. Usually, two tails can be distinguished; a white dust tail, from scattered sun light, and a blueish ion tail from fluorescence processes. Dust particles in the dust tail are pushed out of the coma by light pressure and the tail is curved according to Keplerian mechanics. The kinematics of the ion tail were not understood until the discovery of the solar wind by Biermann (1951). The solar wind sweeps up ions from the coma and blows them in an almost straight tail, which therefore always points away from the Sun. Ionic tails can extend over more than 1 AU. The interaction between comets and wind is discussed in depth in the next section.

Due to their storage far away from the Sun, comets might provide access to pristine material from the early days of the solar system. Also, comets have been suggested as potential sources of life on Earth. Comets have therefore attracted a lot of scientific attention,

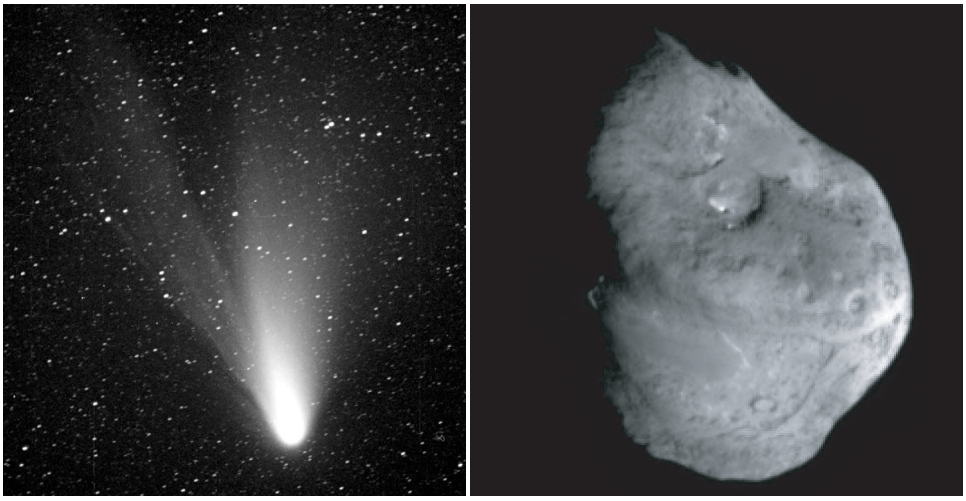

Figure 2.2: ***Left panel:*** *Comet Hale-Bopp in 1996. The ion tail (left) and dust tail (right) can clearly be distinguished.* ***Right panel:*** *The nucleus of comet Tempel 1, five minutes before it was impacted by the Deep Impact probe. Image from NASA/UM (A'Hearn, 2005).*

resulting in several dedicated space missions in the last two decades. In 1986, a number of spacecraft such as ESA's *Giotto* flew by comet Halley. The *Giotto* probe provided the first images of a cometary nucleus (Keller et al., 1986), and constituted much of our current knowledge concerning the interactions between comets and the solar wind.

In July 2005, the Deep Impact (DI) mission provided the first look inside a comet by having a 385 kg copper core colliding with the nucleus of comet 9P/Tempel. The DI mission yielded very high resolution imagery of the surface of comet Tempel 1 (Fig. 2.2) and allowed for remote spectroscopy of subsurface material excavated by the impact (A'Hearn, 2005). A big question raised by DI concerns the origin of the sublimating gas. DI provided the first direct detection of water ice on the surface of a comet, but the total area covered with ice is too small to explain the outgassing of Tempel 1 (Sunshine, 2006). The European *Rosetta* mission will address this question by landing on the surface of comet 67P/Churyumov-Gerasimenko in 2014.

2.2.1 Cometary Atmospheres

As comets approach the Sun, they develop a coma from sublimating gases, mainly water with some CO (< 30%) and CO_2 (< 10%) and small traces of other species. The gases produced directly by the nucleus are referred to as parent species and flow out radially until they are photo-ionized or -dissociated by solar UV flux. At 1 AU, typical lifetimes are around 10^5 s, but these lifetimes vary greatly amongst species (Huebner et al., 1992). Empirically, outflow velocities of parent molecules have been determined to scale with the comet's distance to the Sun, r_h (in AU) as $v = 0.85 r_h^{-0.5}$ km s^{-1}. The products of the fragmentation of parent molecules are called daughter species, and when in turn these

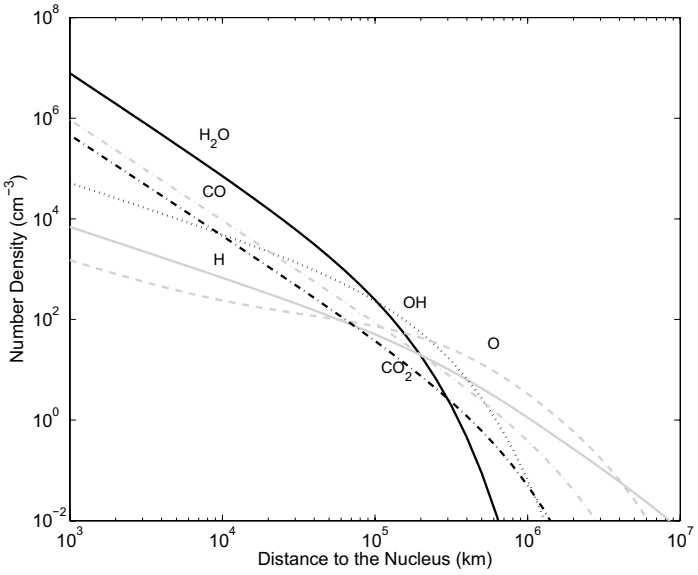

Figure 2.3: *Density distribution in a comet with gas production of Q=10^{29} molecules s^{-1} at 1 AU from the Sun, according to the Haser model (see text).*

fragments are dissociated, they produce granddaughter species.

The most relevant case for cometary atmospheres is the destruction of water (parent) into H and OH (daughters), and subsequently, O and H (granddaughters):

$$\begin{aligned} H_2O + \nu &\rightarrow OH + H + 3.42\ \text{eV} && (1.03\times10^{-5}\ \text{s}^{-1}) \\ &\rightarrow H_2 + O(^1D) + 3.84\ \text{eV} && (5.97\times10^{-7}\ \text{s}^{-1}) \\ &\rightarrow H + H + O + 0.7\ \text{eV} && (7.55\times10^{-7}\ \text{s}^{-1}) \\ &\rightarrow H_2O^+ + e + 12.4\ \text{eV} && (3.31\times10^{-7}\ \text{s}^{-1}) \end{aligned}$$

where reaction rates at 1 AU, for quiet Sun conditions, are given between brackets (Huebner et al., 1992). The first of these reaction paths, where the water molecule breaks apart into hydroxyl and atomic hydrogen, is the most likely channel, with a branching ratio of 86%. After the break up, the kinetic energy release of 3.42 eV yields velocity kicks of 1.5 km s^{-1} for the OH molecule, and 26 km s^{-1} for the H atom (Combi et al., 2004), hence ejecting the latter out of the inner coma to form a large hydrogen halo surrounding the comet.

$$\begin{aligned} OH + \nu &\rightarrow O(^3P) + H + 1.27\ \text{eV} && (6.54\times10^{-6}\ \text{s}^{-1}) \\ &\rightarrow O(^1D) + H + 7.90\ \text{eV} && (6.35\times10^{-7}\ \text{s}^{-1}) \\ &\rightarrow OH^+ + e + 19.1\ \text{eV} && (2.47\times10^{-7}\ \text{s}^{-1}) \end{aligned}$$

Just like the initial water molecule, the OH molecule is most likely to photo-dissociate and its reaction products are again accelerated. The cometary atmosphere then expands until the atomic products O and H are finally photo ionized.

The spatial distribution of neutral molecules and atoms in cometary atmospheres can be approached by means of the Haser model (Haser, 1957; Festou, 1981). The Haser model assumes a point source with a constant and isotropic gas production rate. The density of a parent molecule (e.g. water) is described by:

$$n(r) = \frac{Q}{4\pi v r^2} \exp\left(-\frac{r}{v\tau_P}\right) \tag{2.4}$$

where Q denotes the production rate of the relevant parent species, v is this species' outflow velocity, r is the distance to the nucleus and τ_P is the lifetime of the species in the solar UV field. The product of outflow velocity and lifetime is called the scale length of the molecule β_P:

$$\beta_P = (v\tau_P)^{-1} \tag{2.5}$$

The density of the molecules R originating from the dissociation of molecules P is:

$$n_R^P(r) = \frac{Q_P}{4\pi v_R r^2} \frac{\beta_P^D}{\beta_R - \beta_P} \left(e^{-\beta_P r} - e^{-\beta_R r}\right) \tag{2.6}$$

where β_P^D is the total destruction scale length of the parent molecule and where the velocity v_R is the average velocity for the daughter species, found by summing the outflow velocity and the velocity kick from the dissociation process at right angles. The number density of the products of the second dissociation, the granddaughter products S which are produced from daughter product R, is given by:

$$n_S^R(r) = \frac{Q_P}{4\pi v_S r^2} \cdot \left(Ae^{-\beta_P r} + Be^{-\beta_S r} + Ce^{-\beta_R r}\right) \tag{2.7}$$

where the coefficients A, B and C are:

$$A = \frac{-\beta_P \beta_P^D}{(\beta_P - \beta_R)(\beta_S - \beta_P)} + \frac{\beta_P^D}{\beta_S - \beta_P} \tag{2.8}$$

$$B = \frac{-\beta_P \beta_P^D}{(\beta_R - \beta_P)(\beta_S - \beta_P)} + \frac{\beta_P^D \beta_R}{(\beta_R - \beta_P)(\beta_S - \beta_R)} - \frac{\beta_P^D}{\beta_S - \beta_P} \tag{2.9}$$

$$C = -A - B \tag{2.10}$$

An example of a neutral density distribution in the coma of an active comet at 1 AU from the Sun is shown in Fig. 2.3. Up to 10^5 km from the nucleus, the coma is dominated by water molecules, whereas further outward the most abundant species are its dissociation products H, OH and O. CO has a much longer lifetime in solar UV fluxes, so that it becomes relatively more abundant in the outer parts of the coma.

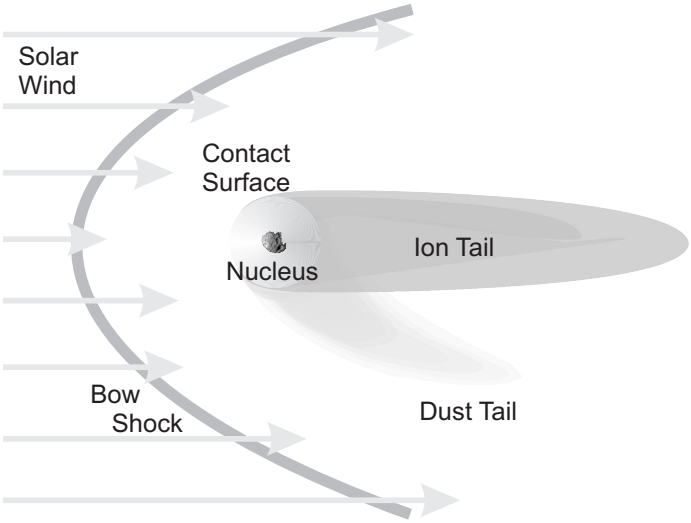

Figure 2.4: *Schematics of the interaction of solar wind and a cometary atmosphere. Scales vary in the figure; the nucleus is 1 – 10 km, the bow shock is situated at ~ 10^6 km from the nucleus, the contact surface at ~ 10^3 km. The large atomic hydrogen halo surrounding the comet is not indicated.*

2.3 Comet-Wind Interaction

When the solar wind first interacts with the ions in the outer coma, a bow shock is created. The solar wind can only digest a certain amount of cometary pick up ions, and when a critical mass is exceeded a bow shock occurs which transforms the parallel supersonic solar wind flow into a divergent subsonic flow. In this bow shock, the solar wind ions are decelerated and heated at the same time. The charge state composition of the wind is not affected in the shock. As an example, during the *Giotto* encounter, comet Halley interacted with a slow 390 km s^{-1} wind, and its bow shock was found to be located at approximately 10^6 km upstream the nucleus (Neubauer et al., 1986; Goldstein et al., 1987).

The stand off distance of the bow shock, R_{bs}, can be estimated by using a rule of thumb derived by Wegmann et al. (2004), which describes the pick up of newly generated cometary ions. The solar wind can only digest a certain amount of cometary ions. When a critical mass is exceeded, a bow shock occurs at a distant R_{bs} from the nucleus:

$$R_{bs} \geq (\gamma^2 - 1)\frac{\alpha m_C Q}{4\pi v F(\infty)} \tag{2.11}$$

where γ is the adiabatic index ($\gamma = 5/3$), $F(\infty)$ is the initial solar wind mass flux, Q is the comet's gas production rate, v is the velocity of the out flowing gas, m_C is the average mass of a cometary ion and α is the average ionization rate of a cometary ion (Schmidt and Wegmann, 1982).

As the wind further penetrates into the comet's atmosphere, it gradually picks up more and more slow cometary ions, meanwhile loosing initial fast protons that get neutralized

by charge exchange processes. The *Giotto* results showed that this mass loading leads to deceleration, or cooling, of the wind down to velocities of ~50 km s^{-1} (Goldstein et al., 1987).

While the bow shock limits the free flowing solar wind, the contact surface is the boundary between pure cometary gases and the solar wind in the inner parts of the coma. Within the contact surface, there is no magnetic field and its extent in case of comet Halley was 4700 km (Neubauer et al., 1986). The plasma experiments on board *Giotto* found that the interaction region between bow shock and contact surface is highly structured. This structuring is still poorly understood.

Highly charged ions are only a minor constituent of the solar wind and play no prominent role in the macroscopic interaction between comets and the solar wind. When these ions collide on neutral atoms or molecules in the coma, they are neutralized via charge exchange reactions. For these reactions, cross sections are more than an order of magnitude larger than those of protons, and therefore interaction ranges for highly charged ions interacting with the comet can extend far beyond the bow shock. X-ray observations of comets have demonstrated that via charge exchange emission, the interaction between comets and the solar wind becomes directly visible.

3 Charge Exchange

Charge exchange is a process in which one or more electrons are transferred from one particle to another, and it is the dominant reaction between ions and neutrals up to collision velocities of several hundreds of kilometers per second. The net reaction is:

$$A^{q+} + B \rightarrow A^{(q-r)+} + B^{(r+s)+} + se^{-} \tag{3.1}$$

Here A is an ion with charge q, that captures r electrons from an initially neutral target B. This target is left with a charge $r+s$ as s electrons are lost to the continuum. The dominant reaction channel in most charge transfer reactions is single electron capture (SEC), where one electron is captured from the target into an excited state of the projectile ion, i.e. $(r,s) = (1,0)$. The excited state subsequently decays to the ground state by the emission of one or more photons. As will be demonstrated in the experimental chapters of this thesis, multiple-electron processes can be an important reaction channel in collisions between highly charged ions and molecules. An important reaction channel is double capture with $(r,s) = (2,0)$, where two electrons are captured by the projectile. This can lead to the population of doubly excited states, which most likely decay by the emission of an Auger-electron (auto-ionizing double capture, A2C), or which can radiatively stabilize (bound double capture, B2C). Note that the A2C reaction leads to $(r,s) = (1,1)$.

The probability P that charge exchange occurs when an ion traverses through a gas is generally expressed in terms of the cross sections σ_j of the different charge exchange processes:

$$P = \sum_j \sigma_j \int dr\, n(r) \tag{3.2}$$

where the integral is taken along the path of the ion through a gas with number density $n(r)$. The cross sections are typically in the order of $10^{-16} - 10^{-14}$ cm^2, depending on the gas and ion combination.

3.1 Bohr-Lindhard Model

A first classical description of one electron capture was proposed by Bohr and Lindhard (1954). It is based on classical relations between the forces and energies of the collision

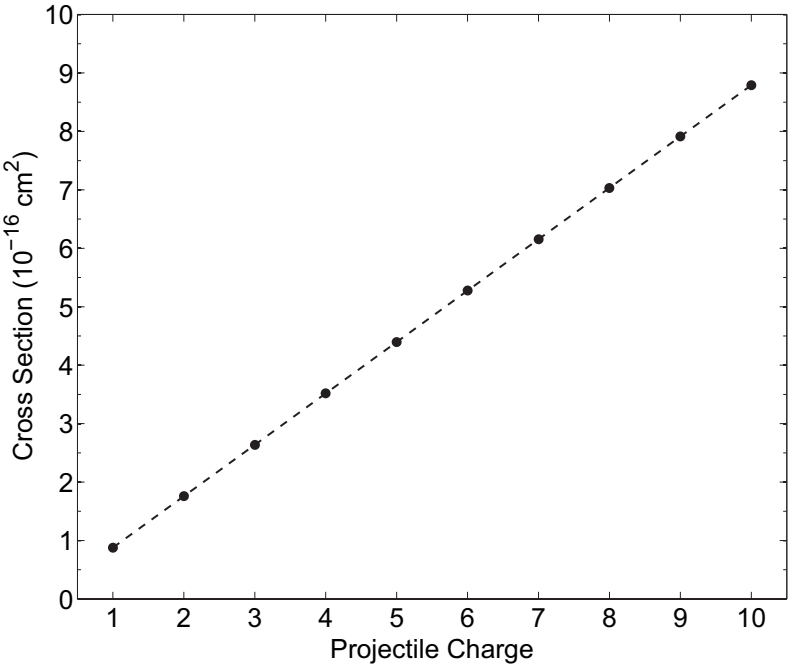

Figure 3.1: *One electron capture cross sections from atomic hydrogen, for ions with increasing charge q, as predicted by the Bohr-Lindhard model.*

system. Two critical distances are introduced for an ion approaching a neutral target. At the first distance, R_1, the coulomb force from the charge q of the projectile attracting the electron is equal to the binding force in the neutral target[1]:

$$\frac{q}{R_1^2} = \frac{2I_b}{a} \tag{3.3}$$

$$R_1 = \sqrt{\frac{aq}{2I_b}} = \frac{\sqrt{aq}}{v_e} \tag{3.4}$$

where v_e is the orbital velocity, I_b the binding energy and a the orbital radius of the target electron. The electron can be captured by the projectile when in the projectile frame, its potential energy is larger than its kinetic energy. This occurs when target and projectile get within the second critical distance R_2:

$$\frac{q}{R_2} = \frac{1}{2}v^2 \qquad \text{hence} \qquad R_2 = \frac{2q}{v^2} \tag{3.5}$$

[1]Throughout this chapter, atomic units are used for convenience. See Appendix A for their definition and conversion

where v is the collision velocity of the projectile. When $R_1 < R_2$, the electron is immediately captured when it is released and the geometrical electron capture cross section is given by:

$$\sigma = \pi R_1^2 = \pi \frac{aq}{2I_b} \tag{3.6}$$

Note that this implies that for velocities below the critical velocity v_c, given by:

$$v_c = \left(\frac{8I_b q}{a}\right)^{\frac{1}{4}} \tag{3.7}$$

the cross section is independent of the projectile velocity, but that for higher velocities, $R_1 > R_2$ - the electron is released before it can be captured by the projectile. If the release process would occur instantaneously, electron capture would be impossible and the cross section would become zero. However, the release takes a finite amount of time and occurs with a probability of v_e/a per unit time. Therefore, there is a chance that the electron is still not released when the projectile is within the capture distance R_2. The probability of electron release within a distance R_2 is determined by the product of the release probability per unit time (v_e/a) and the time during which capture can take place (R_2/v). Thus for $R_1 > R_2$, the electron capture cross section is given by:

$$\sigma = \pi R_2^2 \left(\frac{v_e}{a} \cdot \frac{R_2}{v}\right) = 8\sqrt{2}\pi q^3 \sqrt{I_b} a^{-1} v^{-7} \tag{3.8}$$

At velocities below v_c, the Bohr-Lindhard model thus predicts cross sections that are dependent on the charge of the projectile and the binding energy of the target, but not of the collision velocity. Above velocities v_c, the cross section decreases strongly with increasing velocity.

Resulting charge exchange cross sections for capture from atomic hydrogen by projectiles with increasing charge are shown in Fig. 3.1. For the orbital radius a, expectation values of the radial probability density are used, using hydrogenic wavefunctions with an effective nuclear charge Z_{eff}:

$$< 1/r >^{-1} = n^2/Z_{eff} \tag{3.9}$$

With a maximum acceleration voltage of 24 kV (see Chapter 4), all collisions discussed in this thesis fall within the low velocity regime of the Bohr-Lindhard model.

3.2 Classical Over-the-Barrier Model

The Classical Over-the-Barrier model (COB) is a comprehensible approximation for collisions between ions and neutrals at energies in the range of 100 eV/amu up to 10 keV/amu. It allows for estimates of electron capture cross sections, and the principal quantum number n into which the electron is captured. The COB model describes reactions of the type:

$$A^{q+} + B \rightarrow A^{*(q-r)+} + B^{r+} \tag{3.10}$$

where A^{q+} is the projectile ion with charge q, which captures r electrons from a neutral target B.

The model is based on the idea that if the projectile approaches a target close enough, the electron can freely move in their joint potential well, called a quasi-molecular state. This occurs when the height of the potential barrier between the two nuclei is lower than the binding energy of the target electron. At an infinite separation $R = \infty$, the neutral's least bound electron has a (negative) binding energy I_b. The approaching ion's Coulomb field causes a Stark shift which increases the electron's binding energy:

$$I_b(R) = I_b(\infty) - \frac{q}{R} \tag{3.11}$$

where R is the internuclear distance. The full potential experienced by an electron at a distance r of the target nucleus is the sum of the potential of the ion and that of the target:

$$V(r) = -\frac{q}{|R-r|} - \frac{1}{|r|} \qquad \text{for} \qquad 0 < |r| < |R| \tag{3.12}$$

The top of the barrier is reached for exactly that r where the derivative of this equation equals zero. Solving this equality yields both the position r_{max} and the magnitude V_{max} of the top of the potential barrier:

$$\frac{dV(r)}{dr} = \frac{-q}{(R-r)^2} + \frac{1}{r^2} = 0 \tag{3.13}$$

$$r_{max} = \frac{R}{\sqrt{q}+1} \tag{3.14}$$

$$V_{max} = -\frac{q}{R} - \frac{1+2\sqrt{q}}{R} = -\frac{(\sqrt{q}+1)^2}{R} \tag{3.15}$$

The electron can escape from the target when V_{max} becomes smaller than the binding energy of the electron:

$$-\frac{q}{R} - \frac{1+2\sqrt{q}}{R} = I_b(\infty) - \frac{q}{R} \tag{3.16}$$

which yields a capture distance R_c at which charge exchange can occur:

$$R_c = \frac{2\sqrt{q}+1}{-I_b(\infty)} \tag{3.17}$$

From this distance, the cross section for the one electron capture process can be determined by assuming that if ions pass the neutral at a distance smaller than this critical distance R_c, the electron is captured with unit probability. The electron capture cross section is then given by the geometrical cross section, weighted with the capture probability A:

$$\sigma = \pi R_c^2 = \pi\Big(\frac{2\sqrt{q}+1}{I_b(\infty)}\Big)^2 \tag{3.18}$$

A value of $A = 0.5$ has been determined from both theory (Baede, 1975) and experiments (Dijkkamp et al., 1985).

In the COB, it is assumed that during the quasi-molecular state, the binding energy of the electron remains fixed. On the way out, the potential barrier starts to increase again.

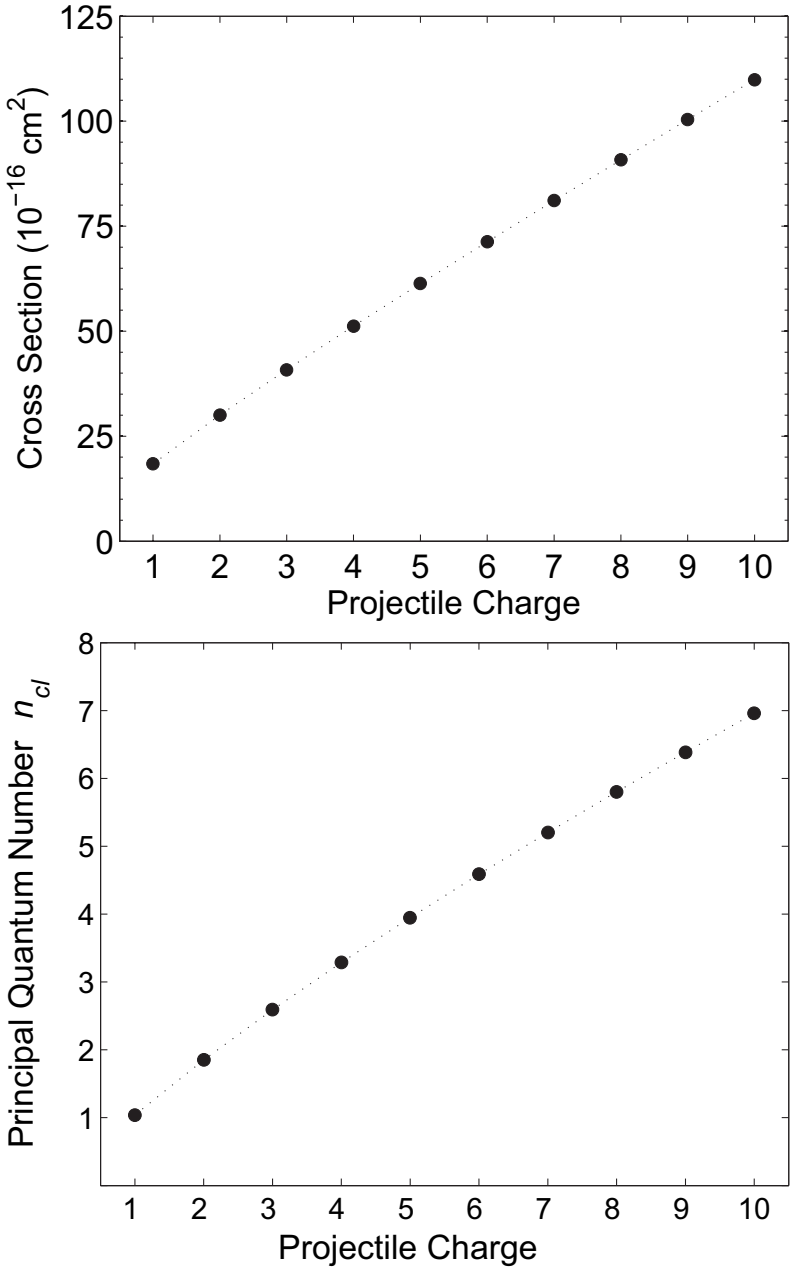

Figure 3.2: *Classical Over-the-Barrier predictions for collisions between ions with charge q and H_2O molecules.* ***Top panel:*** *Capture cross sections.* ***Bottom panel:*** *'Classical' principal quantum number n_{cl} into which the electron is likely to be captured.*

The binding energy I_f of the captured electron at infinitive R equals its energy at the barrier crossing, lowered by the Stark shift induced by the (now charged) target:

$$I_f = I_b(R_c) + \frac{1}{R_c} = I_b - \frac{q-1}{R_c} \tag{3.19}$$

Electron capture thus results in an increase of the binding energy of the captured electron. This binding energy can be used to predict the state n into which the electron is most likely to be captured. This can be done by converting the binding energy I_f into a 'classical' energy level n_{cl} by the hydrogenic approximation:

$$n_{cl} = \frac{q}{\sqrt{|2I_f|}} \tag{3.20}$$

Although the Classical Over-the-Barrier model does not give an exact distribution over the n-states, the availability of states near the predicted binding energies may give information on the effectiveness of certain electron capture processes. If the decimal fraction of n_{cl} is between 0.5 – 0.8 the actual n distribution strongly depends on the collision energy.

COB predictions for ions typical for the solar wind colliding on a H_2O molecule are shown in Fig. 3.2. The principal quantum number into which the electron the electron is captured increases steadily with increasing projectile charge q, from $n = 1-7$ for $q = 1-10$. The cross section increase approximately linear with the projectile charge and ranges from $18 - 110\times10^{-16}$ cm^2 for projectiles with $q = 1 - 10$.

As an example of the COB, consider the collision of O^{7+} + H_2O, which is described experimentally in Chapter 7. A cartoon of the COB interaction of this system is shown in Fig. 3.3. Initially, the electron is bound in the target molecule with $I_b = 12.6$ eV. At an internuclear distance of $R_c = 13.6$ a.u. (7.2 Å), the electron can cross the potential barrier. This capture distance is equivalent to a capture cross section of 81×10^{-16} cm^2. Its binding energy at the capture distance is $I_b(R_c) = 26.6$ eV. Upon separation, the final binding energy of the electron in the projectile $I_f = 24.6$ eV. Following Eq. 3.20, this results in $n = 5.2$. The most likely principal quantum shell into which the electron is captured is thus the $n = 5$ state.

3.2.1 Multiple Electron Capture

Analogue to single electron capture in the previous section, the COB model can also be applied to multiple electron capture processes (Ryufuku et al., 1980; Niehaus, 1986). When the projectile ion approaches the neutral target, the electrons subsequently enter the quasi-molecular state. The potential experienced by the i^{th} electron is:

$$V_i^{in}(r) = \frac{q}{|R-r|} - \frac{i}{|r|} \tag{3.21}$$

resulting in a transit distance for the i^{th} electron given by:

$$R_i^{in} = \frac{i + 2\sqrt{iq}}{-I_{b,i}(\infty)} \tag{3.22}$$

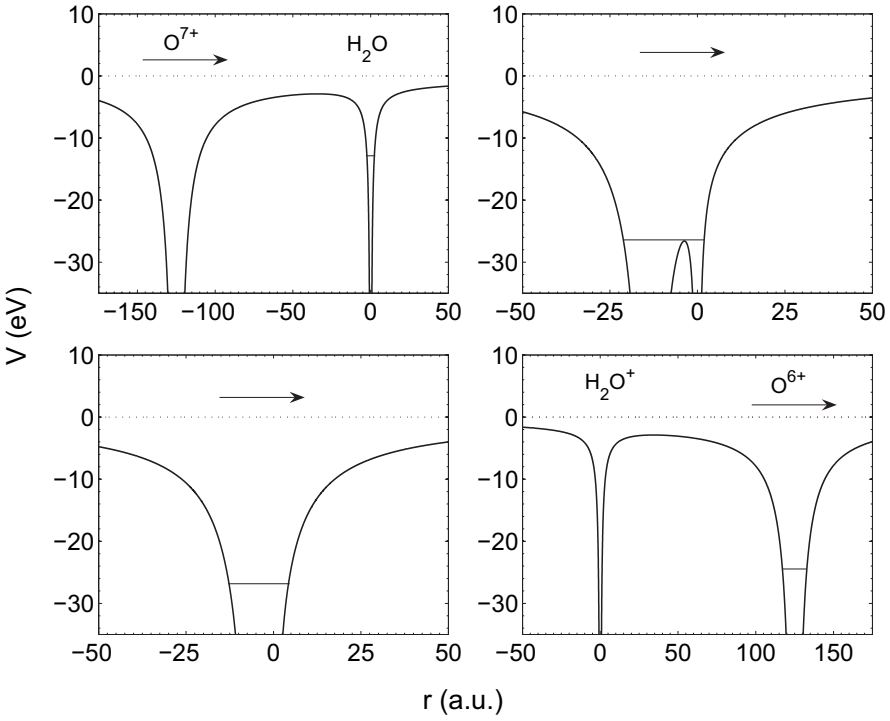

Figure 3.3: *The Over-the-Barrier model for an O^{7+} ion colliding on a neutral H_2O molecule.* ***Upper left panel:*** *The ion approaches the water molecule. When the ion approaches the molecule, the potential barrier between the two is lowered.* ***Upper right panel:*** *At a distance of R_{in}=13.6 a.u. (~ 7.2 Å), the potential barrier becomes lower than the binding energy of the outermost electron of the target.* ***Lower left panel:*** *The electron is in a quasi-molecular state.* ***Lower right panel:*** *On the way out, at a distance of R_{out}=13.6 a.u. (~ 7.2 Å), the quasi-molecular electron is either captured by the projectile ion or recaptured by the target molecule.*

where $I_{b,i}(\infty)$ is the binding energy of the i^{th} target electron at infinite internuclear separation. On the way out, these electrons are assumed to be sequentially captured by the projectile, or recaptured by the target. As in the one electron model, these capture processes occur at the distance where the potential barrier equals the binding energy of the quasi-molecular electron $I_{b,i}(R_i^{in})$:

$$R_i^{out} = R_i^{in}\left(\frac{\sqrt{q-j}+\sqrt{i+c}}{\sqrt{q}+\sqrt{i}}\right)^2 \tag{3.23}$$

where c is the number of already captured electrons at the moment of capture of the i^{th} electron (by either projectile or target). If the electron is captured by the projectile, its final

binding energy at infinite internuclear separation is:

$$I_{f,i} = I_{b,i}(\infty) - \frac{q}{R_i^{in}} + \frac{i+c}{R_i^{out}} = I_{b,i}(\infty)\left(1+\delta(q,i,c)\right) \tag{3.24}$$

where $\delta(q,i,c)$ is defined as:

$$\delta(q,i,c) \equiv \frac{1}{i+2\sqrt{iq}}\left(q - \left(\frac{\sqrt{q}+\sqrt{i}}{1+\sqrt{\frac{q-c}{i+c}}}\right)^2\right) \tag{3.25}$$

The geometrical cross sections for capture of the i^{th} electron capture is now a shell, delimited by the transit distances of the i^{th} and the next $(i+1)^{\text{th}}$ electron, weighted by the capture probability A_i:

$$\sigma_i = A_i \pi \left((R_i^{in})^2 - (R_{i+1}^{in})^2\right) \tag{3.26}$$

To illustrate this, consider a two electron process for O^{7+} colliding on H_2O. The first electron still becomes quasi-molecular at 13.6 a.u. Using a vertical double ionization energy of 41 eV (Alvarado et al., 2005) for the H_2O molecule yields $R_2^{in} = 9.6$ a.u. On the way out, the 2nd electron is captured first (at 9.6 a.u.) and will be bound with a binding energy of 41.2 eV. The other electron is captured at $R_1^{out} = 15.3$ a.u., and bound with 23.1 eV. Note that this is slightly less than in the one electron case, as a result of the larger Stark shift of the ionized target. The geometric cross section for one electron capture is 41×10^{-16} cm^2, and for double electron capture 40×10^{-16} cm^2. Based on the COB model, it is to be expected that for collision between O^{7+} and H_2O, bound double capture is as likely as single electron capture.

3.2.2 Reaction Window

The discussion above assumes that an electron is captured resonantly; the detailed inner structure of the projectile is considered to match the binding energy of the electron(s) from the target perfectly. In practice, this is not the case.

There is an uncertainty in the binding energy due to the finite time Δt an electron needs to cross the potential barrier. If this time interval is short, the uncertainty in the binding energy is determined by the Heisenberg uncertainty principle. For longer time intervals, the uncertainty is given by the change barrier height. In this way, the Extended Over-the-Barrier model predicts a Gaussian distribution of binding energies around the most probable final binding energy, called the reaction window. The distribution around the final binding energy for an electron i is assumed to be a Gaussian distribution with a standard deviation given by:

$$\Delta I_{f,i} = \sqrt{0.5\cdot\left((\Delta V_i^{in})^2 + (\Delta V_i^{out})^2\right)} \tag{3.27}$$

The assumption is made that this classical uncertainty in the barrier height is equal to the quantum mechanical uncertainty

$$\Delta V \Delta t \sim 1 \tag{3.28}$$

The radial velocity v_{rad} of the projectile, i.e. the component of the projectile velocity along the internuclear axis, determines how fast the potential barrier will raise in the finite time Δt it takes an electron to cross the barrier results in an uncertainty in the barrier height ΔV, which can be expressed as:

$$\Delta V = \frac{dV}{dR} \cdot v_{rad} \cdot \Delta t \tag{3.29}$$

so that a minimum uncertainty is given by:

$$(\Delta V)^2 = \frac{dV}{dR} \cdot v_{rad} \tag{3.30}$$

For simplicity, we will consider here an interaction system in which only the outer two electrons are involved. Both on the way in and on the way out, there is an internuclear distance R at which the height of the potential barrier is equal to the shifted binding energy. Substitution of these distances gives:

$$\frac{dV_i^{in}}{dR}\Big|_{R_i^{in}} = \left(\frac{\sqrt{q}+\sqrt{i}}{R_i^{in}}\right)^2 \tag{3.31}$$

$$\frac{dV_i^{out}}{dR}\Big|_{R_i^{out}} = \left(\frac{\sqrt{q-c}+\sqrt{i}}{R_i^{out}}\right)^2 \tag{3.32}$$

The radial velocity v_{rad} is related to the projectile velocity v_p and the impact parameter b by:

$$v_{rad} = v_0 \cdot \sqrt{1-\left(\frac{b}{R_i}\right)^2} \tag{3.33}$$

Niehaus (1986) originally used the radial velocity at the smallest impact parameter possible for the considered electron capture process. Hoekstra et al. (1991) however proposed to use the radial velocity averaged over all internuclear distances for which the electrons can cross the potential barrier, which is a more accurate approach. In that way the average velocities at R_i^{in} and R_i^{out} are found to be:

$$\bar{v}_{rad,i}^{in} = \frac{2}{3} v_p \left(\frac{R_i^{in}}{R_{i+1}^{in}}\right)^2 \left\{1-\left(1-\left(\frac{R_{i+1}^{in}}{R_i^{in}}\right)^2\right)^{\frac{3}{2}}\right\} \tag{3.34}$$

$$\bar{v}_{rad,i}^{out} = \frac{2}{3} v_p \left(\frac{R_i^{out}}{R_{i+1}^{in}}\right)^2 \left\{1-\left(1-\left(\frac{R_{i+1}}{R_i^{out}}\right)^2\right)^{\frac{3}{2}}\right\} \tag{3.35}$$

The reaction window can now be expressed as:

$$W_i(E) = \frac{1}{\sqrt{\pi}\cdot\Delta I_{f,i}} \exp\left(-\left(\frac{E+I_{f,i}}{\Delta I_{f,i}}\right)^2\right) \tag{3.36}$$

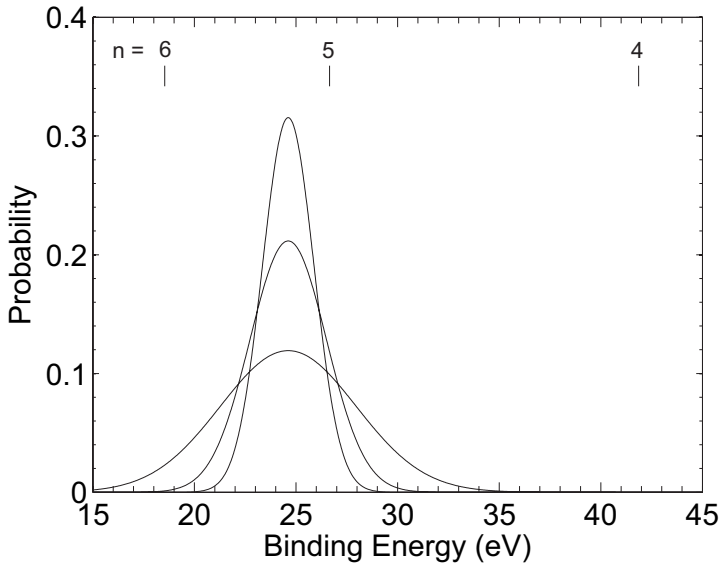

Figure 3.4: *Widening of the reaction window with increasing velocity, for single electron capture by O^{7+} from a H_2O molecule. Velocities of 0.2, 1.0 and 10 keV/amu were used and the position of the excited OVII n-shells are indicated.*

The reaction window can be used to roughly predict the distribution of final states of the ion that are populated by considering the overlap between the reaction window and the binding energies of the final ionic states. The reaction window widens as the velocity increases with a $v_p^{1/2}$ dependence so that for larger velocities, more states can be populated.

This is illustrated in Fig. 3.4 for one electron capture by O^{7+} from H_2O. Capture occurs almost resonantly into the $n = 5$ channel. At higher collision energies however, the reaction window widens and capture into $n = 6$ also becomes possible. These findings are indeed confirmed by experiments described in Chapter 7.

4 Experiment

For more than two decades, fusion research has been a strong incentive to study charge transfer reactions. The discovery of solar wind charge exchange emission in cometary atmospheres triggered great interest in astrophysically relevant collision systems, i.e. atmospheric gases such as H_2O, CO and CO_2. More recently, the experimental focus has shifted to even more complex biologically relevant molecules and clusters, with the aim of understanding ion induced radiation damage (see e.g. Alvarado et al., 2005; Schlathölter et al., 2006).

State selective electron capture processes can be studied by different techniques, and each of them particular advantages. A rough distinction between applied methods would be along the observed reaction product:

- **Photons**: Photon Emission Spectroscopy (PES) is the method used in this thesis. It allows for the measurement of state selective cross sections by detection of the photons that are emitted subsequent to the charge exchange reaction (Hoekstra et al., 1991; Lubinski et al., 2001). The advantage of this method is its high resolution, allowing for resolving the population of different ℓ-states. However, electron capture into the ground state cannot be observed, and the calibration of the spectrometers used is not trivial.

- **Projectile**: Translational Energy Spectroscopy (TES) is a method that uses the kinetic energy that the projectile gains or looses in the charge exchange reaction. The forward scattering energy change corresponds to the difference in electronic binding energy before and after the interaction. The TES technique allows to distinguish different reaction channels such as dissociative and non-dissociative electron capture (Kearns et al., 2002; Kamber et al., 2002). Charge exchange reactions leading to neutralization of the incident projectile cannot be observed.

- **Target (fragments):** Recoil Ion Momentum Spectroscopy (RIMS) is based on measurement of the momenta of the ionized target. In principle, this technique allows to completely resolve the collision dynamics of collision systems so that differential cross sections can be obtained. At the KVI, this technique is used in combination with a magneto-optical trap (see e.g. Turkstra et al., 2001; Knoop et al., 2005).

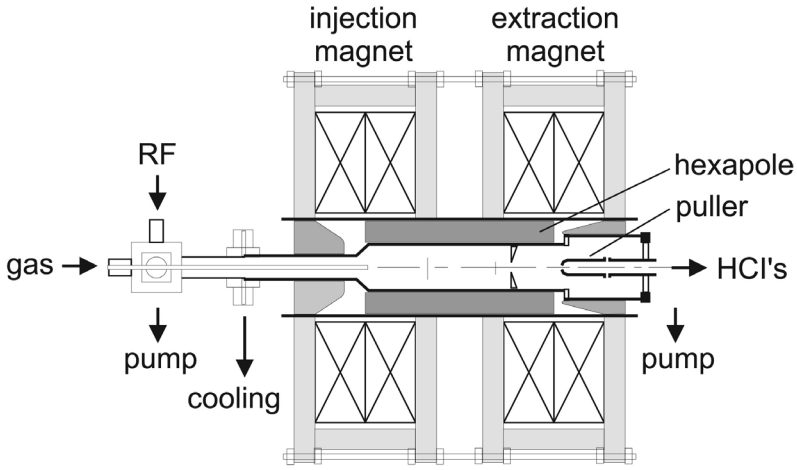

Figure 4.1: *Schematic drawing of the ECRIS at the KVI-atomic physics group. Neutral gas is let in on the left, and is ionized by electrons heated by an RF field. The ions are extracted to the right.*

4.1 ECRIS

The experiments described in this thesis were done in the Atomic Physics group, at the KVI-University of Groningen. In the Atomic Physics group, a number of experimental set ups share an Electron Cyclotron Resonance Ion Source (ECRIS – Drentje, 1985), which produces the highly charged ion beams used for the study of the interaction of highly charged ions with various physical systems.

In an ECRIS, a plasma is confined by a magnetic trap, at the KVI consisting of a radial field from a permanent hexapole magnet and a longitudinal field from two coils (see Fig. 4.1). Electrons gyrate around the magnetic field lines with a cyclotron frequency ω_c and are heated by applying a resonant radio frequency field, approximately 14 GHz. Electron impact driving the ionization of the gas injected into the ECRIS and high charge states are achieved by repeated electron collisions. The maximum charge available is limited by the increasing amount of energy required to strip ions any further and by recombination processes.

The entire ECRIS is floating on high voltage (3 – 24 kV), and ions are extracted using a puller lens, to which a negative potential can be applied to enhance the extraction of low energy or low charge state ions.

After the ions are extracted from the source, they are selected by a 110° bending magnet according to their mass per charge ratio m/q. The selected ions are then guided through a beam line by means of three sets of quadrupole triplet magnets, until a final 45° bending magnet is used to bend the ion beam into the experimental set up.

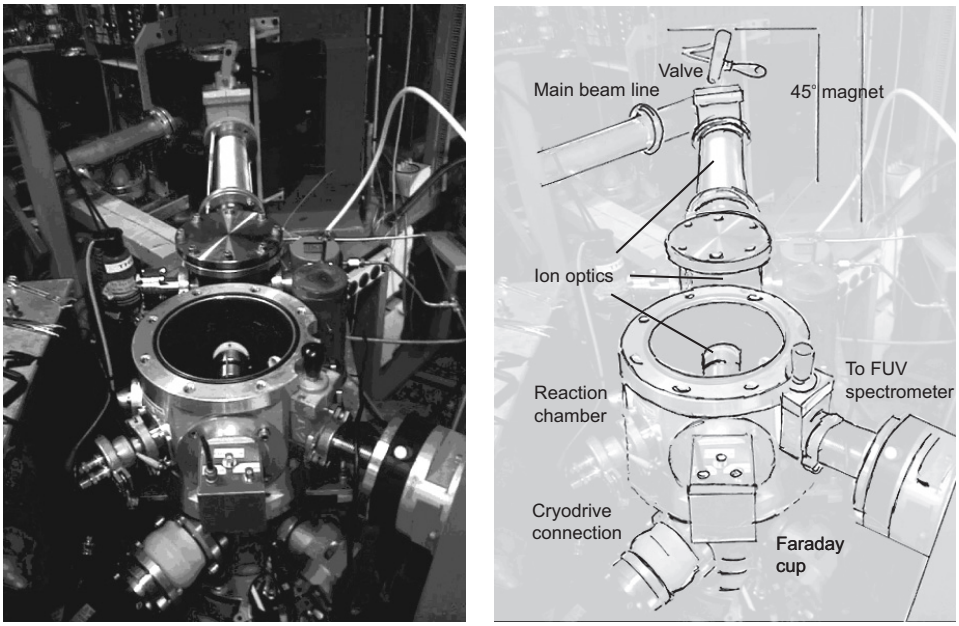

Figure 4.2: *The AGORA set up. In the top of the photo, the main beam line and 45° magnet are just visible. The ion beam then enters the main reaction chamber, where it is decelerated and focussed by ion optics. The EUV spectrometer is placed on the right (only partly visible), and the gas inlet is completely mounted on the top flange, that was removed here.*

4.2 AGORA Experiment

The Photon Emission Spectroscopy (PES) studies described in this thesis are done with the AGORA set up. A sketch of the AGORA set up is shown in Fig. 4.2. Ions from the ECRIS are guided into a large, cylindrical reaction chamber, where they cross a supersonic gas jet let in by a nozzle. The collision center of these two beams is observed by a EUV spectrometer that can be equipped with different gratings, according to the spectroscopic needs of the collision system of interest.

The reaction chamber and beam line are differentially pumped to ensure single collision conditions, and the back ground vacuum was kept around 10^{-6} mbar during the experiments. The nozzle was movable up and down, and in the direction perpendicular to the beam, allowing for optimization of the overlap and hence the resulting photon yield. By moving the nozzle perpendicularly through the ion beam, we were able to estimate the width of the gas jet at its crossing with the ions to be 3.5 mm FWHM. For the targets, commercially available pure gases were used. The water vapor target was prepared specifically to avoid contamination by gases dissolved in the water. A reservoir filled with demineralized water was repeatedly cooled with liquid nitrogen and pumped; in this way the water vapor contains much less than 1% of air molecules (Alvarado et al., 2005). The pressure of the in streaming gas was controlled with a needle valve, and monitored by an absolute

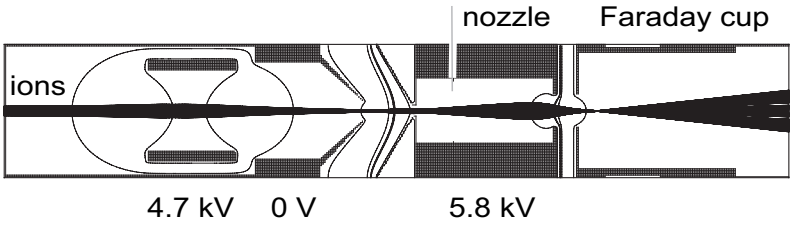

Figure 4.3: *Simulation of the ion guiding into the AGORA set up. The ions, entering from the left, are focussed and decelerated by a set of three electrostatic lenses. The ions then cross the gas jet, injected by a nozzle that is kept on the same high potential as the lens it is embedded in. The beam current is monitored by a Faraday cup (on the right). A typical configuration is shown, where He^{2+} ions extracted with 6 kV from the ECRIS are decelerated to 200 V.*

pressure head. During the course of a day of experiments, the gas pressure was usually stable within a few percent. For water, this was slightly worse and the system required heating to 50° C to prevent pressure instabilities due to condensation.

After a first set of experiments (Chapter 5), the set up was equipped with additional ion optics to enable collision energies below the ECRIS' minimal energy ($3q$ keV). This allowed for velocity depend collision studies in the full range of velocities relevant to the interaction between comets and the solar wind. A schematic outline of the ion optics, including a simulated ion beam is shown in Fig. 4.3. The lens system enabled deceleration down to approximately 200 V. At lower voltages, the ion beam would blow up and not all ions would be captured in the Faraday cup.

4.2.1 EUV Spectrometer

In the collisions between highly charged ions and target molecules, electrons are captured quasi-resonantly into excited states of the ions. The relaxation of these states goes along with the emission of one or more photons, which in our experiment were observed with an EUV spectrometer. The EUV spectrometer used here was a grazing incidence spectrometer, sensitive in the 5 – 84 nm band. Light incident on a gold coated grating is projected onto a Rowland circle with a radius of 1.5 m. By using different gratings, various angles of incidence and certain entrance slit widths the resolution as well as the bandwidth of the instrument can be varied. For the helium experiments, a 600 G/mm grating was used, for the other experiments a 1200 G/mm grating. A position sensitive micro channel plate detector could be moved along the Rowland circle and allows for the simultaneous detection of lines within approximately 10 – 20 nm (for the 1200- and 600 G/mm grating, respectively).

The spectrometer was positioned at the 'magic angle' of 54.7° with respect to the the ion beam. At this angle, there is no influence of the possible anisotropy due to polarization effects in the radiation. To avoid effects due to different sensitivities to parallel and perpendicular polarized light, the spectrometer was tilted around the observation axis in such a way that the entrance slit is inclined under 45°.

The sensitivity of the spectrometer was determined by comparison of various charge

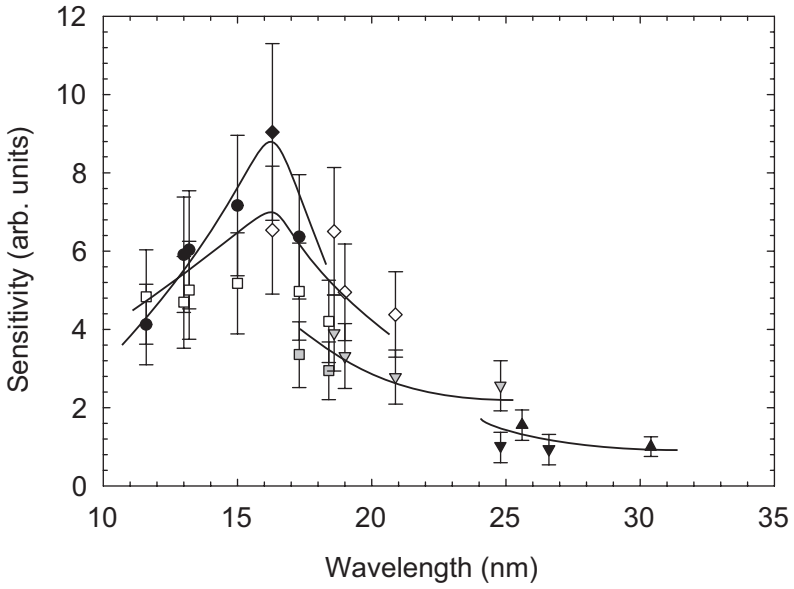

Figure 4.4: *Wavelength dependent response function of the EUV spectrometer, equipped with the 1200 G/mm grating. The jumps in the sensitivity are the result of different positions of the micro channel plate. N^{5+} + H_2 - ♦, ◊, grey and black ▼. O^{6+} + H_2 - ●, white and grey □. He^{2+} + H_2 - ▲. The resulting calibration is normalized to the sensitivity at 30.4 nm and estimated to be accurate within 15%. Lines are drawn to guide the eye.*

exchange reactions of which absolute cross sections are known. Emission cross sections were deduced from photon yields by using the following relation:

$$\sigma_{em} = A \cdot S(\lambda) \frac{q}{Q} N \tag{4.1}$$

where $S(\lambda)$ is the spectrometer's wavelength dependent response, q is the charge state of the incoming ion, Q is the accumulated charge over which is integrated, N is the photon yield. A includes all parameters that are kept constant during our experiments, amongst which the target density, and is found by calibrating via known cross sections.

For the helium experiments described in Chapter 5, only the instrument's sensitivity to the HeI and HeII emission was of importance. This sensitivity was obtained by calibration via He^{2+} + H_2 cross sections (Hoekstra et al., 1991). For the other experiments in this thesis, the 1200 G/mm grating was used, and the interpretation of these spectra required a more extensive calibration of the spectrometer. This calibration involved collisions between various ions and H_2, with well known emission cross sections (Dijkkamp et al., 1985). The resulting sensitivity is shown in Fig. 4.4. The different jumps in the sensitivity are the result of different positions of the micro channel plate. The resulting calibration is estimated to be accurate within 15%.

5 Collisions between He^{2+} and Various Cometary and Planetary Molecules

Helium is the most abundant solar wind ion besides H^+, and its charge exchange emission in the EUV can provide detailed insight into the interaction between solar system plasmas. Using the two complementary experimental techniques of photon emission spectroscopy and translation energy spectroscopy we have studied state selective charge exchange in collisions between fully ionized helium and target gases characteristic for cometary and planetary atmospheres (H_2O, CO_2, CO and CH_4). The experiments were performed at velocities typical for the solar wind (200 – 1500 km/s). We produced a data sets that can be used for modeling the interaction of solar wind alpha particles with cometary and planetary atmospheres.

5.1 Experiments

We have used two complementary experimental techniques, Photon Emission Spectroscopy (PES, see Chapter 4) and Translational Energy Spectroscopy (the TES set up at Queen's University Belfast - see e.g. Hodgkinson et al., 1995; Kearns et al., 2001) to obtain state selective cross sections for single-electron capture reactions. These are given by:

$$He^{2+} + B \longrightarrow He^{+}(n\ell) + B^{+} \tag{5.1}$$

with B the neutral target gas and $n\ell$ the principal and angular momentum quantum numbers. In PES experiments the photon emission subsequent to charge transfer into an excited state is measured while in TES experiments the energy gained or lost by the ion is determined. The energy change corresponds to the difference in electronic binding energy before and after the interaction.

In the PES experiment at the KVI Groningen, an ion beam is crossed with a neutral gas jet (see Chapter 4). The ions are produced in an ECR-Ion Source, which is floated on high

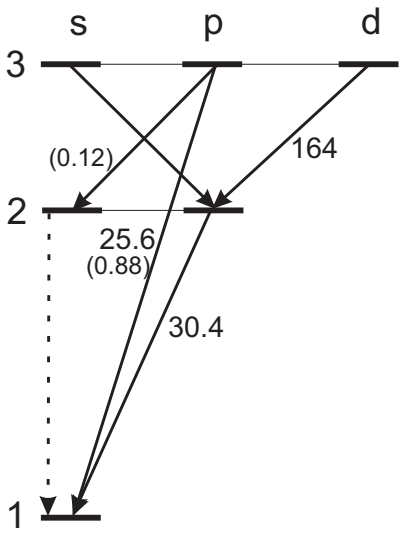

Figure 5.1: *Part of the HeII decay scheme, indicated are the wavelengths (in nm) of the relevant transitions. The numbers in brackets refer to the branching ratios. The forbidden HeII(2s – 1s) decay is represented by a dashed arrow.*

potential allowing collision energies between 1.5 and 12 keV/amu in the case of He^{2+} ions. An EUV spectrometer (5 – 80 nm) was used to obtain the emission spectra following charge exchange. Absolute wavelength and sensitivity calibration of the EUV system was achieved by cross-reference to previous measurements on systems with well known cross sections (see e.g. Hoekstra et al., 1991). The spectrometer is equipped with a position sensitive detector allowing for the simultaneous detection of a wavelength range of approximately 20 nm. The HeII Lyman series was observed in second order, therefore the HeII (2p → 1s), HeII (3p → 1s) appear at 60.4 and 51.2 nm, respectively, see Fig. 5.1. At the highest collision energies, very weak traces of emission from higher HeI (np) states are detected (around 48 nm). The choice of detecting the Lyman lines in second order allows for the simultaneous measurement of the neutral HeI($1s2p\ ^1P \rightarrow 1s^2\ ^1S$) transition at 58.4 nm, that results from two-electron capture. As in our previous studies of $He^{2+} - H_2$ interactions, the spectra are found to be dominated either by the HeII (2p → 1s) line or by the HeI ($1s2p\ ^1P \rightarrow 1s^2\ ^1S$) line depending on collision energy (Lubinski et al., 2001; Bodewits et al., 2004). The line emission is connected to the population of specific $n\ell$ states.

Translational Energy Spectroscopy (TES) experiments were performed at the Queen's University Belfast (Hodgkinson et al., 1995; Kearns et al., 2001). A beam of He^{2+} ions is produced by an ECR ion source and extracted and transported via a 'floating beam line system' in which the beam line is held at a potential of -4 kV. The momentum analyzed He^{2+} beam passes through two hemispherical energy analyzers to reduce its energy spread and is then decelerated to collision energies between 0.2 and 2.0 keV/amu. At these energies the ion beam crosses the neutral gas target. Analysis of kinetic energy changes of the

charge changed ions yields the identification and the determination of the relative contributions of all reaction channels. Because of the degeneracy of the different angular momentum states within a principal quantum shell (cf. Fig. 5.1), they cannot be resolved by the TES method. The TES measurements are therefore directly linked to the total population of the n-shells. In addition, attenuation measurements using the TES set-up at Belfast have been carried out to determine the total one electron capture cross sections for He^{2+} – CH_4 interactions (Seredyuk et al., 2005b).

Together the present TES and PES experiments cover an energy range of 0.2 to 10 keV/amu, which corresponds to velocities from 190 – 1400 km/s, thereby encompassing typical velocities of both slow (200 – 400 km/s) and fast (~1000 km/s) solar winds (Neugebauer et al., 1998).

5.2 Analysis

The relative cross sections from the TES and PES experiments are put on an absolute scale by normalization to total single-electron capture cross sections, σ_{sec}. For the TES experiments absolute values for the n-shell specific cross sections are obtained from the relative cross sections, σ_n^{rel} as follows:

$$\sigma_n = \frac{\sigma_n^{rel}}{\sum_n \sigma_n^{rel}} \sigma_{sec} \tag{5.2}$$

This procedure is repeated for each measurement. The uncertainties are determined by statistical errors and errors associated with the normalization cross sections. The relation between the HeII (np → 1s) Lyman line emission $\sigma_{em}(n\mathrm{p}-1\mathrm{s})$ and the total cross section is somewhat less straightforward:

$$\sum_n \sigma_{em}(n\mathrm{p}-1\mathrm{s}) = \sigma_{sec} - \sigma(n=1) - \sigma^*(2\mathrm{s}) \tag{5.3}$$

where $\sigma^*(2s)$ represents the 2s population cross section, which aside of being populated by direct capture can accumulate population via np→2s transitions, see Fig. 5.1. The only unknown is the direct electron capture contribution $\sigma(2\mathrm{s})$ to $\sigma^*(2\mathrm{s})$, because $\sigma(n=1)$ is

Table 5.1: *Resonant binding energies for He^{2+} one-electron capture. Energies are estimated on basis of the Over-the-Barrier model. The binding energies of the n=1, 2, and 3 shells in He^+ are 54.4, 13.6, and 6.0 eV, respectively*

Target	I_b (eV)	I_f
CO	13.7	17.3
CH_4	12.5	15.8
CO_2	13.8	17.4
H_2O	12.6	15.9
H, O	13.6	17.1

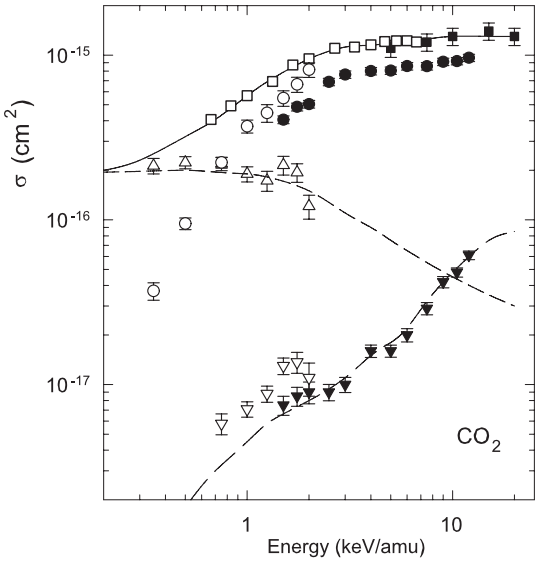

Figure 5.2: *Single-electron capture related cross sections for He^{2+} – CO_2 collisions. Present data: ● – σ_{em}(2p–1s), ▼ – σ_{em}(3p–1s), ○ – σ(n=2), ▽ – σ(n=3), and △ – σ(n=1). Total single electron capture cross sections: ■ – Rudd et al. (1985a), □ – Greenwood et al. (2000). Curves – cross sections used for calibration and modeling purposes, see text.*

known from the TES experiments and the np→2s contributions to σ^*(2s) can be calculated from the corresponding np→ 1s transitions via their respective branching ratios. For example $\sigma_{em}(3p-2s)$ is equal to $(0.12/0.88)\sigma_{em}(3p-1s)$, see Fig. 5.1. For absolute calibration the data at 10 keV/amu was used under the assumption that the ratio between σ(2s) and σ(2p) is statistical, i.e., 1:3. At such an energy a (near) statistical distribution over the angular momenta is a common feature of one-electron capture by multiply charged ions (Janev and Winter, 1985; Hoekstra et al., 1990; Fritsch and Lin, 1991). The absolute calibration of the PES experiment at 10 keV/amu is applied to all energies. The uncertainties of the PES data are determined by statistical errors and possible target density fluctuations ($\leq$ 5%). There is a systematic uncertainty of about 20 – 25% due to the calibration procedure.

Together with existing total single-electron capture cross sections, the TES and PES data for He^{2+} ions colliding on CO_2, CH_4, CO, and H_2O are compiled in Figures 5.2, 5.3, 5.4, and 5.5. The following general trends are observed: **i)** the total one-electron capture cross sections are of similar order of magnitude and they decrease with decreasing collision energy; **ii)** capture into high-n shells ($n \geq 3$) is a minor contribution to the total cross section; **iii)** capture into the $n = 2$ shell ($\sigma_{em}(2p-1s)$ and σ_2) is the dominant channel at higher energies, but decreases rapidly for energies below ~3 keV/amu; **iv)** at energies below ~1 keV/amu, capture into the ground state $\sigma(n = 1)$ dominates. The same trends have been observed for collisions on H_2 (see e.g. Hoekstra et al. (1994), Hodgkinson et al. (1995)

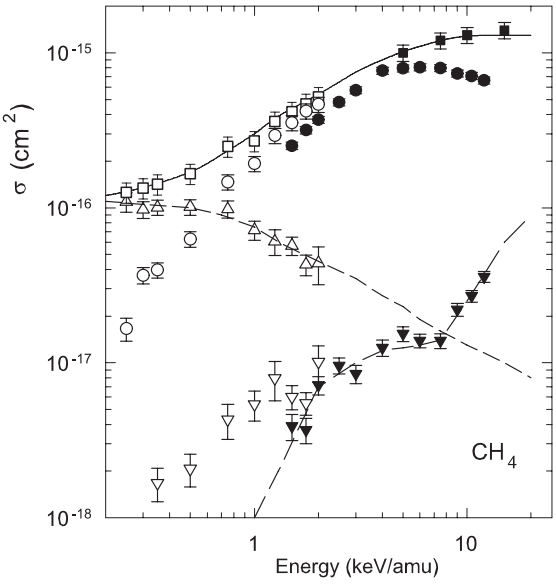

Figure 5.3: *Single-electron capture related cross sections for He^{2+} – CH_4 collisions. Present data: ● – σ_{em}(2p–1s), ▼ – σ_{em}(3p–1s), ○ – σ(n=2), ▽ – σ(n=3), and △ – σ(n=1). Total single electron capture cross sections: ■ – Rudd et al. (1985a), □ – this work. Curves - cross sections used for calibration and modeling purposes, see text.*

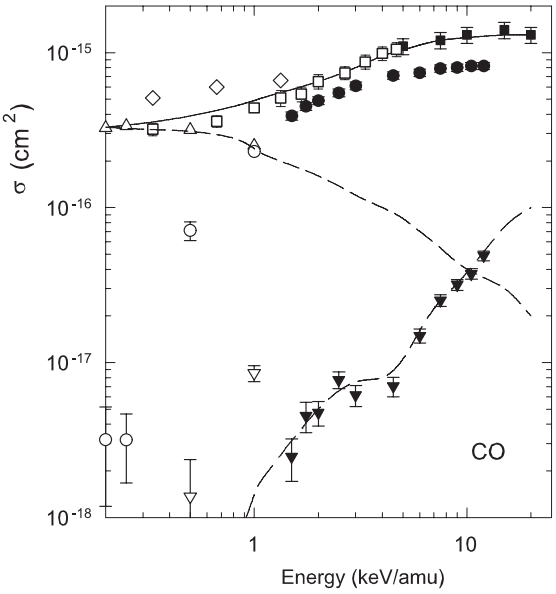

Figure 5.4: *Single-electron capture related cross sections for He^{2+} – CO collisions. Present data: ● – σ_{em}(2p–1s), ▼ – σ_{em}(3p–1s). Kearns et al. 2001: ○ – σ(n=2), ▽ – σ(n=3), and △ – σ(n=1). Total single electron capture cross sections: ■ – Rudd et al. (1985a), □ – Cadez et al. (2002), ◊ – Ishii et al. (2002). Curves – cross sections used for calibration and modeling purposes, see text.*

and references therein).

The aforementioned points also hold for atomic hydrogen, except that no population of the HeII (1s) ground state is observed (see e.g. Shah and Gilbody, 1974, 1978; Hoekstra et al., 1991), not even at low energies. For atomic hydrogen the total single-electron capture follows a similar steep decrease at low energies as observed in the present cases for capture into HeII (n=2). This is a direct manifestation of the fact that resonant charge transfer is not feasible (Janev and Winter, 1985; Fritsch and Lin, 1991). Using a simple 'resonant' charge transfer model as the Over-the-Barrier model (Niehaus, 1986) one finds the following relation between the final state energies and the ionization potential, I_{pot}, of the electron donor:

$$E_{final} = (1 + \frac{q-1}{2\sqrt{q}+1}) I_{pot} \tag{5.4}$$

with q the charge state of the ion. For the collision systems under consideration the final binding energies for resonant electron capture are given in Table 5.1. From the energies it is obvious that the HeII (n=2) shell is most likely populated, but there is an energy mismatch of 2 – 4 eV depending on target species. Due to this energy difference the cross sections decrease at lower collision energies.

This argumentation is in apparent contradiction with the increase of the cross sections for capture into the He^+(n=1) ground state at low energies, because the energy mismatch is very large, almost 40 eV. However, for molecular targets the considerable amount of electronic excess energy associated with charge transfer into the ground state can be absorbed and released via dissociative processes (Hoekstra et al., 1991; Hodgkinson et al., 1995; Kearns et al., 2001; Seredyuk et al., 2005a). As these so-called dissociative electron capture processes involve a kind of energy equilibration between ion and target, they are most efficient at lower collision energy for the interaction time is longer.

Finally, it is of note that in the energy range of 1 – 2 keV/amu in which TES and PES data overlap, the ratio of $\sigma(n=2)$ and $\sigma_{em}(2p-1s)$ is consistent with a statistical ℓ-state distribution.

5.3 EUV Line Emission Data for Alpha Particles

The interaction of solar wind alpha particles with cometary gases shows up in the EUV spectral range via line emission at 30.4 nm (HeII ($2p \rightarrow 1s$)) and 58.4 nm (HeI ($1s2p\ ^1P \rightarrow 1s^2\ ^1S$)) (Krasnopolsky et al., 1997; Krasnopolsky and Mumma, 2001; Bodewits et al., 2004). For predicting line intensities at 30.4 nm in astrophysical environments one can not directly use the measured $\sigma_{em}(2p-1s)$ cross sections because of additional contributions from the $He^+(2s)$ state. The lifetime of the metastable $He^+(2s)$ is so long that, in contrast to cometary environments, its decay (via state mixing with the $He^+(2p)$ level) is not observed in field-free laboratory experiments (Shah and Gilbody, 1978; Hoekstra et al., 1991). However, the overall cross section for 30.4 nm emission, i.e., the cross section for 'infinitely' long observation times, can be constructed from the laboratory data as follows:

$$\sigma_{em}(30.4\text{nm}) = \sigma_{sec} - \sigma(n=1) - \sigma_{em}(3p-1s) \tag{5.5}$$

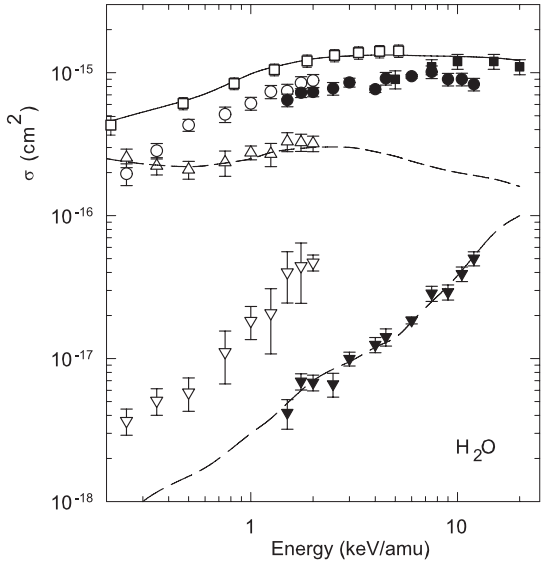

Figure 5.5: *Single-electron capture related cross sections for He^{2+} – H_2O collisions. Present data: ● – σ_{em}(2p–1s), ▼ – σ_{em}(3p–1s), ○ – σ(n=2), ▽ – σ(n=3), and △ – σ(n=1). Total single electron capture cross sections: ■ – Rudd et al. (1985b), □ – Greenwood et al. (2004). Curves – cross sections used for calibration and modeling purposes, see text.*

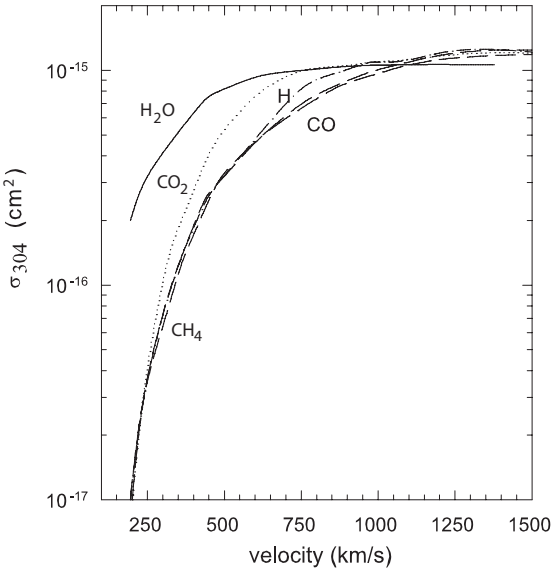

Figure 5.6: *Cross sections for HeII line emission at 30.4 nm for 'infinite' observation times, see text.*

The cross sections for 30.4 nm emission determined in this way are compiled in Fig. 5.6. For reference the data for atomic hydrogen are added (Shah and Gilbody, 1978; Hoekstra et al., 1991). Except for water molecules, the velocity behavior of the HeII line emission at 30.4 nm is found to be remarkably similar for all targets. The values used for σ_{sec}, $\sigma(n=1)$, and $\sigma_{em}(3p-1s)$ are indicated by the smooth curves in Figures 5.2, 5.3, 5.4, and 5.5.

The competing line emission at 58.4 nm, resulting from simultaneous two-electron capture into HeI ($1s2p\ ^1P$), is almost independent of the He^{2+} collision velocity (see Fig. 5.7). As the 30.4 nm line emission depends strongly on velocity the ratio between the two lines may be used as velocity diagnostics (Bodewits et al., 2004).

In the interaction between comets and the solar wind, collision between He^{2+} and water play a key role. Helium charge exchange can be traced by line emission in the extreme-ultraviolet and the ratio between the Ly-α and Kα emission lines of HeII and HeI at 30.4 nm and 58.4, respectively provides a direct measure for projectile velocities that are typical for the solar wind. For solar wind velocities, the line ratio for the system $He^{2+} - H_2O$ collisions is higher than the line ratios found for CO and H_2. This implies that for those cases where water is the dominant collision partner for solar wind He-ions, diagnostics based on CO and H_2 helium line emission ratios probably overestimate the solar wind velocity (Bodewits et al., 2004).

5.4 Additional Charge Exchange Data

To model the line emission, one needs to track the evolution of the charge state distribution of helium ions entering in the gas cloud of the comet (Chapter 8). Besides the single electron capture (SEC) process by He^{2+}

$$He^{2+} + B \longrightarrow He^{+} + B^{+} \tag{5.6}$$

one also has to consider bound double-electron capture (B2C) by He^{2+}:

$$He^{2+} + B \longrightarrow He + B^{2+} \tag{5.7}$$

and sequential one-electron capture (SEQ) by He^{+}:

$$He^{+} + B \longrightarrow He + B^{+} \tag{5.8}$$

These three processes control both the charge state distribution and the line emission. For total bound double capture (Eq. 5.7) we used data of Rudd et al. (1985a); Greenwood et al. (2000) and for one-electron capture by He^{+} (Eq. 5.8) we used data of Rudd et al. (1985c,b); Greenwood et al. (2000, 2004). For the 58.4 nm line emission following single-electron capture by He^{+} we used data of Juhász (2004). Because of the absence of the relevant data for interactions on atomic oxygen, the following cross section estimates were used: for direct and sequential single-electron capture (Eqs. 5.6 and 5.8) we used the data for atomic hydrogen because O and H have the same ionization potential; for double-electron capture we used the CO data because it has a similar second ionization potential.

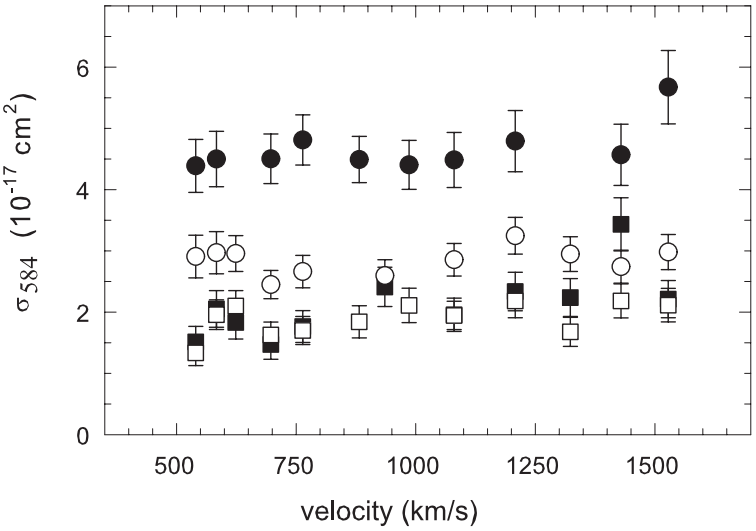

Figure 5.7: *Cross sections for HeI line emission at 58.4 nm.* ● *- CO_2,* ○ *- CO,* ■ *- H_2O, and* □ *- CH_4.*

5.5 Helium Line Ratio

The experimental setup used for the PES measurements described in this chapter was not yet equipped with decelerating ion optics. Direct measurements of cross sections were therefore only possible between 1.5 – 12 keV/amu (or 535 – 1500 km/s), slightly above slow solar wind velocities (≤400 km/s). For these velocities, the ratio between the 30.4 nm and 58.4 nm emission lines is more or less constant as is shown in Fig. 5.8. Because the cross section for capture into the HeI(1s2p) state has been seen to be roughly constant with velocity in collisions between both CO and H_2 (Bodewits et al., 2004), we estimated 58.4 nm double electron capture cross sections for velocities below 1.5 keV/amu by extrapolation from our results. By assuming a statistical distribution over the angular momenta, the 30.4 nm/58.4 nm line ratio can then be estimated from total HeII (2ℓ) cross sections in He^{2+} – water molecule collisions (Seredyuk et al., 2005a; Abu-Haija et al., 2003).

In Fig. 5.8, the He^{2+} – water molecule line ratio is compared with the line ratios obtained with H_2 and CO targets. Although the line ratios for collisions with the latter two molecules overall show the same behavior, the line ratio of water shows a rather different behavior over the whole range of typical solar wind velocities. The helium line ratio changes orders of magnitude for only a relatively small increase of velocity. This suggests that the 30.4/58.4 nm ratio could be used as velocity diagnostics for charge exchange interactions, but also that one should distinguish the contribution of different target species. This will be further discussed in the Chapters 8 and 9.

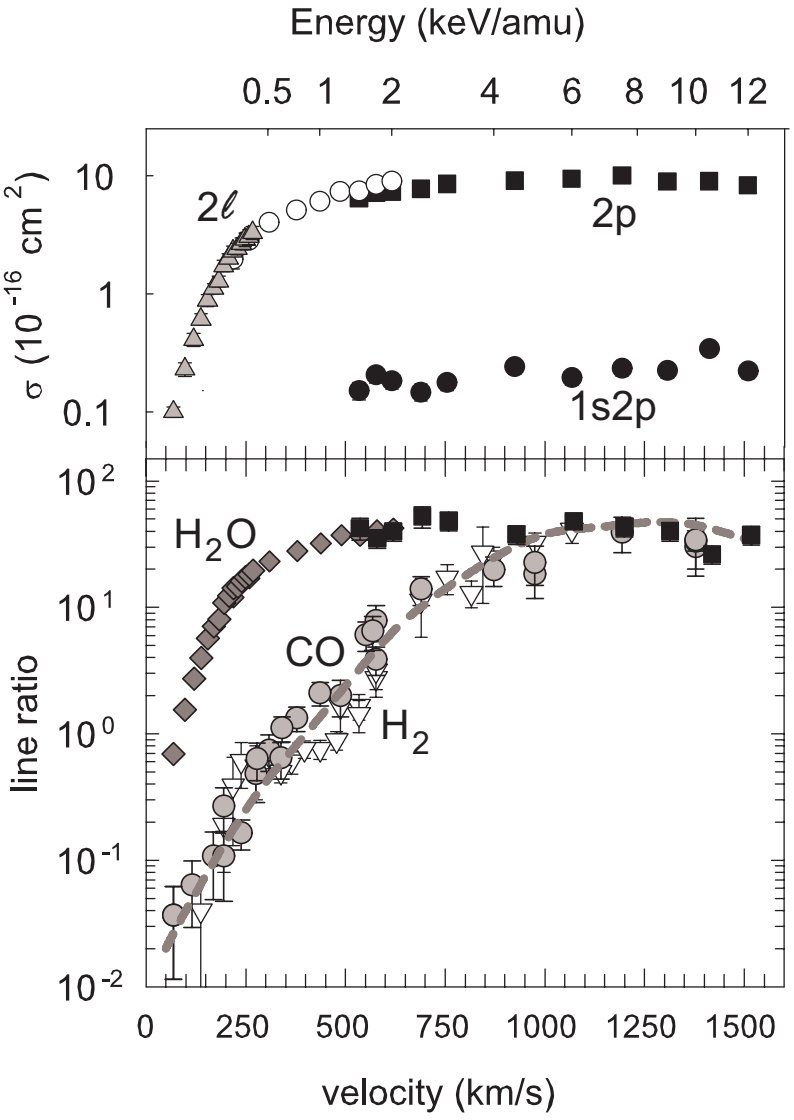

Figure 5.8: *Dependency of line emission on the projectile velocity.* ***Upper panel:*** *He^{2+} colliding on H_2O. Present data for state selective cross sections for HeII (2p) are indicated by black squares, state selective cross sections for HeII (2ℓ) by open circles (Seredyuk et al., 2005a) and grey triangles (Abu-Haija et al., 2003). Present data for HeI (1s2p) are indicated by black circles.* ***Lower panel:*** *Experimental line ratios between 30.4 nm and 58.4 nm emission for He^{2+} colliding on H_2 (white triangles), CO (grey circles – Bodewits et al., 2004) and H_2O (measured – black squares, estimated – grey diamonds). At low velocities, the HeI cross section is estimated by extrapolation, see text. Lines are drawn to guide the eye.*

6 Electron Capture Channels in Collisions between O^{6+} and H_2O

Apart from protons and alpha particles, the solar wind contains a small percentage of multiply charged C, O, N and Ne ions. In addition, very small fractions of intermediately charged Mg, Si, S and Fe ions are present in the solar wind (Schwadron and Cravens, 2000). The solar winds can be divided in slow and fast winds at approximately 200 – 400 km s^{-1} and approximately 500 – 1000 km s^{-1}, respectively. The full velocity range encompassed by the slow and fast winds corresponds to a collision energy range of approximately 0.2 – 6 keV/amu.

The most abundant solar wind minor ion is O^{6+}, which has not been considered in great detail because its emission falls just below the low-energy detection limits of *Chandra* and XMM-*Newton*. OVI emission has been detected in FUSE observations of comet C/WM1 (Weaver et al., 2002) and EUVE observations of comet Hyakutake (Krasnopolsky and Mumma, 2001). Oxygen ions precipitating into the Jovian atmosphere are important contributors to the observed EUV and X-ray emission of the aurorae of Jupiter (Waite et al., 1994). Model calculations based on O^{q+} – H_2 interactions underline the important role of O^{6+} ions as line emitters (Kharchenko et al., 1998; Liu and Schultz, 1999).

In particular, state selective electron capture by O^{6+} in collisions on H, H_2 and He has been studied extensively, e.g. refs. (Dijkkamp et al., 1985; Fritsch and Lin, 1986; Shimakura et al., 1987; Beijers et al., 1992; Liu and Schultz, 1999; Lubinski et al., 2000; Kearns et al., 2003). For many typical cometary and planetary target species such as CO, CO_2 and H_2O the availability of experimental or theoretical data is very limited (Bodewits et al., 2004).

In this chapter we will focus on the one-electron capture in 0.1 – 7.5 keV/amu collisions of O^{6+} on H_2O molecules. Water molecules are the most likely electron donors in the interaction of the solar wind with comets.

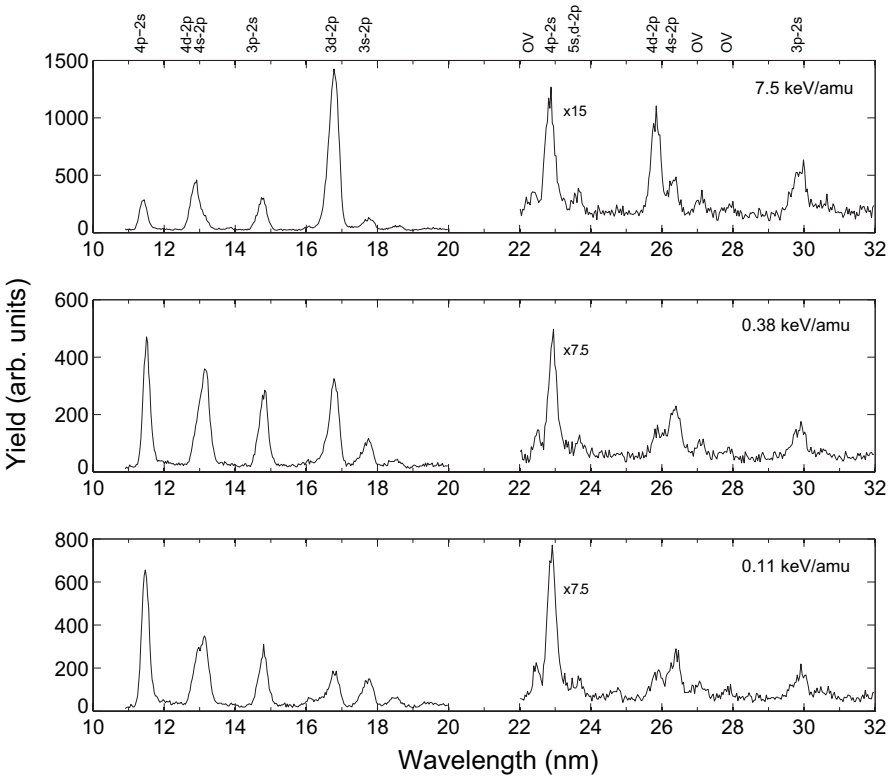

Figure 6.1: *Velocity dependence of charge exchange spectra for collisions between O^{6+} and H_2O. Shown are the first order (10 – 20 nm) and the second order (22 – 32 nm) spectra for collision energies of 7.5 keV/amu (top), 0.38 keV/amu (middle) and 0.11 keV/amu (bottom). The spectra are corrected for the accumulated charge and target pressure, but not for the spectrometer's wavelength dependent response. Second order spectra are blown up for the ease of presentation.*

6.1 Experiment

All experimental data in this chapter were obtained with the Photon Emission Spectroscopy (PES) experiment described in Chapter 4. Fig. 6.1 shows typical spectra obtained with the PES set up, at different collision velocities. With the 1200 grooves/mm grating used for this experiment, the resolution of the spectrometer is approximately 0.3 nm FWHM. Spectra were measured at two different positions along the Rowland circle, in order to obtain first and second order spectra. In second order, the spectrometer is less sensitive, but the $1s^2 4d$–$1s^2 2p$ and $1s^2 4s$–$1s^2 2p$ peaks that overlay in first order are clearly separated.

6.2 Spectral Analysis

All spectra were analyzed by fitting Gaussian peaks to the data. Emission cross sections were deduced from photon yields by using the following relation:

$$\sigma_{\mathrm{em}} = A \cdot S(\lambda) \frac{q}{Q} N \tag{6.1}$$

where $S(\lambda)$ is the spectrometer's wavelength dependent response, q is the charge state of the incoming ion, Q is the accumulated charge over which is integrated, N is the photon yield. A includes all parameters that are kept constant during our experiments, amongst which the target density, and is found by calibration via known cross sections for He^{2+}+H_2O (Seredyuk et al., 2005a; Bodewits et al., 2005, 2006). The resulting emission cross sections are given in Table 6.1.

To derive population cross sections, the measured emission cross sections should be corrected for branching ratios and cascade effects. The decay scheme of OVI is given in Fig. 6.2. Transitions from $n = 4 \rightarrow 3$ fall outside the wavelength range accessible to the spectrometer when equipped with the 1200 G/mm grating used here. Transitions from n= 5 → 2 fall within the observable wavelength regime, but lie too close to the strong 4p–2s transition to be resolved in first order. In second order however, the separation between the lines becomes large enough for individual detection and careful inspection of these spectra shows a very weak emission feature due to the 5s,5d – 2p transitions at ~23.4 nm (see Fig. 6.1). We will therefore assume that capture into $n = 5$ is negligible. The population cross sections can therefore be derived from the measured line emission cross sections by means of the following relations:

Table 6.1: *Fit results - measured emission cross sections for one electron capture in O^{6+}+H_2O collisions, for different collision energies. All cross sections are in units of 10^{-16} cm^2. Only relative errors are given. The systematic uncertainty is approximately 25%.*

E (keV/amu)	11.6 nm	13.0 nm	13.2 nm	15.0 nm	17.3 nm	18.4 nm
0.11	11 ± 1.1	3.2 ± 0.3	5.4 ± 0.5	4.2 ± 0.4	5 ± 0.5	2.6 ± 0.3
0.19	8.7 ± 0.9	3.2 ± 0.3	5.3 ± 0.5	4.4 ± 0.4	8 ± 0.8	2.1 ± 0.2
0.38	7.3 ± 0.7	2.8 ± 0.3	5.3 ± 0.5	4.2 ± 0.4	10 ± 1.0	1.7 ± 0.2
1.31	5.0 ± 0.5	3.0 ± 0.3	4.1 ± 0.4	3.1 ± 0.3	12 ± 1.2	1.2 ± 0.1
3.94	4.3 ± 0.4	4.5 ± 0.5	2.9 ± 0.3	3.6 ± 0.4	22 ± 2.2	1.3 ± 0.1
7.50.....	3.3 ± 0.3	4.7 ± 0.5	1.4 ± 0.1	3.2 ± 0.3	33 ± 3.3	1.3 ± 0.1

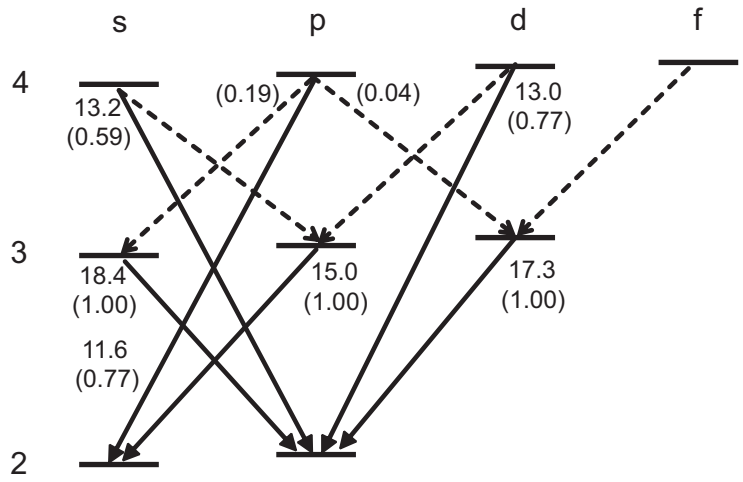

Figure 6.2: *Grotrian diagram of OVI ($1s^2 n\ell$) transitions. Observed transitions are indicated with solid lines, other transitions by dashed lines. Wavelengths are given in nanometers, the numbers between brackets are the branching ratios.*

$$
\begin{aligned}
\sigma(4s) &= \sigma_{em}(13.2)/0.59 \\
\sigma(4p) &= \sigma_{em}(11.6)/0.77 \\
\sigma(4d) &= \sigma_{em}(13.0)/0.77
\end{aligned}
$$

$$
\begin{aligned}
\sigma(3s) &= \sigma_{em}(18.4) - 0.19\sigma(4p) \\
&= \sigma_{em}(18.4) - 0.25\sigma_{em}(11.6) \\
\sigma(3p) &= \sigma_{em}(15.0) - 0.41\sigma(4s) - 0.23\sigma(4d) \\
&= \sigma_{em}(15.0) - 0.69\sigma_{em}(13.2) - 0.30\sigma_{em}(13.0)
\end{aligned}
\tag{6.2}
$$

$$
\begin{aligned}
\sigma(3d+4f) &= \sigma(17.3) - 0.04\sigma(4p) \\
&= \sigma(17.3) - 0.03\sigma_{em}(11.6)
\end{aligned}
$$

From these relations, it is clear that except for the 4f state, capture into the $n = 4$ states is observed directly, and that population cross sections for $n = 3$ are derived indirectly from the line emission cross sections. It is not possible to separate capture into the $1s^2 3d$ and $1s^2 4f$ states without observing the direct transition between those two states at longer wavelengths.

Assuming that one electron capture populates only $n = 3,4$ states, the total one electron capture cross sections can be found by adding up these state selective cross sections:

$$\sigma_t = \sum_{n\ell} \sigma(n\ell) \tag{6.3}$$

The results are subject to a number of uncertainties. The dominating absolute uncertainty is that arising from the spectrometer's calibration by means of cross sections for CXE from He^{2+} ions, and is approximately 20% (Bodewits et al., 2006). This error affects all data points, and leads to a simple scaling factor. A more complex error is due to the uncertainty in the wavelength dependent sensitivity of the spectrometer, which we estimate to be 10 – 15%. Added in quadrature these uncertainties lead to an absolute systematic uncertainty of 25%. The uncertainty associated with the wavelength-dependent sensitivity may also influence the relative line strengths which are of importance when assessing cascade contributions. Target fluctuations were controlled by performing regular calibration measurements, but lead to a random error in the order of 5%. Statistical errors for these experiments were small due to high photon yields and never exceeded 1% (1σ). Therefore we assume a relative uncertainty of 10% in the line emission cross sections.

6.3 Results and Discussion

6.3.1 Population Cross Sections

The state selective cross sections, determined from the line emission data via equation 6.2, are shown in Fig. 6.3. Cross sections for electron capture into the $1s^2 3s$ and $1s^2 3p$ states are very small ($\leq 10^{-16}$ cm^2). Therefore, although we did not measure separate $1s^2 4f$ and $1s^2 3d$ cross sections, it seems very reasonable to assume that capture into $1s^2 3d$ is not significant and thus, that $n = 4$ is the dominant reaction channel in collisions between O^{6+} and H_2O molecules, as expected from the Classical-over-the-Barrier model (Fig. 6.5), and in line with the TES experiments by Seredyuk et al. (2005c).

At low energies, the $1s^2 4p$–$1s^2 2s$ transition at 11.6 nm is the strongest line in the spectrum, followed by the relatively strong $1s^2 4s$–$1s^2 2p$ emission. Around 0.5 keV/amu, all emission lines in the spectrum are roughly equally strong, as are the capture cross sections. At high velocity, the spectrum is completely dominated by the $1s^2 3d$–$1s^2 2p$ transition at 17.3 nm as the ℓ-state distribution has shifted to higher states.

The population of low ℓ-states at low energy, and a near statistical distribution at higher energy is a general feature in electron capture by multiply charged ions (see e.g. Janev and Winter, 1985; Lubinski et al., 2001). To illustrate the change in the ℓ-distribution more

Table 6.2: *State selective cross sections for one electron capture in O^{6+}+H_2O collisions, for different collision energies. All cross sections are in units of 10^{-16} cm^2. Only relative errors are given. The systematic uncertainty is approximately 25%.*

E (keV/amu)	3s	3p	4s	4p	4d	4f + 3d	Total
0.11	0.8 ± 0.3	-0.5 ± 0.6	9.1 ± 0.9	14 ± 1.4	4.1 ± 0.4	4.8 ± 0.6	33 ± 1.9
0.19	0.4 ± 0.3	-0.2 ± 0.6	9.0 ± 0.9	11 ± 1.1	4.1 ± 0.4	7.6 ± 0.8	32 ± 1.8
0.38	0.0 ± 0.2	-0.3 ± 0.6	8.9 ± 0.9	9.5 ± 1.0	3.6 ± 0.4	9.4 ± 1.0	31 ± 1.8
1.31	-0.2 ± 0.2	-0.6 ± 0.4	7.0 ± 0.7	6.5 ± 0.7	3.9 ± 0.4	11 ± 1.2	28 ± 1.6
3.94	0.3 ± 0.2	0.2 ± 0.4	5.0 ± 0.5	5.5 ± 0.6	5.8 ± 0.6	22 ± 2.2	39 ± 2.4
7.50	0.9 ± 0.1	0.9 ± 0.4	2.3 ± 0.2	4.3 ± 0.4	6.1 ± 0.6	33 ± 3.3	47 ± 3.4

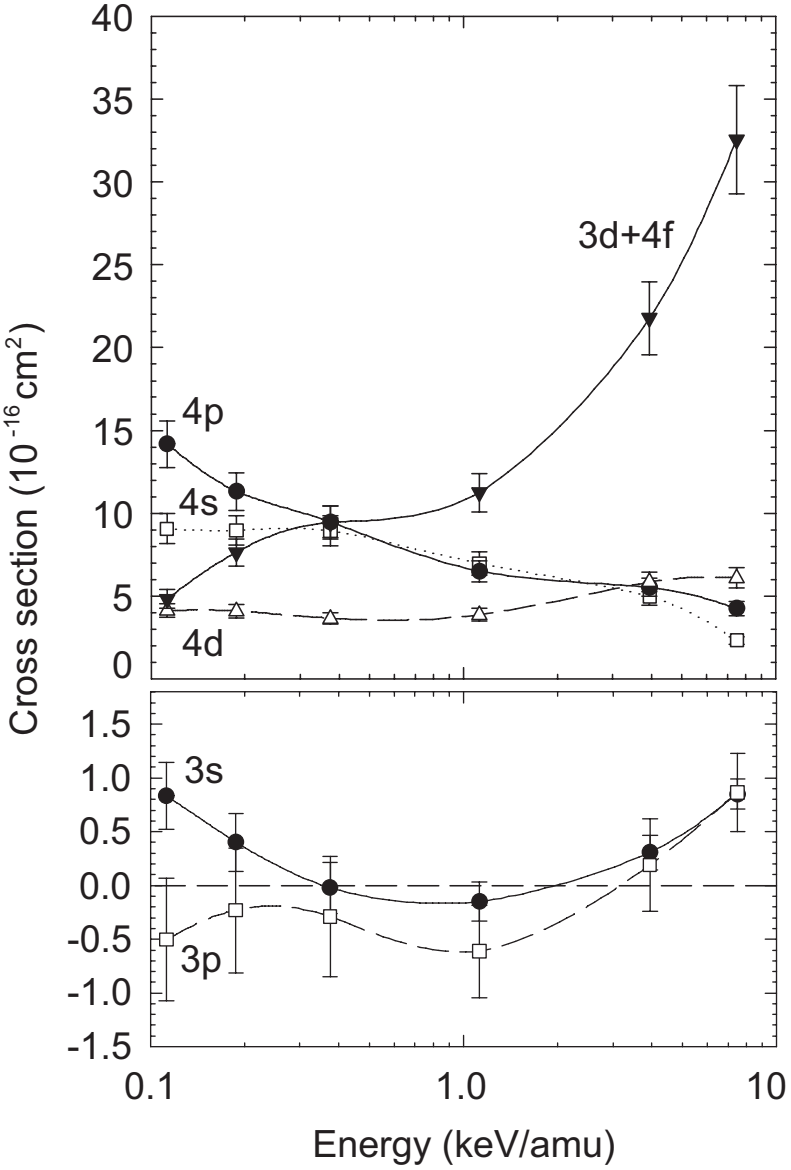

Figure 6.3: *Velocity dependence of state selective, single electron capture cross sections for O^{6+} + H_2O.* ***Upper panel:*** *Capture into $n = 4$. □ − $\sigma(4s)$; • − $\sigma(4p)$; △ − σ(4d); ▼ − $\sigma(3d+4f)$* ***Lower panel:*** *Capture into $n = 3$. • − $\sigma(3s)$; □ − $\sigma(3p)$. Lines are drawn to guide the eye. Only relative errors are given. The systematic uncertainty is approximately 25%.*

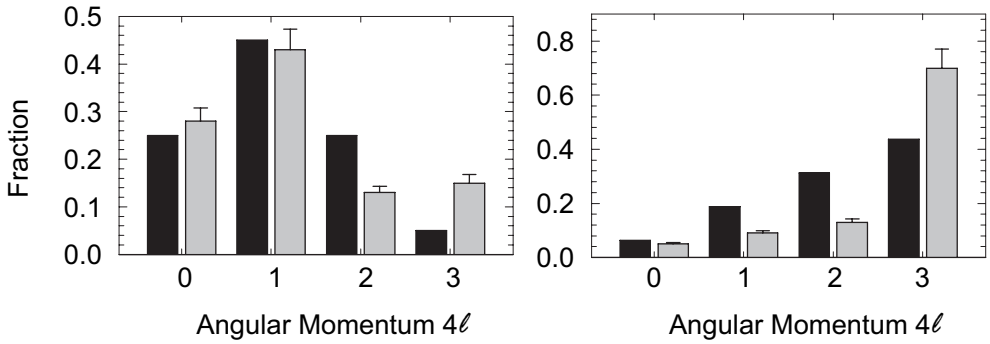

Figure 6.4: *Comparison of measured (grey) and theoretical distribution (black) over the 4ℓ-states.* ***Left panel:*** *Measured distribution at 0.11 keV/amu, compared with a radial coupling determined low energy distribution (Abramov et al., 1978; Janev et al., 1983).* ***Right panel:*** *Measured distribution at 7.5 keV/amu, compared with a statistical ℓ-distribution typical for higher collision velocities.*

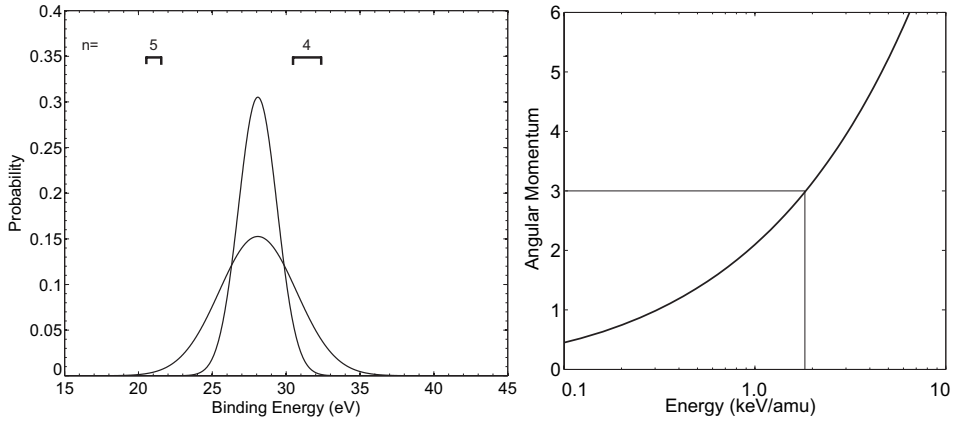

Figure 6.5: *Over-the-Barrier predictions for one electron capture in O^{6+} + H_2O collisions.* ***Left panel:*** *Reaction windows for collision energies of 0.25 and 4 keV/amu. OVI states are indicated.* ***Right panel:*** *Collision energy dependence of the maximum none-integer angular momentum (see text).*

qualitatively, two measured fractional population of the 4ℓ-states are shown in Fig. 6.4. At the lowest velocity, there is a fair agreement with the distribution function predicted for electron transfer via purely radial coupling (Abramov et al., 1978; Janev et al., 1983). At the highest velocity, where rotational couplings are important, the ℓ-state distribution roughly resembles a statistical distribution ($2\ell+1$), but the 4f state seems to be overpopulated with respect to the other 4ℓ states.

To some extent, as rotational coupling is linked to the collisional angular momentum, the shift in the ℓ-state distribution over angular momenta may be understood in terms of the classical Over-the-Barrier model (Burgdörfer et al., 1986). In the frame of the O^{6+} ion,

Table 6.3: *Ionization potentials and resulting Over-the-Barrier predictions for capture distances and geometrical cross sections.*

#	IP_n (eV)	$R_{c,n}$ (a.u.)	σ_n (Å^2)
1	12.6	12.7	39
2	27	8.6	11
3	~45	6.9	21

the target has an apparent angular momentum L of the order $L = bv_p$, with b the impact parameter and v_p the projectile velocity. The maximum impact parameter is the capture radius R_c at which the electron can cross the potential barrier between the target and projectile (Chapter 3). The maximum (non-integer) angular momentum ℓ of the captured electron can then be estimated using the relation:

$$L^2 = \ell(\ell+1) \tag{6.4}$$

In figure 6.5, the maximum angular momentum for O^{6+} + H_2O collisions is given as a function of collision energy. Capture into $\ell = 3$ becomes possible at collision energies above 2 keV/amu, above which we indeed observe a steep increase in the 4f capture cross section (Fig. 6.3).

As the 4f population is determined from the $1s^2$3d–$1s^2$2p transition, the apparent overpopulation of the 4f state at both low and high collision energies might be partly due to capture into the 3d and 5g states. As mentioned before, the measured 3s and 3p capture cross sections are close to zero and therefore it seems logic that capture is also negligible. However, in their TES experiments (0.75 – 1.5 keV/amu) Seredyuk et al. (2005c) find that next to dominant capture into $n = 4$, formation of $O^{5+}(n = 3)$ through dissociative capture channels is significant (up to 50%). Capture via these channels might therefore explain the apparent slight overpopulation of the 4f state at low energies. However, the contribution of these dissociative channels becomes smaller with decreasing velocity (Seredyuk et al., 2005c). At higher velocities, the reaction window widens enough to allow capture into $n = 5$ (Fig. 6.5). Also, the higher velocities result in higher maximum values of the electron's angular momentum. The apparent overpopulation of 4f can therefore be attributed to cascade contributions of the 5g state.

6.3.2 Total Cross Sections

We also used our data to determine velocity dependent, total one electron capture cross sections. The results are shown in Fig. 6.6. Above 1 keV/amu, where capture into $1s^2$4f becomes more and more important, the total cross section increases strongly with velocity. In the figure, total one electron capture cross sections for collisions with H and H_2 are also given for comparison. According to the classical-over-the-barrier (COB) model, one electron capture cross sections scale with the inverse of the ionization potential of the target (Chapter 3). The binding energy of water is 12.6 eV, that of H is 13.6 eV and that of

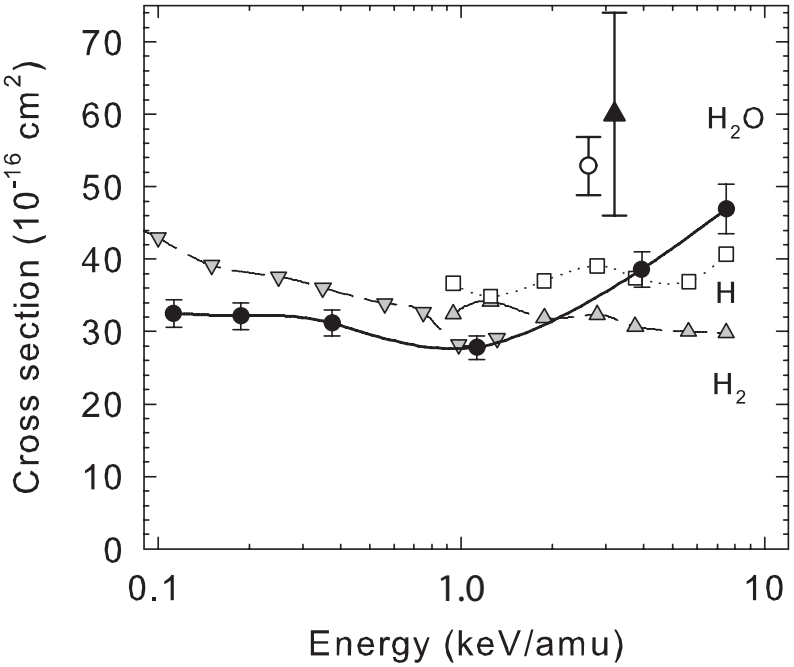

Figure 6.6: *Velocity dependence of total one electron capture cross sections for collisions between O^{6+} and H_2O – •, compared with charge exchange cross sections for H_2 (△ – Dijkkamp et al. (1985), ▽ – Lubinski et al. (2000)) and H (□ – Dijkkamp et al. (1985)). ○– total charge changing cross section from Mawhorter et al. (2007). ▲ – total charge changing cross section for C^{6+} + H_2O (Greenwood et al., 2001). Lines are drawn to guide the eye. Only relative errors are given. The systematic uncertainty is approximately 25%.*

H_2 is 16.1 eV. The COB model thus predicts that the one electron capture cross sections for all species will be comparable, which is confirmed by our results.

Total charge changing cross sections for O^{6+}+H_2O have recently been measured by Mawhorter et al. (2007). At a collision energy of 2.6 keV/amu, they measured a charge changing ($O^{6+} \rightarrow O^{5+}$) cross section of $(53 \pm 4) \times 10^{-16}$ cm^2. A similar cross section has been measured for C^{6+}+H_2O collisions (Greenwood et al., 2001). These cross sections are much larger than the one electron capture cross sections determined by us at comparable energies, which by interpolation would be approximately $(34 \pm 8) \times 10^{-16}$ cm^2. The difference can only be explained by auto-ionizing double electron capture processes.

The Over-the-Barrier model (Niehaus, 1986) can be used to make an estimation of the multiple electron capture cross sections. Using binding energies from literature (Alvarado et al., 2005) and assuming the binding energy of the third electron to be approximately 45 eV, we find cross sections of $\sigma_1 = 39$, $\sigma_2 = 11$ and $\sigma_3 = 21 \times 10^{-16}$ cm^2 (see Table 6.3). The σ_1 agrees well with the single electron capture cross section we measured, while the sum of σ_1 and σ_2 is close to the aforementioned charge changing cross sections ($q = 6 \rightarrow q = 5$).

Following the argumentation of Knoop et al. (2006), it is estimated that two electron

capture will mainly populate ($3\ell n'\ell'$, n'=5 – 7) configurations. The resulting energy defects would coincide with the feature observed in the TES spectra at energy defects of 20 – 30 eV (Seredyuk et al., 2005c).

This implies that the cross sections for double charge exchange ($O^{6+} \rightarrow O^{4+}$) measured by Mawhorter et al. (2007) should be largely attributed to auto-ionizing 3 electron capture reactions, rather than bound double electron capture reactions.

6.4 Conclusions

In the interaction between comets and the solar wind, collisions between the O^{6+} and and water play a key role. In this section, we have presented velocity dependent state selective and total one electron capture cross sections for collisions between O^{6+} and H_2O, at collision energies between 0.11 – 7.5 keV/amu. These energies correspond to velocities typical for the solar wind, i.e. 150 – 1200 km s^{-1}.

Our results show that single electron capture mainly leads to population of the $n = 4$ state and that the subsequent decay gives rise to strong EUV emission between 10 – 20 nm. The relative strength of the different EUV lines strongly depends on the collision velocity and might be used as a velocimetric diagnostic in comet-wind interactions, for example by observing the ratio between the $1s^2$3d–$1s^2$2p and $1s^2$4p–$1s^2$2s transitions.

We also used our data to determine total one electron capture cross sections. From a comparison with other experimental studies, we conclude that direct one electron capture cross section constitutes only 60% of the total charge changing cross section, and that multiple electron processes thus play an important role in collisions between O^{6+} and H_2O. These results emphasize that a thorough understanding of charge exchange processes is of utmost importance for modeling of solar wind charge state distributions in cometary and planetary atmospheres.

7 Charge Exchange Emission from H-like C and O Colliding on H_2O

Charge exchange emission in astrophysical environments is characterized by strong forbidden lines, and the relative strengths of the forbidden, resonance and intercombination lines following charge exchange are distinctly different from those due to other emission mechanisms (Kharchenko and Dalgarno, 2001). This has recently been demonstrated by Mars observations with XMM-*Newton* (Dennerl et al., 2006), which do resolve the OVII forbidden, resonance and intercombination lines. Using the relative strength of these lines, the observers were able to distinguish between fluorescence emission from the planetary disc and a CXE dominated halo due to solar wind interactions with the outer atmosphere.

The analysis of the Mars observations was based on the assumption that charge exchange populates the triplet and singlet states according to a statistical distribution, with a ratio of 3:1. Interestingly, no direct measurements or simulations of the collision systems of interest are available to support this assumption. The long lifetimes of the metastable states of solar wind ions make it very difficult to measure the resulting emission directly in a laboratory experiment. For example, the 2^3S state has a lifetime of 20 ms in CV, and 1 ms in OVII (Porquet and Dubau, 2000; Porquet et al., 2001). At typical solar wind velocities of 500 km s^{-1}, the ions cover a distance of 11 and 0.5 km, respectively.

Beiersdorfer et al. (2003) measured CXE spectra by trapping ions typical for the solar wind, and then injecting a target gas into the trap. The forbidden lines of He-like C, N and O were observed, but the experiment did not allow for direct measurement of the triplet-to-singlet (TS) ratio because of the mixing of the subshells induced by the large magnetic field used to trap the ions.

Suraud et al. (1991) investigated collisions between C^{5+} and H_2 by means of Far-UV Photon Emission Spectroscopy, which allowed for the direct measurement of some specific triplet and singlet emission cross sections. They measured a near to statistical TS population ratio of $\sigma_T/\sigma_S = 3.7$ at a collision energy of 4.3 keV/amu, which is close to the

statistical TS ratio. However, experiments with lower charged ions (O^{3+}, N^{4+}) and H and H_2 showed that at collision energies below 1 keV/amu, the TS-ratio changes significantly with decreasing collision energy (Beijers et al., 1996; Bliek et al., 1998). These findings are confirmed by theoretical simulations (Wang et al., 2002; Stancil et al., 1997). Preliminary theoretical results suggested a strong velocity dependence of the OVII triplet/singlet ratio for electron capture from helium (Krasnopolsky et al., 2004). Such an effect will have important consequences for the interpretation of CXE spectra if it also occurs with other collision targets, such as H_2O for comets.

Here, we present the first direct measurements of the velocity dependence of the ratio between capture into specific triplet- and singlet states following single electron capture (SEC) by H-like carbon and oxygen ions colliding with water molecules. These reactions can be summarized as:

$$A^{q+}(1s) + H_2O \rightarrow A^{(q-1)+}(1sn'\ell') + (H_2O)^+ \tag{7.1}$$

$$\rightarrow A^{(q-1)+}(1sn\ell) + (H_2O)^+ + h\nu \tag{7.2}$$

where the incoming projectile A^{q+} (C^{5+} or O^{7+}) captures one electron into an excited state $1sn'\ell'$, which subsequently decays to a lower lying state by emitting a photon.

The experiments are carried out in the energy range between $0.3-20q$ keV by means of photon emission spectroscopy, i.e., by detecting the extreme-ultraviolet photons emitted during the ions' relaxation (Chapter 4). The experiment therefore yields direct measurements of various EUV emission cross sections, from which by means of a spectroscopic analysis population cross sections are derived.

7.1 Atomic Structure of He-like ions

Because decay schemes work as a funnel, the lowest transitions ($n = 2 \rightarrow 1$) are the strongest emission lines in astrophysical CXE spectra. For helium-like ions, these are the forbidden line z (1^1S_0–2^3S_1), the intercombination lines y, x (1^1S_0–$2^3P_{1,2}$), and the resonance line w (1^1S_0–2^1P_1), see Fig. 7.1. For X-ray plasma diagnostics, two different ratios between these lines are used:

$$R = \frac{z}{x+y} \tag{7.3}$$

$$G = \frac{z+x+y}{w} \tag{7.4}$$

In electron collision dominated plasmas, the ratio R is sensitive to electron densities, and the ratio G to electron temperatures (Gabriel and Jordan, 1969). In the case of CXE, the G and R ratios solely depend on the initial $n\ell$-distribution and on the branching ratios of the ionic system of interest, and hence on the collision velocity and the electronic structure of the two colliding particles.

The apparent branching ratios for the decay of the 2^3P state are determined by weighting theoretical transition rates (Porquet and Dubau, 2000; Porquet et al., 2001) by an as-

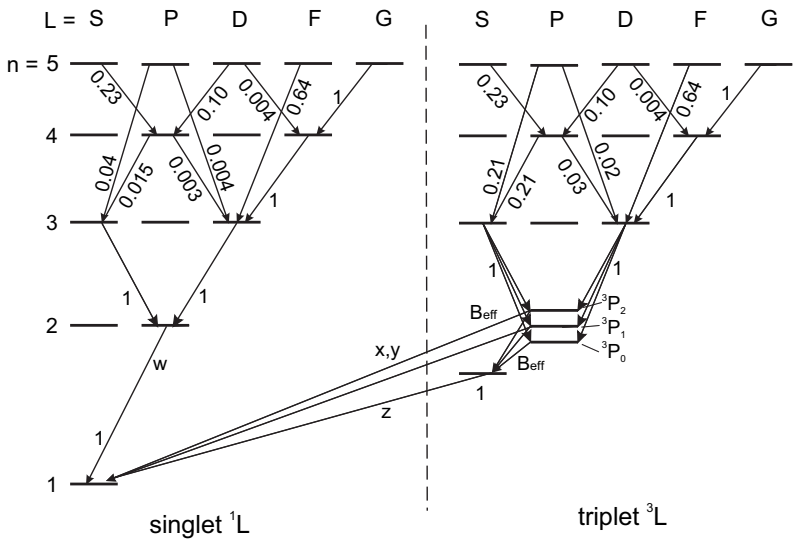

Figure 7.1: *Part of the decay scheme of a helium-like ion.*

Table 7.1: *Apparent effective branching ratios, B_{eff}, for the decay of the 2^3P state of He-like carbon and oxygen ions.*

transition	CV	OVII
1^1S_0–$2^3P_{1,2}$	0.11	0.30
2^3S_1–$2^3P_{0,1,2}$	0.89	0.70

sumed statistical population of the triplet P-term:

$$B_{eff} = \sum_{j=0}^{2} \frac{(2j+1)}{(2L+1)(2S+1)} \cdot \mathrm{B}_j \tag{7.5}$$

The resulting effective branching ratios are given in Table 7.1.

The ratio G is not equal to the overall triplet-to-singlet ratio, because in the singlet system the np-states decay to the ground state directly. G thus depends both on the triplet to singlet ratio, and on the initial distribution over the $n\ell$ states.

7.2 Analysis

7.2.1 C^{5+}

Charge exchange spectra following C^{5+}+H_2O collisions are complex and contain many emission lines. Equipped with a 1200 grooves/mm grating, our EUV spectrometer has a

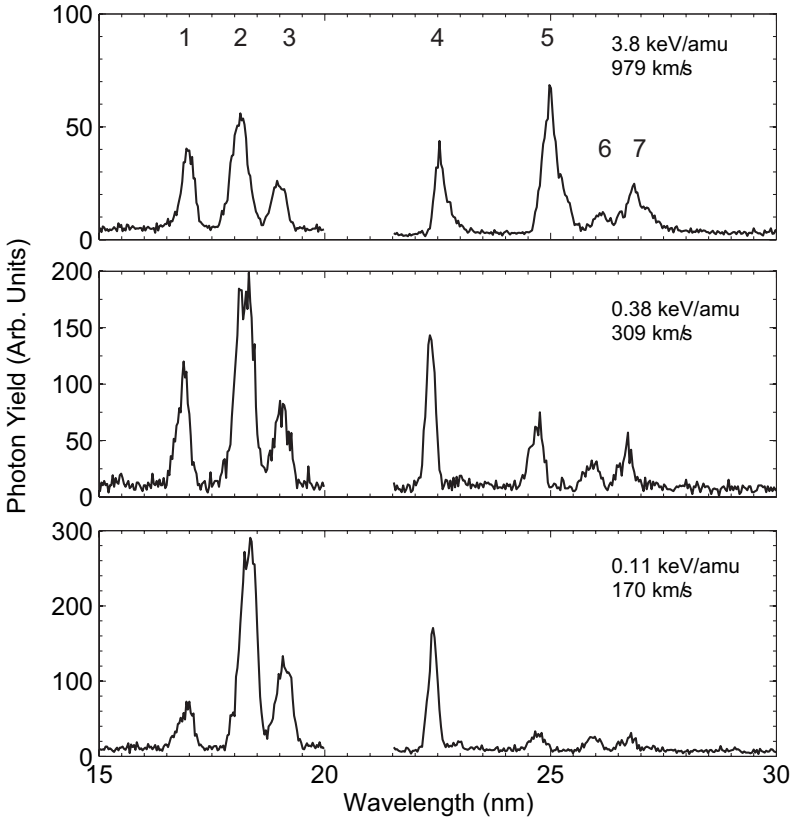

Figure 7.2: *Charge exchange spectra for collisions between C^{5+} and H_2O, at different velocities. The spectra are all on the same scale, i.e. corrected for the inlet pressure and integration time. The numbers above the figure refer to Table 7.4. The spectra are not corrected for the wavelength dependent sensitivity of the detection system.*

resolution of 0.3 nm FWHM, which is not enough to resolve every single emission line. All spectra were analyzed by fitting 7 Gaussian shaped peaks to the data (see Table 7.2). The resulting photon yields were converted to emission cross sections by calibrating via known cross sections for He^{2+}+H_2O (Seredyuk et al., 2005a; Bodewits et al., 2006).

The observed emission lines provide two independent, direct measures of the TS ratios: the ratio between the triplet and singlet 3d–2p transitions, H_3, and the ratio between the triplet and singlet 4s,d–2p transitions, H_4:

$$H_3 = \frac{\sigma(\mathrm{3d})_T + \sigma(\mathrm{4f})_T}{\sigma(\mathrm{3d})_S + \sigma(\mathrm{4f})_S} \tag{7.6}$$

$$H_4 = \frac{\sigma_{em}(\mathrm{4s-2p})_T + \sigma_{em}(\mathrm{4d-2p})_T}{\sigma_{em}(\mathrm{4s-2p})_S + \sigma_{em}(\mathrm{4d-2p})_S} \tag{7.7}$$

To obtain the H_3 ratio, the $\sigma(\mathrm{3d})^*_T$ population cross section should be corrected for cascade

Table 7.2: *Fit results - measured emission cross sections for collisions between C^{5+} and H_2O, at different collision energies. All cross sections are in units of 10^{-16} cm^2. Only relative errors are given. The systematic uncertainty is approximately 25%.*

#	λ (nm)	Transitions	Coll. energy (keV/amu)		
			0.113	0.375	3.75
1	17.3	4p–2s (T)	1.0 ± 0.1	0.7 ± 0.1	1.1 ± 0.1
2	18.8	4d–2p (T), 4s–2p (T), 4p–2s (S)	6.1 ± 0.6	2.0 ± 0.2	2.0 ± 0.2
3	19.8	4d–2p (S), 4s–2p (S)	2.5 ± 0.2	0.7 ± 0.1	0.8 ± 0.1
4	22.7	3p–2s (T)	14 ± 1.4	7.2 ± 0.7	4.4 ± 0.4
5	24.8	3d–2p (T), 3p–2s (S)	2.7 ± 0.3	4.0 ± 0.4	10 ± 1.0
6	26.0	3s–2p (T,S)	2.6 ± 0.3	1.9 ± 0.2	1.8 ± 0.2
7	26.7	3d–2p (S)	2.1 ± 0.2	2.4 ± 0.2	3.6 ± 0.4

population from the 4p-state in the triplet system, because this 4p-2s cascade transition is negligible in the singlet system:

$$\sigma(3d)^*_T = \sigma_{em}(3d-2p)_T - 0.04\sigma_{em}(4p-2s)_T \tag{7.8}$$

The observed emission lines also allow us to deduce emission cross sections for the K-series, observable in X-ray. To do this, we first assume that singlet np–2s transitions do not contribute significantly to the observed emission features, because these transitions have very small branching ratios compared to transitions directly to the ground state (less than 0.06 for $n = 3,4$). Close inspection of the measured spectra (Fig. 7.2) shows that there is no detectable 1s5p-1s2s line emission around 15.6 nm. It is therefore save to assume that contributions from capture into the $n = 5$ states are negligible. A third assumption is that the $n\ell$-distribution is equal in the triplet and singlet systems.

Kα line emission cross sections can then be estimated from the cascade population cross sections of the 1s2p($^3P_{1,2}$) and 1s2s($^3S_1$) states by using apparent branching ratios from Table 7.1

$$\sigma_{em}(x+y) = 0.11\sigma(2p)^*_T \tag{7.9}$$

$$\sigma_{em}(z) = \sigma(2s)^*_T \tag{7.10}$$

where the cascade population cross sections can be deduced from the measured emission cross sections:

$$\sigma(2s)^*_T = \sigma_{em}(4p-2s)_T + \sigma_{em}(3p-2s)_T + 0.89\sigma(2p)^*_T \tag{7.11}$$

$$\begin{aligned}\sigma(2p)^*_T = {} & \sigma_{em}(4s,d-2p)_T + \sigma_{em}(3d-2p)_T \\ & + 0.32\sigma_{em}(4p-2s)_T + \frac{H_3}{H_3+1}\sigma_{em}(3s-2p)_{ST}\end{aligned} \tag{7.12}$$

In a similar manner, the emission cross section of the resonance line is found from the population of the 1s2p($^1P_1$) state:

$$\sigma_{em}(w) = \sigma_{em}(4s,d-2p)_S + \sigma_{em}(3d-2p)_S + \frac{1}{H_3+1}\sigma_{em}(3s-2p)_{ST} \tag{7.13}$$

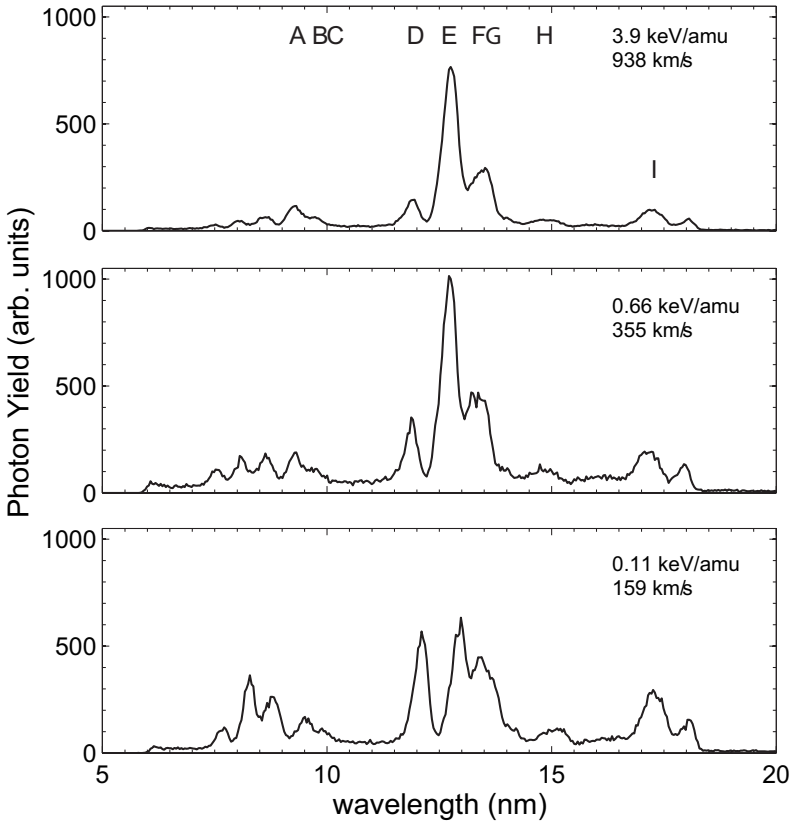

Figure 7.3: *Charge exchange spectra for collisions between O^{7+} and H_2O, at different velocities. The spectra are all on the same scale, i.e. corrected for the inlet pressure and integration time. The labels A-I refer to Table 7.3.*

With our spectrometer, the K-series cannot be observed directly. Emission cross sections for Kβ and Kγ lines can be estimated by weighting the triplet populations with the triplet-singlet ratio and the relevant branching ratios:

$$\sigma_{em}(3\mathrm{p}-1\mathrm{s})_S = \frac{1}{H_3}\cdot\sigma_{em}(3\mathrm{p}-2\mathrm{s})_T \tag{7.14}$$

$$\sigma_{em}(4\mathrm{p}-1\mathrm{s})_S = \frac{0.95}{0.76}\frac{1}{H_4}\cdot\sigma_{em}(4\mathrm{p}-2\mathrm{s})_T \tag{7.15}$$

Finally, total one electron capture cross sections can be estimated by:

$$\sigma_t = \sigma_{em}(w)+\sigma_{em}(x,y)+\sigma_{em}(z)+1.05\sigma_{em}(3\mathrm{p}-1\mathrm{s})_S+1.05\sigma_{em}(4\mathrm{p}-1\mathrm{s})_S \tag{7.16}$$

7.2.2 O^{7+}

The analysis of OVII spectra due to single electron capture by O^{7+} from H_2O molecules is even more complex than the CV spectra. More emission lines are present due to the fact that the higher charge state of the oxygen ion leads to population of the $n = 5,6$ shells. Typical spectra for charge exchange between H-like oxygen and H_2O are shown in Fig. 7.3. The data were analyzed by fitting 9 Gaussians to the spectra, see Table 7.5.

The spectra provide one independent measures J_3 of the TS ratio following one-electron capture:

$$J_3 = \frac{\sigma_{em}(3\mathrm{d}-2\mathrm{p})_T - 0.04\sigma_{em}(4\mathrm{p}-2\mathrm{s})}{\sigma_{em}(3\mathrm{d}-2\mathrm{p})_S} \tag{7.17}$$

In the singlet system, the 1s4p(^{1}P) state mainly relaxes directly to the ground state, whereas in the triplet system, a minor fraction cascades to the 1s3d(^{3}S) state. We therefore correct J_3 for this contribution by weighting the emission cross section of the 4p–2s(T) with the relevant branching ratio.

From these relations, the following emission cross sections can be derived for the K-series:

$$\sigma_{em}(\mathrm{K}\gamma) = \frac{0.93}{0.75}\frac{1}{J_3}\sigma_{em}(4\mathrm{p}-2\mathrm{s})_T \tag{7.18}$$

$$\sigma_{em}(\mathrm{K}\beta) = 0.95\frac{1}{J_3}\sigma_{em}(3\mathrm{p}-2\mathrm{s})_T \tag{7.19}$$

7.2.3 Uncertainties

The results are subject to a number of uncertainties. The dominating absolute uncertainty is that arising from the spectrometer's calibration by means of cross sections for CXE from He^{2+} ions, and is approximately 20% (Bodewits et al., 2006). This error affects all data points, and leads to a simple scaling factor. A more complex error is due to the uncertainty in the wavelength dependent sensitivity of the spectrometer, which we estimate to be 10 – 15%. Added in quadrature these uncertainties lead to an absolute systematic uncertainty of 25%. The uncertainty associated with the wavelength-dependent sensitivity may also influence the relative line strengths which are of importance when assessing cascade contributions. Target fluctuations were controlled by performing regular calibration measurements, but lead to a random error in the order of 5%. Statistical errors for these experiments were small due to high photon yields and never exceeded 1% (1σ). Therefore we assume a relative uncertainty of 10% in the line emission cross sections.

Table 7.3: *Fit results - measured emission cross sections for collisions between O^{7+} and H_2O, at different collision energies. All cross sections are in units of 10^{-16} cm^2. Only relative errors are given. The systematic uncertainty is approximately 25%.*

#	λ (nm)	Line(s)	Collision Energy (keV/amu)							
			0.13	0.22	0.66	1.3	2.6	3.3	3.9	4.6
A	9.1	4p–2s (T)	0.9 ± 0.1	0.8 ± 0.1	0.8 ± 0.1	0.9 ± 0.1	0.4 ± 0.1	0.7 ± 0.08	0.9 ± 0.09	0.9 ± 0.1
B	9.7	4s,d–2p (T), 4p–2s (S)	3.7 ± 0.4	3.4 ± 0.4	3.8 ± 0.4	3.4 ± 0.3	4.3 ± 0.4	3.2 ± 0.3	3.0 ± 0.3	3.0 ± 0.3
C	10.0	4s,d–2p (S)	1.7 ± 0.2	1.8 ± 0.2	1.6 ± 0.2	1.5 ± 0.2	1.7 ± 0.2	1.2 ± 0.1	1.2 ± 0.1	1.1 ± 0.1
D	12.0	3p–2s (T)	7.6 ± 0.8	6.8 ± 0.7	4.1 ± 0.4	2.8 ± 0.3	2.9 ± 0.3	2.1 ± 0.2	2.0 ± 0.2	2.1 ± 0.2
E	12.8	3d–2p (T), 3p–2s (S) .	7.6 ± 0.8	10 ± 1.0	13 ± 1.3	12 ± 1.2	15 ± 1.5	10 ± 1.0	9.8 ± 1.0	11 ± 1.1
F	13.3	3s–2p (T)	5.1 ± 0.5	5.3 ± 0.5	5.0 ± 0.5	3.8 ± 0.4	3.9 ± 0.4	3.1 ± 0.3	2.8 ± 0.3	2.8 ± 0.3
G	13.7	3s,d–2p (S)	3.3 ± 0.3	3.8 ± 0.4	4.3 ± 0.4	3.9 ± 0.4	4.4 ± 0.4	3.2 ± 0.3	3.2 ± 0.3	3.2 ± 0.3
H	15.0	OVI	0.7 ± 0.07	0.7 ± 0.08	0.6 ± 0.1	0.0 ± 0.00	0.5 ± 0.05	0.3 ± 0.03	0.4 ± 0.04	0.3 ± 0.03
I	17.3	OVI	3.0 ± 0.3	2.9 ± 0.3	1.6 ± 0.2	0.0 ± 0.0	1.5 ± 0.2	1.0 ± 0.10	0.8 ± 0.08	0.9 ± 0.1

7.3 Results and Discussion

7.3.1 Triplet-Singlet Ratios

The measured velocity dependence of the accessible CXE triplet to singlet ratios is shown in Fig. 7.4. Our measurements show that in collisions between H-like carbon and oxygen with water, singlet and triplet states are populated statistically at high velocities. At low collision velocities, all TS ratios are significantly lower than 3. In particular the CV H_3 ratio decreases quickly with decreasing velocity, and this effect should be observable at normal slow solar wind interactions (300km s^{-1} or 0.5 keV/amu).

Unfortunately, there exists no simple model to describe TS ratios. Parallel to the distribution over the l-shells, it is to expected that at low velocities, capture cross sections become more and more dependent on the exact nature of the state (binding energies, angular momentum). Qualitatively we find a statistical distribution at high velocities, whereas at low velocities, all measured TS ratios decrease significantly below 3.

7.3.2 Partial Cross Sections

C^{5+} – The result of our spectral analysis are shown in Tables 7.4 and 7.5 for C^{5+} and O^{7+}, respectively. The EUV CXE spectra of CV allow for the derivation of emission cross sections of all the lines detectable in X-ray (i.e. the K-series, the forbidden line and the intercombination line). The Classical Over-the-Barrier model shows that capture into $n = 4$ is nearly resonant (Fig. 7.5).

In Fig. 7.7 our results are compared with theoretical state selective, velocity dependent cross sections for collisions of bare ions with atomic hydrogen (Errea et al., 2004; Fritsch and Lin, 1984; Green et al., 1982; Shipsey et al., 1983), see Chapter 8. At high velocities, the results for C^{5+} are in good agreement with the theoretical cross sections, but at lower velocities the theoretical cross sections underestimate the emission cross sections. At velocities typical for the slow solar wind (300 km s^{-1}), the most important features (i.e. the CV w, x, y and z lines) are underestimated by a factor of approximately 1.5. The Kβ might be underestimated more, but is only a minor contributor to emission in astrophysical environments.

O^{7+} – The OVII spectrum contains too many unresolved lines to allow for an analysis comparable to that of the C^{5+} data. In particular, the spectral resolution of our experiment is not sufficient to resolve all the $n = 5$ and $n = 6$ lines that are present below 9 nm. Nevertheless, some general trends can be observed. From the Classical Over-the-Barrier model, it is to be expected that capture into $n = 5$ is the dominant reaction channel (Fig. 7.5). Hasan et al. (2001) measured the n-distribution at 2 keV/amu and observed indeed that most capture occurs into $n = 5$ (85%), and capture into n=4 and n=6 contribute 14% and 1.4%, respectively.

Emission cross sections of the Kβ and Kγ lines were derived from the spectra. Compared to theory for bare nitrogen ions colliding on H (Fig. 7.7), the presented emission cross sections are roughly a factor of 2 smaller. Greenwood et al. (2001) directly measured emission cross sections for $O^7+ + H_2O$ with an X-ray spectrometer. For a collision energy of 2.7 keV/amu, they found much larger emission cross sections of (3.0 ± 0.4) and

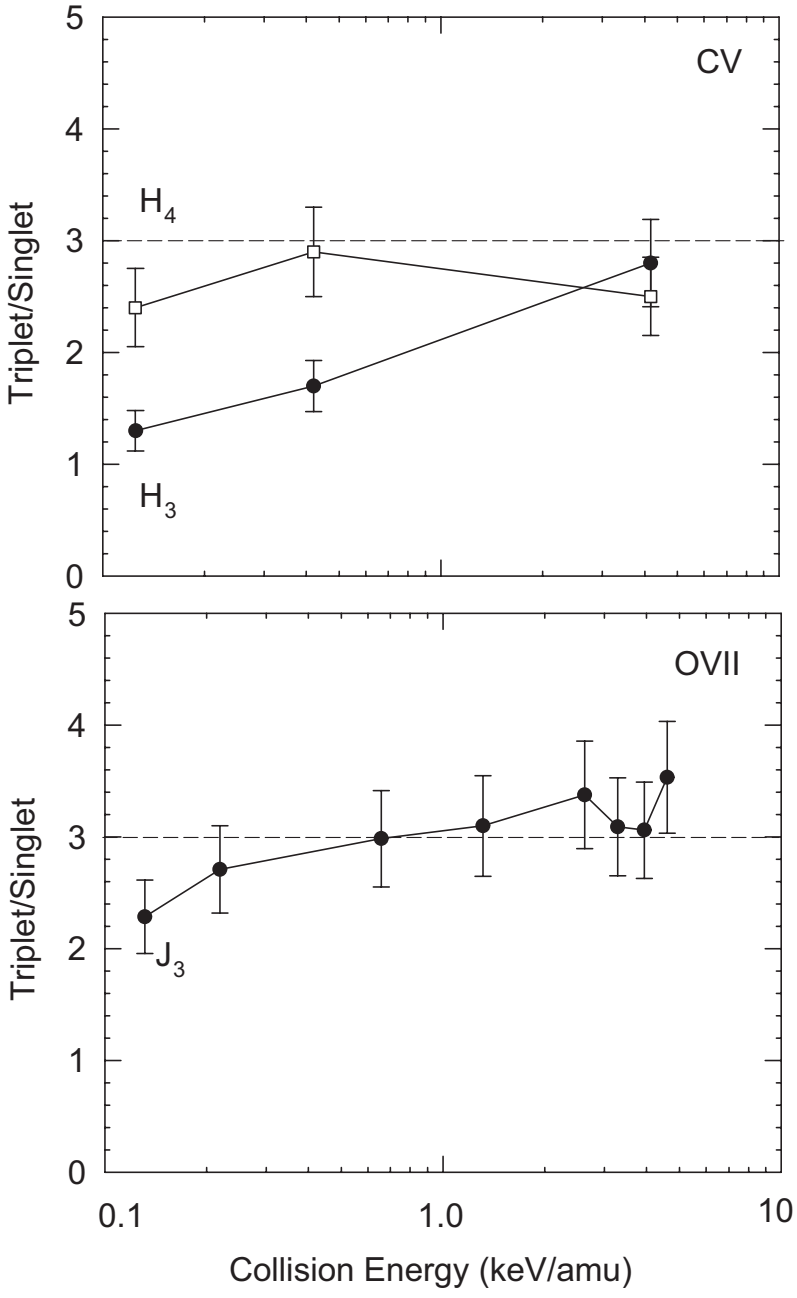

Figure 7.4: *Triplet to singlet ratios for charge exchange between C^{5+} and H_2O (upper panel) and O^{7+} and H_2O (lower panel) for different collision energies. Lines are drawn to guide the eye. The dashed line indicates the statistical triplet to singlet ratio (3).*

Table 7.4: *Triplet-singlet ratios, emission cross sections and total one electron capture cross sections for collisions between C^{5+} and H_2O, at different collision energies. All cross sections are in units of 10^{-16} cm^2. Only relative errors are given. The systematic uncertainty is approximately 25%.*

Coll. energy (keV/amu)	0.113	0.375	3.75
Velocity (km s^{-1})	170	309	979
H_3	1.3 ± 0.2	1.7 ± 0.2	2.8 ± 0.4
H_4	2.4 ± 0.4	2.9 ± 0.4	2.5 ± 0.4
x+y	1.2 ± 0.08	0.8 ± 0.05	1.5 ± 0.1
z	24 ± 1.5	14 ± 0.9	18 ± 1.0
w	5.8 ± 0.4	3.8 ± 0.3	4.9 ± 0.4
Kβ	11 ± 1.9	4.4 ± 0.8	1.6 ± 0.3
Kγ	0.5 ± 0.1	0.3 ± 0.04	0.6 ± 0.1
Total	43 ± 2.6	24 ± 1.2	26 ± 1.2

$(3.5 \pm 0.6) \times 10^{-16}$ cm^2 for the Kβ and Kγ, respectively.

7.3.3 Total Cross Sections

Total charge changing cross sections for C^{5+}+H_2O collisions have recently been measured by Mawhorter et al. (2007). They measured a charge changing cross section of $(42 \pm 3.2) \times 10^{-16}$ cm^2. This is much larger than the one electron capture cross sections measured by us at comparable energies, which by interpolation would be $(25 \pm 6.6) \times 10^{-16}$ cm^2. This difference can only be attributed to auto-ionizing double electron capture (A2C) processes. Such processes most likely populate either the ground state or the first excited state of CV, as A2C -enhanced population of the $n = 3$ state would have been directly observable in our PES experiments. For two electron charge transfer, Mawhorter et al. (2007) measured a cross section of $(6.0 \pm 1.0) \times 10^{-16}$ cm^2. According to our interpretation, the auto-ionizing double electron capture cross section would be approximately $(17 \pm 7.3) \times 10^{-16}$ cm^2, or roughly a factor of 3 larger than the cross section for bound double electron capture. As in the case of O^{6+} + H_2O collisions (see Chapter 6) the cross section for twofold charge

Table 7.5: *Triplet-singlet ratios, emission cross sections and total one electron capture cross sections for collisions between O^{7+} and H_2O, at different collision energies. All cross sections are in units of 10^{-16} cm^2. Only relative errors are given. The systematic uncertainty is approximately 25%.*

E (keV/amu)	0.13	0.22	0.66	1.3	2.6	3.3	3.9	4.6
v (km s^{-1})	159	205	355	501	709	793	868	938
J_3	2.3 ± 0.3	2.7 ± 0.4	3.0 ± 0.4	3.1 ± 0.4	3.4 ± 0.5	3.1 ± 0.4	3.1 ± 0.4	3.5 ± 0.5
Kγ	0.5 ± 0.1	0.4 ± 0.1	0.3 ± 0.1	0.4 ± 0.1	0.2 ± 0.03	0.3 ± 0.1	0.4 ± 0.1	0.3 ± 0.1
Kβ	3.2 ± 0.6	2.4 ± 0.5	1.3 ± 0.3	0.8 ± 0.2	0.8 ± 0.2	0.7 ± 0.2	0.6 ± 0.2	0.6 ± 0.2

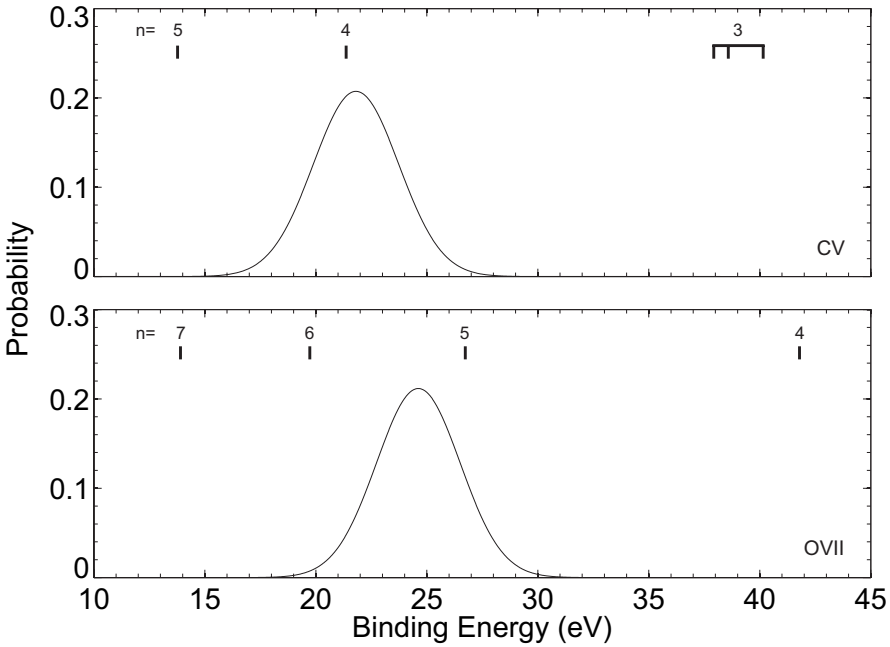

Figure 7.5: *Classical Over-the-Barrier reaction windows for single electron capture by C^{5+} (top panel) and O^{7+} (lower panel) from H_2O.*

transfer measured by Mawhorter et al. (2007) is most likely due to 3 (or more) electron transfer.

Our experiment ensures single collision conditions, and the OVI emission detected allow for an estimate of double electron capture cross sections. The spectra show the presence of OVI $1s^2 3p–1s^2 2s$ (15.0 nm) and $1s^2 3d–1s^2 2p$ (17.3 nm) emission lines. The emission cross sections of both lines decrease with increasing collision velocity. Adding the two emission cross sections together, we find the minimum cross section for bound double electron capture to decrease from $(3.7 \pm 1.0) \times 10^{-16}$ cm^2 at 0.13 keV/amu to $(1.2 \pm 0.3) \times 10^{-16}$ cm^2 at 4.6 keV/amu.

It is interesting to compare these results with Over-the-Barrier predictions and charge changing measurements. Greenwood et al. (2001) measured one, two- and threefold charge changing cross sections of $\sigma_{q,q-1} = (53 \pm 1) \times 10^{-16}$ $\sigma_{q,q-2} = (8 \pm 1) \times 10^{-16}$ and $\sigma_{q,q-3} < 3 \times 10^{-16}$ at collision energies of 2.72 keV/amu. Our lower limit for bound double capture cross sections is about 40% smaller than the double charge changing cross section of Greenwood et al. (2001). These results seem consistent with ours, in particular given that we observed only the strongest OVI emission lines.

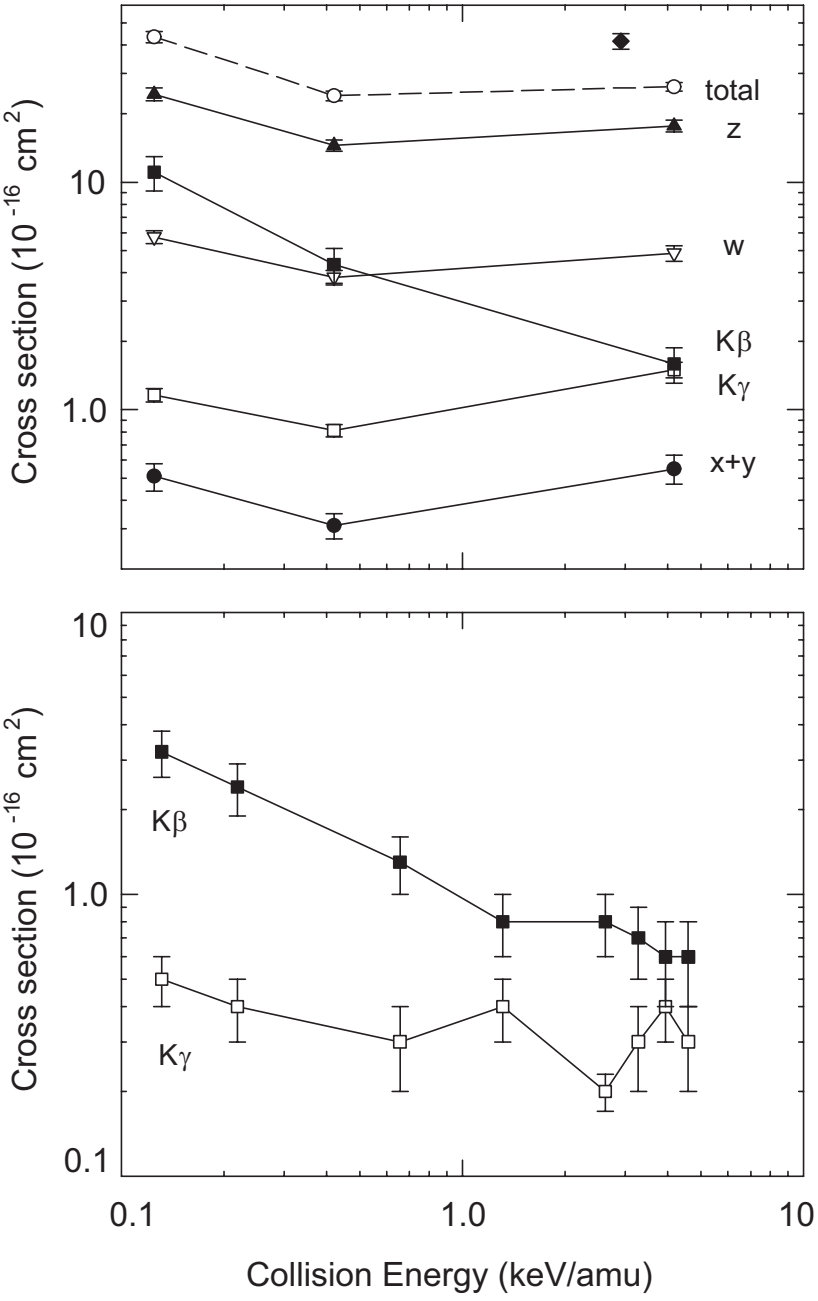

Figure 7.6: *Velocity dependence of X-ray emission cross sections.* ***Top panel:*** C^{5+} + H_2O. *Indicated are* ▲ *– z;* ▽ *– w;* □ *– x + y;* ■ *– Kβ;* ● *–Kγ and the total one electron capture cross section* ○ *–*σ_t*;* ♦ *– total charge changing cross section (Mawhorter et al., 2007).* ***Lower panel:*** O^{7+} + H_2O. *Indicated are:* ■ *– Kβ;* ● *–Kγ. Lines are drawn to guide the eye, and only relative errors are given. The systematic uncertainty is approximately 25%.*

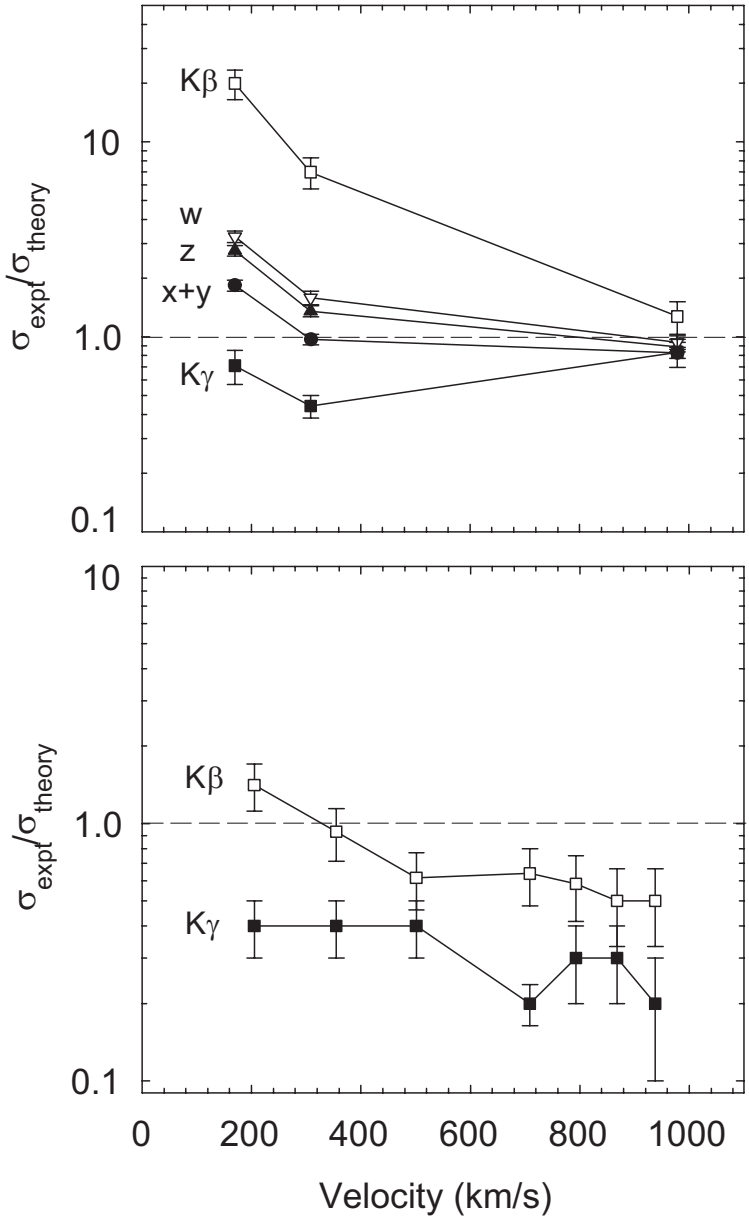

Figure 7.7: *Ratio between experimentally obtained cross sections and theoretical cross sections for bare ions colliding on H, see text.* ***Top panel:*** *C^{5+} + H_2O. Indicated are ▲ − z; ▽ − w; □ − x + y; ■ − Kβ; ● − Kγ.* ***Lower panel:*** *O^{7+} + H_2O. Indicated are: ■ − Kβ and ● − Kγ. Lines are drawn to guide the eye, and only relative errors are given. The systematic uncertainty is approximately 25%.*

Table 7.6: *Ionization potentials and resulting Over-the-Barrier predictions for capture distances and geometrical cross sections.*

#	IP_n (eV)	C^{5+}		O^{7+}	
		$R_{c,n}$ (a.u.)	σ_n (Å^2)	$R_{c,n}$ (a.u.)	σ_n (Å^2)
1	12.6	11.8	33	13.6	45
2	27	8.0	9	9.1	12
3	~45	6.5	19	7.4	24

7.4 Conclusions

Cometary X-ray spectra are dominated by the forbidden lines of H-like C and O following charge exchange with water and its dissociation products. The relative strength of these lines are determined by the distribution over triplet and singlet states into which the electrons are captured. We performed experimental studies of O^{7+} and C^{5+} colliding on water vapor and for the first time measured triplet-singlet population ratios. At high collision velocities, both the OVII and CV states are populated statistically. At lower velocities however, the ratios decrease significantly below 3. This effect is the strongest for CV, and this might be directly observable in interactions between comets and the slow solar wind.

From comparison with existing measurements, our results also allowed for a reconstruction of the relevant electron capture channels. Our findings are consistent with earlier experiments (Chapter 6) and show once again that auto-ionizing processes play an important role in charge transfer reactions.

8 Charge Exchange Emission Model

Several models are currently available to simulate cometary charge exchange emission. These models can be roughly qualified as either macroscopic, simulating the magneto-hydrodynamical interaction (Haberli et al., 1997; Wegmann et al., 1998, 2004) or microscopic, simulating the X-ray spectrum of comets by following the relaxation of the solar wind ions (Schwadron and Cravens, 2000; Kharchenko and Dalgarno, 2000, 2001; Beiersdorfer, 2003; Bodewits et al., 2004). From these models, and from recent observations with Chandra it has become clear that cometary high-energy emission depends upon certain properties of both the comet (gas production rate, composition, distance to the Sun) and the solar wind (speed, composition). We will briefly describe our model here and show how EUV observations of comets can be linked to cometary and solar wind properties.

Comets are generally considered cold, dusty snowballs from which volatile gases start to sublimate as they approach the Sun. When a comet enters the inner parts of the solar system, it will heat up so that different species can sublimate from the nucleus. These gases stream away from the nucleus until they are dissociated or ionized by solar radiation. The lifetime in the solar radiation field varies greatly amongst species typical for cometary atmospheres (Huebner et al., 1992). The dissociation and ionization scale lengths depend on the distance to the Sun. Generally, water molecules are confined to the inner regions of the coma, whereas the outer regions are populated by atomic dissociation products H and O and molecules that are more stable in sun light, such as CO.

We will assume that a comet with a production rate Q has a spherically expanding neutral coma. The coma interacts with solar wind ions, penetrating from the sunward side following straight line trajectories. The charge exchange processes between solar wind ions and coma neutrals are explicitly followed both in the change of the ionization state of the solar wind ions and in the relaxation cascade of the excited ions.

8.1 Atmosphere Model

The density distribution of different cometary species and their dissociation products is calculated with a standard Haser model (Haser, 1957; Festou, 1981). The comet's distance to the Sun determines the velocity of the out flowing molecules and their photo-destruction and photo-ionization rates (Huebner et al., 1992). The spatial extent and elemental distribution of the cometary neutral cloud is therefore primarily determined by the solar radiation field. Water and hydroxyl molecules have very short lifetimes compared with CO, H and O so that the inner regions of the coma consist mainly of water vapor, while the outer regions are populated with water dissociation products and molecules which are more stable sun light. This is illustrated in Fig. 8.1, which shows the neutral density profiles for the comets Halley at 1 AU (Q= 7×10^{29} molecules/s of which 5% CO – (Goldstein et al., 1987; Fuselier et al., 1991)) and Hale-Bopp at 3 AU (Q= 6×10^{29} molecules/s of which 30% CO and 10% CO_2 – (Biver et al., 1997)). In both cases, the inner regions of the cometary gas cloud are dominated by molecules, in particular H_2O, while the regions outside 10^5 km from the nucleus are dominated by atomic H and O. Hale-Bopp was a carbon-rich comet and has a large CO abundance throughout its coma. Halley was carbon-poor and much closer to the Sun. The outer regions of its coma can be seen to be dominated by the atomic products of water dissociation.

8.2 Interaction Model

The second step in the model is to track the evolution of the charge state distribution (CSD) of the ions along their trajectories. We assume that the ions follow straight line trajectories, parallel to the Sun-comet axis. Because of the cylindrical symmetry of the system only the distance traveled through the coma (s) and the distance to the Sun-comet axis (b) need to be considered. The charge state distribution of the helium ions is given by the following differential equations, where N^{q+} is the flux of a particular charge state and n_i and σ_i denote the number density and cross section of each atmospheric species:

$$\frac{dN^{2+}(s,b)}{ds} = -N^{2+}(s,b)\sum_i n_i(s,b)\times (\sigma_{sec,i}+\sigma_{bdc,i}) \tag{8.1}$$

$$\frac{dN^{1+}(s,b)}{ds} = N^{2+}(s,b)\sum_i n_i(s,b)\sigma_{sec,i} - N^{1+}(s,b)\sum_i n_i(s,b)\sigma_{seq,i} \tag{8.2}$$

$$\frac{dN^{0+}(s,b)}{ds} = N^{2+}(s,b)\sum_i n_i(s,b)\sigma_{b2c,i} + N^{1+}(s,b)\sum_i n_i(s,b)\sigma_{seq,i} \tag{8.3}$$

When the solar wind first interacts with a cometary atmosphere, it is both decelerated and

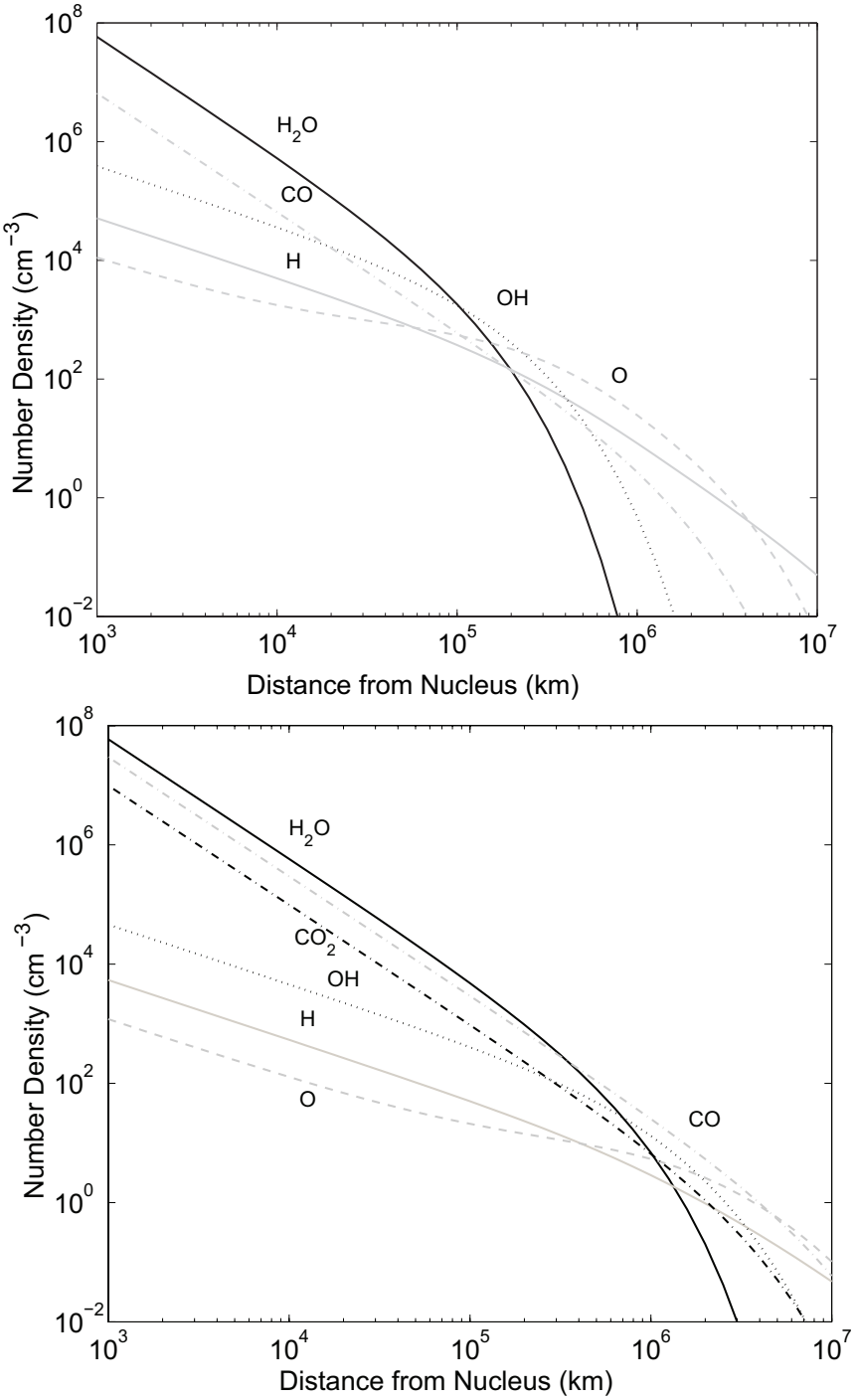

Figure 8.1: *Neutral density distribution as a function of the distance from the cometary nucleus for comets Halley (top) and Hale-Bopp (bottom), at heliocentric distances of 1.0 and 3.1 AU, respectively.*

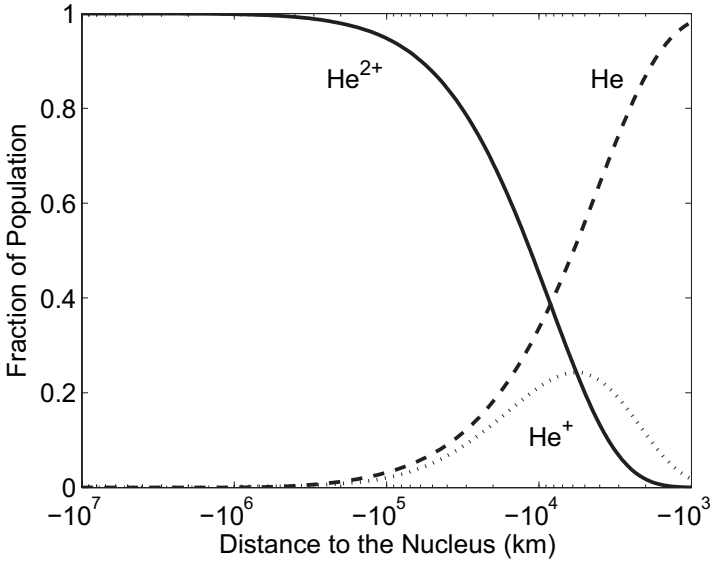

Figure 8.2: *Helium charge state distribution along the comet-Sun axis for comet Halley.*

heated in the bow shock. This bow shock does not affect the ionic charge state distribution. Wegmann et al. (2004) derived a rule of thumb based on mass loading length scales, that can be used to estimate the stand-off distance R_{bs} of the bow shock:

$$R_{bs} \geq (\gamma^2 - 1)\frac{\alpha m_C Q}{4\pi w F(\infty)} \tag{8.4}$$

where γ is the adiabatic index ($\gamma = 5/3$), $F(\infty)$ is the initial solar wind proton flux, Q is the comet's mass loss rate, w is the velocity of the out flowing gas, m_C is the average mass of a cometary ion and α is the average ionization rate Schmidt and Wegmann (1982).

After the bow shock, the drift velocity of the solar wind velocity is given as:

$$v_d = 0.25 v_d(\infty) \tag{8.5}$$

The kinetic energy released by decelerating the wind is converted into thermal energy. The most probable velocity of the corresponding Maxwellian distribution is given by:

$$v_{th} = \sqrt{v_{th}^2(\infty) + \frac{9}{16} v_d^2(\infty)} \tag{8.6}$$

Deep within the coma, the solar wind finally cools down as the hot wind ions, neutralized by charge exchange, are replaced by cooler cometary ions. For simplicity however, we shall assume that the wind keeps a constant velocity and temperature after crossing the bow shock.

Initially, all solar wind helium is ionized. Using our laboratory charge exchange cross sections, we can now solve Eq. 8.3 to find the charge state distribution. Fig. 8.2 shows the charge state distribution along the comet-Sun axis for comet Halley for a wind with an initial velocity of 370 km/s. The helium ions clearly penetrate deep into the coma. Most of the charge exchange reactions take place between $10^5 - 10^3$ km from the nucleus. A population of He^+ can be seen to build up around 10^4 km, a feature that was also observed in the *Giotto* mission through comet Halley's coma (Goldstein et al., 1987; Fuselier et al., 1991; Bodewits et al., 2004).

Once the charge state distribution in the coma is known, the emission coefficients j (in units of $cm^{-3}s^{-1}ster^{-1}$) for line emission at 30.4 and 58.4 nm are found by introducing line emission data:

$$j_{304}(s,b) = \frac{1}{4\pi} N^{2+}(s,b) \sum_i n_i(s,b)\sigma_{em,i}(304) \tag{8.7}$$

$$\begin{aligned} j_{584}(s,b) = &\frac{1}{4\pi} N^{2+}(s,b) \sum_i n_i(s,b)\sigma_{em,i}(584) \\ &+ \frac{1}{4\pi} N^{1+}(s,b) \sum_i n_i(s,b)\sigma_{em,i}(seq,584) \end{aligned} \tag{8.8}$$

where the cross sections are Maxwellian averaged emission cross sections $\sigma_{em}(v_d, v_{th})$. Temperatures in the solar wind are around 10^5 K, which for He^{2+} ions corresponds to a velocity of 50 km/s. This velocity is relatively small compared to the drift velocity of the solar wind (200 – 700 km/s). However when interacting with cometary atmospheres, the wind is both decelerated and heated in a bow shock. Because the heating is significant and the drift velocity is strongly reduced, the full velocity distribution needs to be considered. The Maxwellian averaged cross section can be found by applying the following relations:

$$<\sigma>=\frac{<\sigma v>}{<v>} \tag{8.9}$$

where

$$<\sigma v>= 2\pi \int_0^\infty \int_0^\pi \sigma(v) v^3 f(v,\theta) \mathrm{d}v \sin\theta \mathrm{d}\theta$$

and

$$f(v,\theta) = \left(\frac{m}{2\pi kT}\right)^{\frac{3}{2}} \exp\left[-\frac{m}{2kT}(v_d^2 + v^2 - 2v_d v\cos\theta)\right]$$

To illustrate the effect of a broad Maxwellian distribution on the cross sections, figure 8.3 shows Maxwellian averaged cross sections for different temperatures as a function of drift velocity. For low drift velocities (≤400 km/s) effects of the Maxwellian velocity distribution become of importance for temperatures above 10^6 K. At higher drift velocities the effects are marginal.

A 3D integration assuming cylindrical symmetry around the comet-Sun axis finally yields the absolute intensity of the emission lines. Effects due to the observational geometry (i.e. field of view and phase angle) are included at this step in the model.

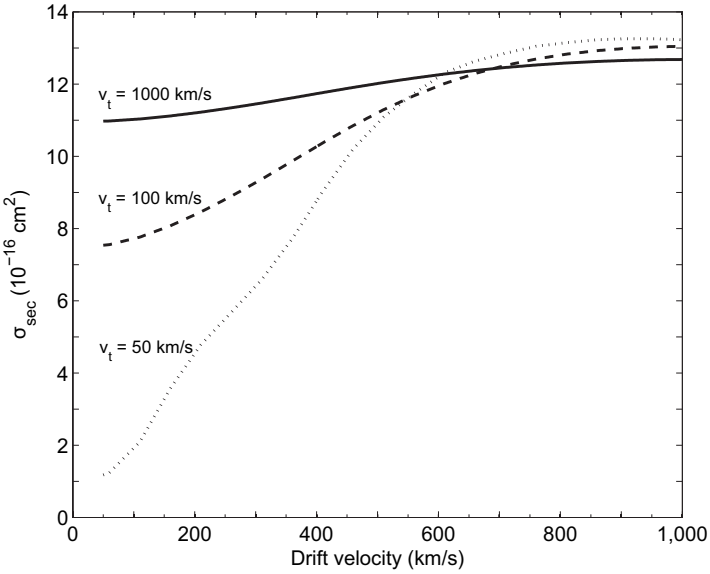

Figure 8.3: *Drift velocity dependence of maxwellian averaged total one electron capture cross sections of He^{2+} on H_2O. The velocities are equivalent to temperatures of 1.6×10^8 K, 1.6×10^6 K and 4×10^5 K, respectively.*

8.3 Heavy Ions

8.3.1 Atomic Structure of He-like Ions

Electron capture by highly charged ions populates highly excited states, which subsequently decay to the ground state. These cascading pathways follow ionic branching ratio statistics. Because decay schemes work as a funnel, the lowest transitions ($n = 2 \rightarrow 1$) are the strongest emission lines in CXE spectra. For helium-like ions, these are the forbidden line (z: $1s^2\ ^1S_0$–$1s2s\ ^3S_1$), the intercombination lines (y, x: $1s^2\ ^1S_0$–$1s2p\ ^3P_{1,2}$), and the resonance line (w: $1s^2\ ^1S_0$–$1s2p\ ^1P_1$), see Fig. 8.4.

The apparent branching ratio, B_{eff}, for the intercombination transitions is determined by weighting branching ratios (B_j) derived from theoretical transition rates (Porquet and Dubau, 2000; Porquet et al., 2001) by an assumed statistical population of the triplet P-term:

$$B_{eff} = \sum_{j=0}^{2} \frac{(2j+1)}{(2L+1)(2S+1)} \cdot B_j \tag{8.10}$$

The resulting effective branching ratios are given in Table 8.1. These ratios can only be observed at conditions where the metastable state is not destroyed (e.g. by UV flux or collisions) before it decays. In contrast to many other astrophysical X-ray sources, this

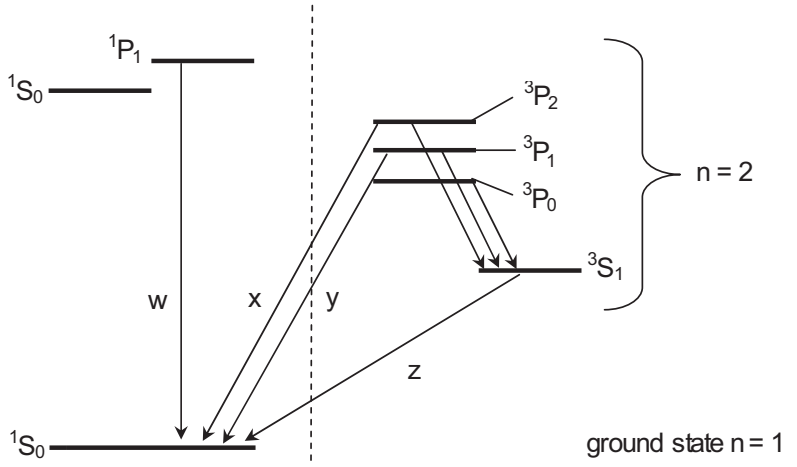

Figure 8.4: *Part of the decay scheme of a helium-like ion. The $^1S_0$ decays to the ground state via two-photon processes (not indicated).*

Table 8.1: *Apparent effective branching ratios (B_{eff}) for the relaxation of the 2^3P-state of He-like carbon, nitrogen, oxygen and neon.*

transition	CV	NVI	OVII	NeIX
$1s^2$ ($^1S_0$)–1s2p ($^3P_{1,2}$)	0.11	0.22	0.30	0.34
1s2s ($^3S_1$)–1s2p ($^3P_{0,1,2}$)	0.89	0.78	0.70	0.66

condition is fulfilled in cometary atmospheres, making the forbidden lines strong markers of CXE emission.

8.3.2 Emission Cross Sections

To obtain line emission cross sections we start with an initial state population based on state selective electron capture cross sections and then track the relaxation pathways defined by the ion's branching ratios.

Electron capture reactions can be strongly dependent on target effects. An important difference between reactions with atomic hydrogen and the other species is the presence of multiple electrons, hence allowing for multiple (mostly double) electron transfer. It has been demonstrated both experimentally and theoretically that double electron capture can be an important reaction channel in multi-electron targets and that after autoionization to an excited state it may contribute to the X-ray emission (Ali et al., 2005; Hoekstra et al., 1989; Beiersdorfer et al., 2003; Otranto et al., 2006; Bodewits et al., 2006). Unfortunately, experimental data on reactions with species typical for cometary atmospheres, such as H_2O, atomic O and CO are at best scarcely available. Because the first ionization potentials of these species are all close to that of atomic H, using theoretical state

selective one electron capture cross sections for bare ions charge exchanging with atomic hydrogen from theory is a reasonable approach, which is also confirmed by experimental studies (Greenwood et al., 2000, 2001; Bodewits et al., 2006). Here, we will use the working hypothesis that effective one electron cross sections for multi-electron targets present in cometary atmospheres are at least roughly comparable to cross sections for one electron capture from H. Based on this hypothesis, we will use our comet-wind interaction model to evaluate the contribution of the different species.

For our calculations, we use a compilation of theoretical state selective, velocity dependent cross sections for collisions with atomic hydrogen (Errea et al., 2004; Fritsch and Lin, 1984; Green et al., 1982; Shipsey et al., 1983). We furthermore assume that capture by H-like ions leads to a statistical triplet to singlet ratio of 3:1, based on measurements by Suraud et al. (1991) and Bliek et al. (1998). We will first focus on the strongest emission features, which are the $n = 2 \rightarrow 1$ transitions, i.e. the Ly-α transition (H-like ions) or the forbidden, resonance and intercombination lines (He-like ions).

In Fig. 8.5, the emission cross sections of the Ly-α or the sum of the emission cross sections of the forbidden, resonance and intercombination lines of different ions (C, N, O) are shown as a function of collision velocity, for one electron capture reactions with atomic hydrogen. This figure sets the stage for solar wind velocity induced effects in cometary X-ray spectra. Most important is the effect of the velocity on the two carbon emission features; their prime emission features increase by a factor of almost two when going from typical 'slow' to typical 'fast' solar wind velocities. The OVIII Ly-α emission cross section can be seen to drop steeply below approximately 300 km s^{-1}. The NVI Kα displays a similar, though somewhat less strong behavior.

The relative intensity of the emission lines (per species) is governed by the state selective electron capture cross sections of the charge exchange reaction and the branching ratios of the resulting ion. A measure of these intensities is the hardness ratio (Beiersdorfer et al., 2001), which is defined as the ratio between the emission cross sections of the higher order terms of the Lyman-series and the Ly-α (or between the higher order K-series and the Kα in case of He-like ions):

$$\frac{\sum_{n>2}^{\infty} \sigma_{em}(\text{Ly}-n)}{\sigma_{em}(\text{Ly}-\alpha)} \tag{8.11}$$

For electron capture by H-like ions, we will use the ratio between the sum of the resonance, intercombination and forbidden emission lines and the rest of the K-series as the hardness ratio. Fig. 8.5 shows the hardness ratios of CXE from abundant solar wind ions. The figure shows that most hardness ratios are constant at typical solar wind velocities (above 300 km s^{-1}) but it also clearly demonstrates the suggestion made by Beiersdorfer et al. (2001) that hardness ratios are good candidates for studies of velocimetry deep within the coma when the solar wind has slowed down by mass loading.

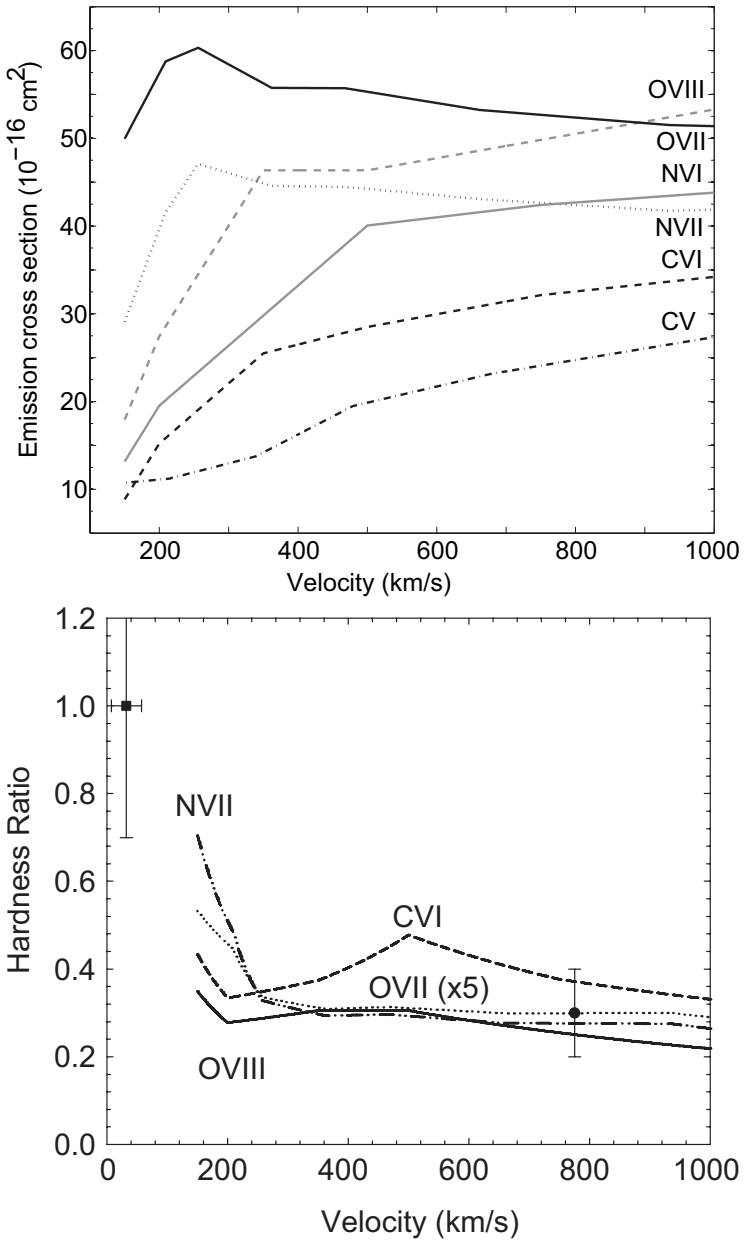

Figure 8.5: ***Upper panel:*** *Velocity dependence of Ly-α or the sum of the forbidden/resonance/intercombination emission cross sections of different solar wind ions: OVIII (dashed, grey line), OVII (solid, black line), NVII (dotted, black line), NVI (solid, grey line), CVI (dashed, black line) and CV (dash-dotted, black line).* ***Lower panel:*** *Velocity dependence of the hardness ratio of different solar wind ions: OVIII (solid line), OVII (dashed line) NVII (dashed line) and CVI (dash-dotted line). Also shown are two experimentally obtained hardness ratios by Beiersdorfer et al. (2001b) and Greenwood et al. (2000) for O^{8+} colliding on CO_2 and H_2O, respectively (see text).*

Table 8.2: *Compilation of theoretical, velocity dependent emission cross sections for collisions between bare- and H-like solar wind ions and atomic hydrogen, in units of 10^{-16} cm^2. See text for details. We estimate uncertainties to be approximately 20%. The ion column contains the resulting ion, not the original solar wind ion. Line energies compiled from Garcia and Mack, 1965; Vainshtein and Safronova, 1985; Drake, 1988; Savukov et al., 2003 and the CHIANTI database (Dere et al., 1997; Landi et al., 2006).*

E (eV)	Ion	Transition	200 km s^{-1}	400 km s^{-1}	600 km s^{-1}	800 km s^{-1}	1000 km s^{-1}
299.0	CV	z	8.7	12	16	18	20
304.4	CV	x,y	0.65	1.0	1.5	1.7	1.8
307.9	CV	w	1.8	3.0	4.1	4.8	5.2
354.5	CV	1s3p–1s^2 .	0.55	0.71	0.81	1.0	1.3
367.5	CV	1s4p–1s^2 .	0.70	0.66	0.76	0.74	0.72
367.5	CVI	2p–1s	15	26	30	33	34
378.9	CV	1s5p–1s^2 .	0.00	0.02	0.05	0.04	0.04
419.8	NVI	z	13	23	28	29	29
426.3	NVI	x,y	2.7	4.3	5.3	5.7	6.0
430.7	NVI	w	3.8	6.0	7.4	8.1	8.5
435.5	CVI	3p–1s	1.6	4.0	4.7	4.7	4.8
459.4	CVI	4p–1s	2.9	5.9	7.0	6.4	6.0
471.4	CVI	5p–1s	0.55	1.0	1.3	0.85	0.54
497.9	NVI	1s3p–1s^2 .	0.43	0.99	1.3	1.3	1.3
500.3	NVII	2p–1s	40	45	44	42	42
523.0	NVI	1s4p–1s^2 .	0.81	1.6	1.9	1.8	1.7
534.1	NVI	1s5p–1s^2 .	0.14	0.31	0.33	0.21	0.14
561.1	OVII	z	37	34	33	32	31
568.6	OVII	x,y	10	10	10	9.9	9.7
574.0	OVII	w	9.9	11	11	11	10
592.9	NVII	3p–1s	6.3	4.9	4.8	4.5	4.3
625.3	NVII	4p–1s	2.9	2.9	3.7	4.3	4.6
640.4	NVII	5p–1s	11	5.2	3.7	2.7	2.2
650.2	NVII	6p–1s	0.00	0.21	0.13	0.09	0.08
653.5	OVIII	2p–1s	27	40	48	51	53
665.6	OVII	1s3p–1s^2	1.7	1.3	1.3	1.2	1.2
697.8	OVII	1s4p–1s^2	0.81	0.79	1.0	1.2	1.3
712.8	OVII	1s5p–1s^2	2.8	1.3	0.92	0.68	0.54
722.7	OVII	1s6p–1s^2	0.00	0.06	0.04	0.02	0.02
774.6	OVIII	3p–1s	2.6	4.7	5.6	5.3	5.0
817.0	OVIII	4p–1s	1.0	1.6	2.0	2.2	2.3
836.5	OVIII	5p–1s	2.4	4.0	4.6	4.1	3.7
849.1	OVIII	6p–1s	1.6	1.6	1.5	1.1	0.67

9 Helium Charge Exchange in Cometary Atmospheres

In this chapter we will focus on the interaction of helium ions from the solar wind with molecules that are abundant in cometary and planetary atmospheres. In Chapter 5 state selective cross sections for collisions between helium ions and H_2O, CO_2, CO and CH_4 were presented. From the laboratory results we deduce data sets for EUV emission in astrophysical environments. These cross sections are the ingredients in our model calculations of cometary helium emission. Using these spectra, we show in Section 9.3 how EUV emission can be analyzed in terms of solar wind and comet characteristics and apply this to existing observations of the comets C/1996 B2 (Hyakutake) and C/1995 O1 (Hale-Bopp).

9.1 Model Results

The sensitivity of charge exchange processes to properties of both the solar wind and the comet leads to many observable effects. The observation of helium emission from comets can therefore be used to probe the characteristics of the comet – solar wind interaction.

In this chapter, we shall use comet Halley as our standard case and adopt the comet and solar wind characteristics that were observed during the *Giotto* encounter, i.e. a gas production of 7×10^{29} molecules s^{-1} of which 10% CO molecules, located at 1 AU from the Sun and encountering a solar wind with $v(\infty)$ = 370 km s^{-1}, $n_p(\infty)$ = 10 cm^{-3} and a solar wind alpha abundace of 2% (Fuselier et al., 1991).

9.1.1 Intensities

Changing the cometary and/or solar wind parameters affects the absolute and relative emission line intensities. This is illustrated in Fig. 9.1, where the total luminosity of the HeII 30.4 nm is plotted against the total luminosity of the HeI 58.4 nm line for a Halley-like interaction. The luminosity of the HeII 30.4 nm line increases by four orders of magnitude as the velocity increases from 100 to 1000 km s^{-1}, whereas the luminosity of the HeI

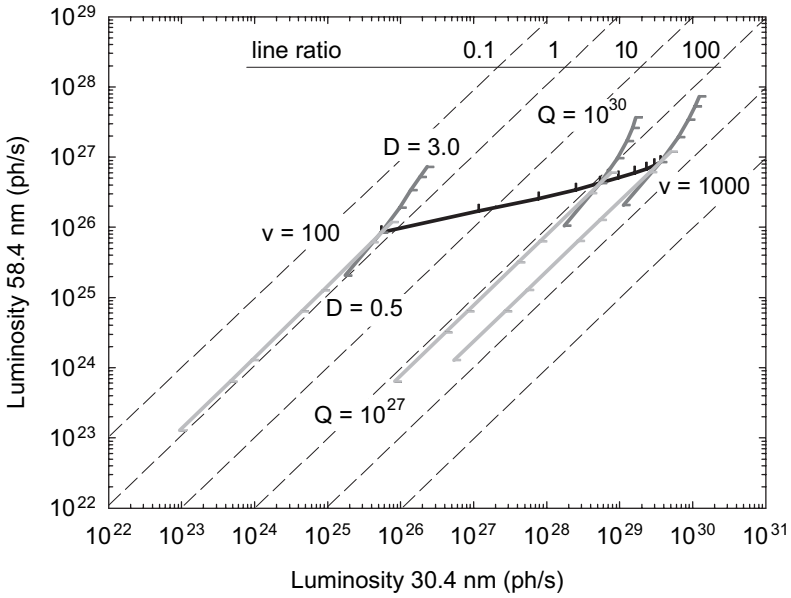

Figure 9.1: *HeI and HeII EUV luminosities of comet Halley. The solid black line indicates the dependence of the helium line emission on the initial velocity of the solar wind (given in units of km s^{-1}). For fixed velocities, the grey lines indicate the influences of changes in gas production (molecules s^{-1}) and heliocentric distance (AU).*

58.4 nm line merely follows the increase of solar wind flux. The ratio between the two helium lines can be seen to be very sensitive to the initial velocity of the solar wind. This behavior is a direct consequence of the strong and weak velocity dependence of the emission cross sections of the 30.4 and 58.4 nm emission, respectively, cf. Figs. 5.6 and 5.7.

The absolute luminosities of the two helium lines depend on the solar wind flux and on cometary characteristics, such as the mass loss rate and the heliocentric distance. Because the largest part of the cometary atmosphere is collisionally thin to charge exchange, the luminosity follows the increase in available neutral donor species. An increase in the mass loss rate or heliocentric distance therefore affects both emission lines in a similar fashion, so that whereas their absolute brightnesses change, the ratio between them is preserved. The ratio between HeII 30.4 nm and HeI 58.4 nm emission can therefore be used to probe the velocity of the wind, whereas absolute line intensities measure a combination of solar wind helium fluxes and comet mass loss rates.

9.1.2 Relative Contributions of Species

In Chapter 5, we presented state selective electron capture cross sections for different species that are abundant in cometary atmospheres. It was demonstrated that below collision velocities of approximately 1000 km s^{-1}, charge exchange cross sections differ per electron donor species.

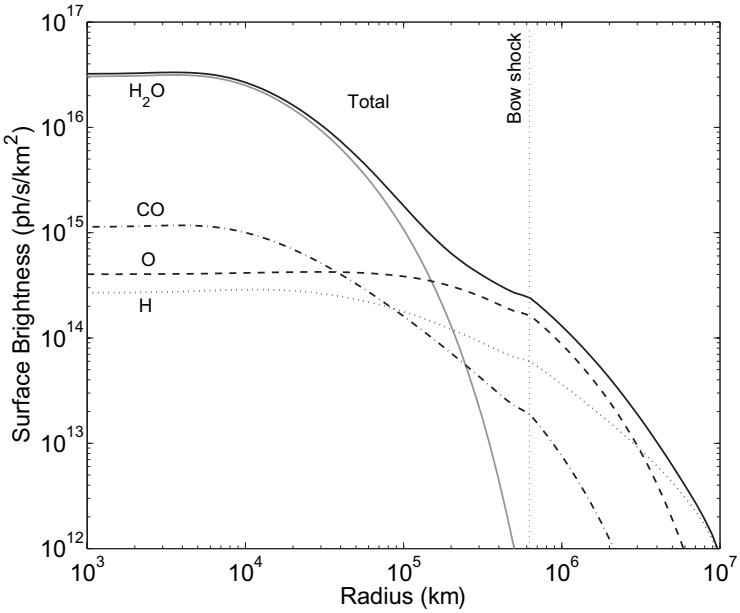

Figure 9.2: *The contribution of neutral cometary species to the surface brightness of the HeII 30.4 nm line within increasing annuli around the nucleus of comet Halley. Black solid line, total; grey solid line, H_2O; dotted line, H: dashed line, O; dash-dotted line, CO.*

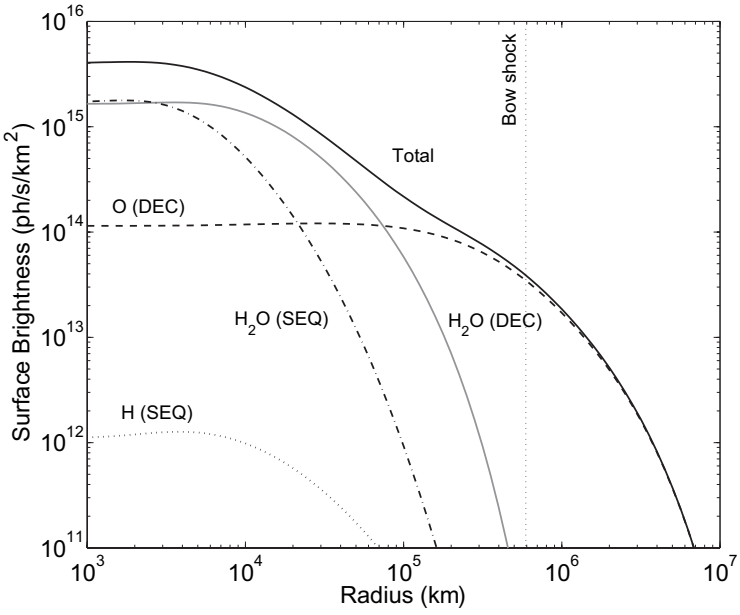

Figure 9.3: *The contribution of neutral cometary species to the surface brightness of the HeI 58.4 nm line within increasing annuli around the nucleus of comet Halley. Black solid line, total; grey solid line, water B2C; dashed-dotted line, water SEQ; dashed line, O B2C; dotted line, atomic H SEQ.*

Figs. 9.2 and 9.3 show which collisions underly the helium line emission of a Halley-like comet-wind interaction. Within ~ 10^5 km from the nucleus, the emission of both lines is dominated by helium colliding on water. Further outward however, the water dissociation products can be seen to take over this role; the HeII 30.4 nm line is then caused by collisions with atomic O and H while the HeI 58.4 nm is due to collisions with atomic O.

Comparing the surface brightness plots with the Haser-model (Fig 8.1), it can be seen that the area where the surface brightness of the 30.4 nm emission is dominated by emission following collisions with water is roughly two times bigger than the region where water molecules are the most abundant neutral species. This difference occurs because emission cross sections for water are much larger than the emission cross sections for O and H (cf. Fig. 5.6). In the case of the HeI 58.4 nm emission, the region where the surface brightness is water-dominated coincides with the region where water is most abundant, as we assumed double electron emission cross sections for collisions with atomic oxygen to be as large as those for collisions with water.

In Fig 9.2, a small kink shows up around 6×10^5 km. This kink is located at the bow shock, which we assumed to be an abrupt transition, and reflects the change of effective collision velocity. Since emission cross sections for double electron capture are roughly constant over the relevant velocity range, the bow shock causes no observable discontinuity in the HeI 58.4 nm emission.

Sequential electron capture plays only a minor role in the deeper lying collisionally thick regions of the comet. The important role of atomic oxygen with regard to the HeI is very interesting, as collisions between He^{2+} and atomic oxygen have barely been studied.

The rate of photo-destruction of cometary neutrals increases with the inverse square of the heliocentric distance r_h. According to the Haser-model, the distance to the nucleus where the number density of water equals the number density of H then depends only on the heliocentric distance with $r_h^{3/2}$. The closer a comet gets to the Sun, the more important emission following charge exchange with water daughter species will become, at the expense of the role of water molecules.

9.1.3 Spatial Effects

The extent of charge exchange emission and the location of its maximum surface brightness depends on the neutral gas distribution in the coma and on the cross sections of the underlying charge exchange processes. Depending on the velocities of the solar wind within the cometary atmosphere, each charge exchange reaction has a specific length scale.

At low densities, charge exchange affects the charge state distribution only marginally. In such collisionally thin environments, EUV and X-ray charge exchange aurorae map the distribution of neutral gas in the coma (cf. the observations of comet 2P/2003 (Encke) by Lisse et al., 2005). When the atmosphere becomes denser and hence collisionally thick to charge exchange, the aurora will take the form of a characteristic 'bowl' (Wegmann et al., 2004), which in projection takes the typical crescent shape observed in the X-ray observations of comet C/1996 B2 (Hyakutake) and C/1999 S4 (Linear) (Lisse et al., 1996, 2001). It is of note here, that total charge exchange cross sections of helium are more than an order of magnitude smaller than total charge exchange cross sections of highly charged solar wind

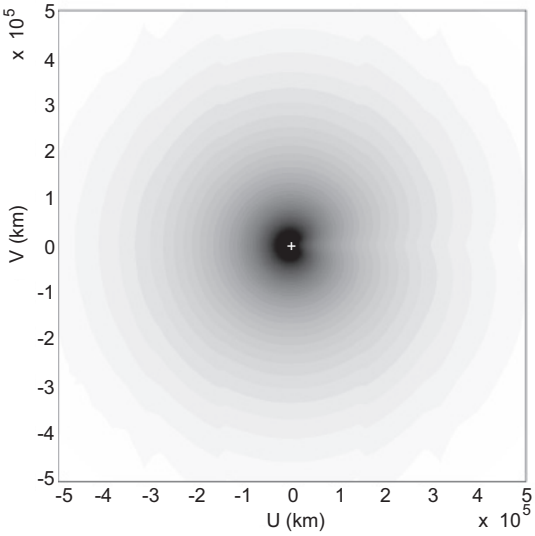

Figure 9.4: *Stretched gray scale image of the morphology of the HeII 30.4 nm emission for a Halley-like comet-wind interaction in arbitrary units, seen with a phase angle of 90°. The comet's nucleus is indicated by a cross hair.. The Sun is to the left.*

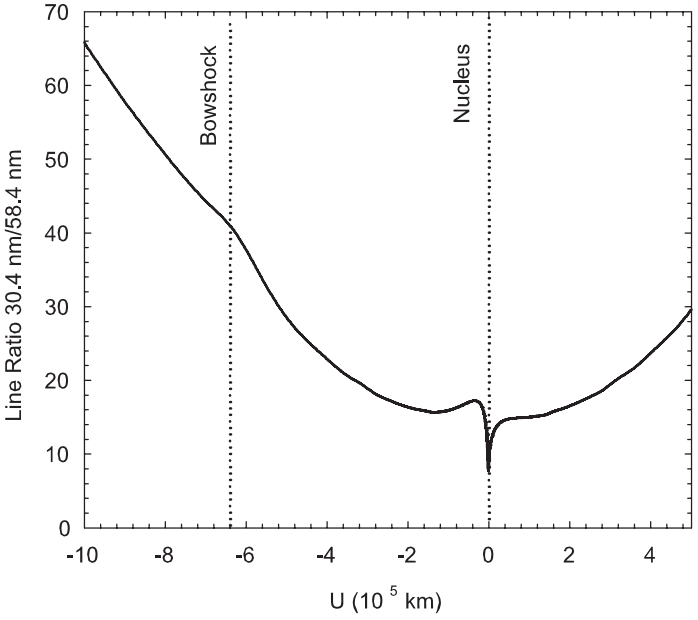

Figure 9.5: *Ratio of the intensities of the HeII 30.4 nm and HeI 58.4 nm emission lines along the comet-Sun axis. The Sun is to the left.*

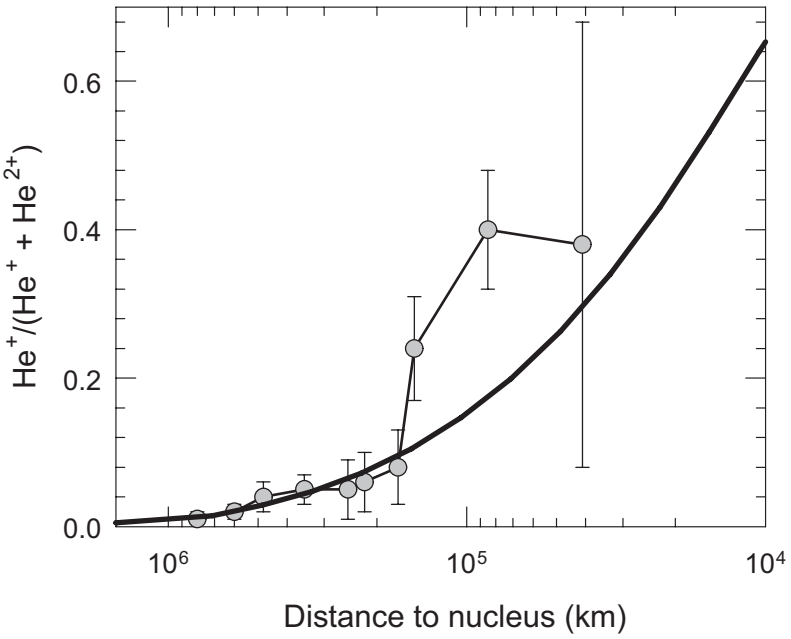

Figure 9.6: *Helium charge state distribution in comet Halley. The solid line represents the predicted distribution. In situ measurements performed by the Giotto probe are indicated by circles.*

oxygen, carbon and nitrogen ions. Different from X-ray observations, EUV emission will therefore display a weaker crescent shape, which is surrounded by a faint symmetric halo from the outer, collisionally thin regions of the coma (see Fig. 9.4).

The spatial behavior of the line emission ratio is illustrated in Fig. 9.5, where the ratio between the HeII 30.4 nm and HeI 58.4 nm line on the comet-Sun axis projected in the observer's plane is shown. Beyond 2×10^5 km of the nucleus, the presence of atomic hydrogen increases the HeII line, thereby increasing the ratio between the HeII and HeI line. The coma is collisionally thick to He^{2+} just before the nucleus, where the ratio increases slightly. The ratio then reaches a minimum, as the He^{2+} state is depleted, and this depletion is also responsible for the shadow behind the nucleus that can be seen in both Fig.s 9.4 and 9.5.

9.2 In Situ Measurements by the *Giotto* Mission

Using experimental total charge exchange cross sections, the charge state distribution was simulated for comet Halley. In situ measurements of both the solar wind velocity (Goldstein et al., 1987) and the helium charge state distribution (Fuselier et al., 1991) performed with the IMS/HERS instruments on board *Giotto* allow for a test of our model. A solar wind velocity of 300 km/s and cometary characteristics as summarized in Table 1 were used. As can be seen from Fig. 9.6, the predicted distribution is in good agreement with the *Giotto*

measurements, up to the magnetic pile-up boundary (1.5×10^5 km, Goldstein et al. (1987)) where complex magneto-hydrodynamics start to govern the interactions.

9.3 Analysis of Existing EUV Observations

Several comets have been observed in the Extreme Ultraviolet (Mumma et al., 1997), and in two cases helium emission has been detected. In comet Hale-Bopp, the 58.4 nm line was observed, but the 30.4 nm was not detected above the background; in comet C/1996 B2 (Hyakutake), it was exactly the other way around as the 30.4 nm line was detected but the 58.4 nm line was not detected above the background. Here, we will apply our model to these comets to demonstrate how cometary EUV emission can be analyzed in terms of charge exchange processes.

9.3.1 C/1996 B2 (Hyakutake)

Comet C/1996 B2 (Hyakutake) was observed with the Extreme Ultraviolet Explorer (EUVE) from March 21 – 25, 1996 (Krasnopolsky et al., 1997). The observing conditions of Hyakutake are summarized in table 9.1. During its observation, the comet was very close to Earth (approximately 0.1 AU) and therefore well studied by different techniques, which help us to reduce the number of free parameters in the model.

A compilation of hourly averages of different solar wind parameters obtained by the WIND and IMP8 spacecraft are available on the internet from the National Space Science Data Center OmniWeb[1]. Following the time shift procedure described by Neugebauer et al. (2000) and using the cometary coordinates summarized in Table 9.1, we find that the wind that interacted with C/1996 B2 (Hyakutake) was monitored on board the spacecrafts between March 21 4:00 UT and March 24 21:00 UT.

The OmniWeb data show a highly variable wind with velocities between 450 and 650 km s^{-1} during the observation and proton densities between 2 – 7 cm^{-3}. Although there

[1] http://nssdc.gsfc.nasa.gov/omniweb/ow.html

Table 9.1: *Observing conditions of C/1996 B2 (Hyakutake). References: 1. Biver et al. (1999); 2. JPL Horizons website*

Parameter	3/21/96	3/25/96	ref.
Q (mol/s)	2×10^{29}		1
Q_{CO} (mol/s)	4×10^{28}		1
R (AU)	1.13	1.05	2
Δ (AU)	0.17	0.10	2
Phase Angle (degrees)	37	58	2
Heliogr. Lat. (degrees)	-3.7	-1.9	2
Heliogr. Long. (degrees)	309	308	2

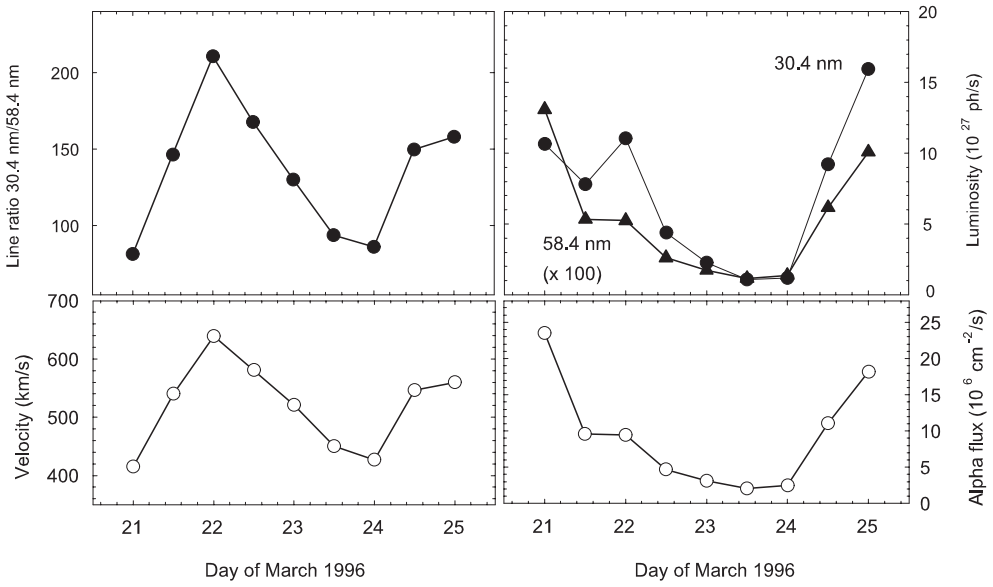

Figure 9.7: *Temporal variability of helium charge exchange emission of C/1996 B2 (Hyakutake) during the* EUVE *observations.* ***Upper left:*** *Calculated ratio of the* HeII *30.4 nm/*HeI *58.4 nm line emission.* ***Upper right:*** *Calculated luminosities of* HeI *58.4 nm and* HeII *30.4 nm.* ***Lower left:*** *Solar wind velocity from OmniWeb as received on C/1996 B2 (Hyakutake)* ***Lower right:*** *Solar wind helium flux from OmniWeb as received on C/1996 B2 (Hyakutake).*

was a 3 – 7° latitudinal separation between comet and spacecraft (Neugebauer et al., 2000) and latitudinal gradients are present in the solar wind, we will use the OmniWeb solar wind data as input parameters to model the EUV emission of comet C/1996 B2 (Hyakutake). The OmniWeb data shows a high variability in solar wind density, velocity and alpha content. This is supported by optical observations of plasma tail disconnection events, which also demonstrate that, during the EUVE observation, comet C/1996 B2 (Hyakutake) interacted with a highly variable (thus equatorial) solar wind (Snow et al., 2004).

Fig. 9.7 shows the predicted total luminosities of the two helium lines during the EUVE observations. Variations in the solar wind helium flux cause the total luminosities of the two helium lines to vary over more than an order of magnitude while the ratio varies with a factor of 2. The 58.4 nm line can be seen to track the alpha particle flux, whereas the behavior of the 30.4 nm line is a convolution of the variation due to the velocity and the flux. The behavior of the line emission ratio therefore directly probes the velocity variations.

The HeII 30.4 nm line was observed to have a photon production rate of 7.3×10^{24} photons/s. The HeI 58.4 nm line was not detected above the background level of 10^{24} photons/s. The two helium lines were observed with two different EUVE detectors; the HeII 30.4 nm line is observed with the medium wavelength spectrometer (MW) while for the HeI 58.4 nm line the long wavelength (LW) spectrometer is required. Due to filter configurations, different apertures were used. The MW and LW detector had apertures of $36.6' \times 9.2'$

Table 9.2: *Summary of C/1996 B2 (Hyakutake) model results and data reduction*

	$L_{30.4}$ (ph/s)	$L_{58.4}$ (ph/s)	ratio
Observation	6.6×10^{24}	$<8\times10^{23}$	$\gtrsim 8$
Model emission in MW aperture	1.48×10^{26}	5.65×10^{24}	26
Model emission in LW aperture	1.35×10^{26}	5.19×10^{24}	26
Model emission after background subtraction (MW aperture)	7.2×10^{24}	(1.6×10^{23})	(45)
Model emission after background subtraction (LW aperture)	(3.9×10^{25})	1.7×10^{24}	(22)
Model results	7.2×10^{24}	1.7×10^{24}	4

and $32.9' \times 9.2'$, respectively, and were both centered on the comet's nucleus. Krasnopolsky et al. (1997) used factors of 1.1 and 1.2 to correct for the different apertures of the MW and LW detector, respectively, so that from the reported values above we deduce photon production rates of 6.6×10^{24} photons/s for the HeII 30.4 nm line and an upper limit of 8.3×10^{23} photons/s for the HeI 58.4 line in the apertures.

As the comet filled the entire field of view, the observers subtracted a tail ward part of the signal from that of a sunward part, based on the assumptions that C/1996 B2 (Hyakutake) was collisionally thick to charge exchange and that its charge exchange emission was homogenous over the observed part of the comet. From our results in section 9.1.3, we expect that for the case of comet Hyakutake, these assumptions are not fully justified. To illustrate this, we summarize the model results, integrated over the time of the observations to take the variability of the wind into account and follow the data reduction procedure of the observers in Table 9.2.

From this table, it can be seen that the different MW and LW aperture sizes do not affect the line ratio and that the emission can be scaled by a factor that accounts for the different aperture sizes. Following the background subtraction procedure of the observers, we calculate luminosities of 7.2×10^{24} and 1.7×10^{24} photons/s for the HeII 30.4 nm and HeI 58.4 nm lines, respectively. We conclude that as much as 90% of the cometary HeII emission line and 65% of the HeI emission was subtracted as 'background'.

Given the uncertainties introduced by the background subtraction procedure of the observation, the uncertainties in the initial solar wind conditions, and the high variability of the solar wind during the observations, the model reproduces the observations very well.

The case of comet C/1996 B2 (Hyakutake) shows both the observational difficulties and potential diagnostic richness of cometary charge exchange aurorae. The temporal behavior of relative and absolute line emission can be used to remotely study solar wind characteristics whereas their spatial distribution provides access to the interaction between the comet and the wind.

Table 9.3: *Observing conditions of C/1995 O1 (Hale-Bopp). References: 1. Biver et al. (1999); 2. JPL Horizons website*

Parameter	9/14/96	9/20/96	ref.
Q (molec./s)	6×10^{29}		1
Q_{CO} (molec./s)	2×10^{29}		1
Q_{CO_2} (molec./s)	6×10^{28}		1
R (AU)	3.09	3.03	2
Δ (AU)	2.90	2.92	2
Phase Angle (degrees) .	19	19	2
Heliogr. Lat. (degrees) .	19	20	2
Heliogr. Long. (degrees)	44	44	2

9.3.2 C/1995 O1 (Hale-Bopp)

Comet C/1995 O1 (Hale-Bopp) was observed with the EUVE observatory from September 14-19, 1996 by Krasnopolsky et al. (1997). The observing conditions of Hale-Bopp are summarized in Table 9.3.

An estimate of the solar wind conditions at Comet C/1995 O1 (Hale-Bopp) during the EUVE observations is obtained by mapping measurements made in-situ by the *Ulysses* spacecraft to the comet's position. The *Ulysses* data over the period of interest are summarized in Fig. 9.8. At the time, *Ulysses* was at a solar latitude of 26 degrees North, while C/1995 O1 (Hale-Bopp) was at 19.9 degrees North. The spacecraft was separated from C/1995 O1 (Hale-Bopp) by around 130° in longitude; Hale-Bopp was at a heliocentric distance of 3.05 AU, while *Ulysses* was at 4.35 AU. Solar wind conditions might have varied between the spacecraft and the comet, but as the structure of the solar wind around this time was fairly stable, and the parameters observed by *Ulysses* were fairly constant from one rotation to the next, it seems justifiable to use the solar wind conditions observed by *Ulysses* and summarized in Table 9.3 as initial conditions in our model.

From the *Ulysses* data, C/1995 O1 (Hale-Bopp) would have interacted with a quiet, fast solar wind. There is some variability in the alpha-particle measurements, that differs from that seen in the protons. As is illustrated in Fig. 9.8, we predict that during the observations, the ratio between the HeII and HeI emission was constant, whereas the absolute intensities closely followed the solar wind helium flux and varied less than a factor of 3.

Krasnopolsky et al. (1997) observed a photon production rate of 1.2×10^{26} photons/s for the HeI 58.4 nm emission line within a projected slit of $5.4 \times 10^5 \times 3.6 \times 10^5$ km^2. Within this slit, the HeII was not detected above a 2σ upper limit of 7×10^{25} photons/s. Neither line was detected in the subtracted background spectrum, to a level of $\lesssim 3\%$ of the background continuum emission. Our model predicts that within this slit, the helium lines drop to less than 15% of the average surface brightness of the coma, and would 'disappear' into the background.

Averaging the results shown in Fig. 9.8 over the time of the observations, we find total photon production rates of 7.6×10^{26} and 2.9×10^{25} photons/s for the HeII 30.4 nm and

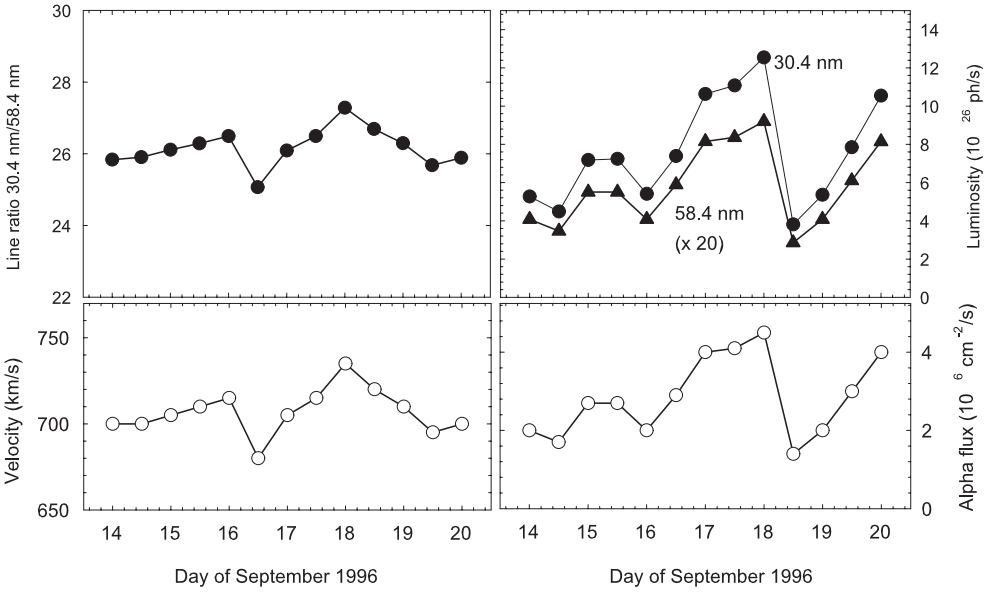

Figure 9.8: *Temporal variability of helium charge exchange emission of C/1995 O1 (Hale-Bopp) during the EUVE observations.* ***Upper left:*** *Calculated ratio between the HeII 30.4 nm and HeI 58.4 nm line emission.* ***Upper right:*** *Calculated luminosities of HeI 58.4 nm and HeII 30.4 nm.* ***Lower left:*** *Solar wind velocity from Ulysses as received on C/1995 O1 (Hale-Bopp).* ***Lower right:*** *Solar wind helium flux from Ulysses as received on C/1995 O1 (Hale-Bopp).*

the HeI 58.4 nm lines, respectively. Our model thus overestimates the HeII emission by a factor of 10 and underestimates the HeI emission within a factor of 4. We know of no other processes that can efficiently contribute to the HeI emission (Bodewits et al., 2004). Following Fig. 9.1, this suggests that comet C/1995 O1 (Hale-Bopp) interacted with a higher alpha particles flux, via either the total solar wind flux or the alpha particle abundance in the solar wind (hence increasing the luminosities of both helium emission lines) and also much slower (hence decreasing the HeII 30.4 nm emission but preserving the HeI 58.4 nm emission).

There are two different possible scenarios to fit the model to the observation, but we cannot distinguish between them as only total photon production rates are available.

Table 9.4: *Summary of C/1995 O1 (Hale-Bopp) observational and model results.*

	$L_{30.4}$ (ph/s)	$L_{58.4}$ (ph/s)	ratio
Observation	$< 7 \times 10^{25}$	1.2×10^{26}	$\gtrsim$0.6
Model results	7.6×10^{26}	2.9×10^{25}	26

First, the comet could have interacted with a slower, denser wind. According to our model, this would require an initial wind velocity below 200 km s^{-1} and an unrealistically high helium flux of 5×10^7 cm^{-2}/s, 17 times more than the flux observed by Ulysses.

It is possible that, although mapped *Ulysses* data suggest that Hale-Bopp was in fast, polar coronal hole solar wind at the time of observation, the lower heliolatitude of the comet compared to the spacecraft meant that it may actually have been south of the northern boundary of the streamer belt. Such a situation would yield a lower solar wind velocity, and higher solar wind particle number density at Hale-Bopp, with both of these parameters being more variable than in the fast, coronal hole flow. *Ulysses* and ground-based observations suggest that the heliospheric current sheet did extend to as high as 30 degrees north heliolatitude at the time (Forsyth et al., 1997). Ultimately, the solar wind conditions at Hale-Bopp at the time will not be determined absolutely, but even if the comet was within the streamer belt, it is unlikely that the velocity would be as low as 200 km s^{-1}, as required by our model.

Alternatively, the difference between modeled and observed HeII photo production rates might be explained in terms of cooling and slow down of the solar wind within the coma. At 3 AU from the Sun, C/1995 O1 (Hale-Bopp) was already an exceptionally large comet with a huge ionopause distance. According to Eq. 8.4, the bow shock must have been over 10^7 km from the nucleus; in contrast, for comet C/1996 B2 (Hyakutake), the bow shock was located at only a few 10^5 km in front of the nucleus. Our model can explain the observation in this scenario if the solar wind, with an initial velocity of 700 km s^{-1}, would have been cooled and slowed down to a mean collision velocity of $\lesssim$ 175 km s^{-1} in the interaction zone. To explain the observed luminosities, an alpha flux of 1.5×10^7 $cm^{-2}s^{-1}$ is needed, which is 5 times higher than the wind sampled by Ulysses. It would be most interesting to test these hypotheses with magnetohydrodynamic comet-wind models.

9.4 Summary and Conclusions

Within the limitations of available EUV observations of comets, we have illustrated the manifold consequences of the charge exchange interaction process. Clear spectral, temporal and morphological effects should be detectable for different comet – solar wind conditions. The main findings of this work are the following:

1. Emission cross sections are very sensitive to velocity effects. Every charge exchange reaction has its own particular behavior with respect to the velocity, so that line emission ratios - in our case the ratio between the HeII 30.4 nm and the HeI 58.4 nm line - can be used for velocimetry. Absolute intensities can be used to determine local heavy ion fluxes.

2. Different electron capture cross sections imply different emission length scales. Spatial gradients in charge exchange line emission ratios hence contain a wealth of information on the interaction between comet and solar wind. This also implies, that it will be very difficult to interpret spectra that are produced by integration over the full projected image of the comet as in the cases of the two comets discussed.

3. Water and its dissociation products O and H are the most important collision partners for charge exchange reactions in cometary atmospheres. Our model predicts that atomic oxygen is the most important multi-electron donor in the outer regions of the comet, but experimental data on charge exchange reactions is lacking.

4. Emission following double electron capture is the most important source of cometary EUV emission next to single electron capture. Sequential capture contributes only marginally to the HeI 58.4 nm emission. Interestingly, multiple electron capture has not been included in simulations of cometary X-ray spectra (cf. Ali et al. (2005)).

We have applied our model to the observation of helium emission in the comets C/1996 B2 (Hyakutake) and C/1995 O1 (Hale-Bopp). For Hyakutake, the comparison between model and observation is severely hampered by the large background correction. Nevertheless, our model seems to reproduce the observations well. The model results illustrate that the time variability of the different lines might provide a powerful tool as interaction diagnostics.

The case of C/1995 O1 (Hale-Bopp) illustrates well the dependence of the helium line emission to the collision velocity. For Hale-Bopp, our model requires low velocities in the interaction zone. We interpret this as the effect of severe post bow shock cooling in this extraordinary large comet.

10 Spectral Analysis of the Chandra Comet Survey

Cometary spectra reflect the physical characteristics of the solar wind; e.g. spectra resulting from either fast, cold (polar) wind and slow, warm equatorial solar wind should be clearly different (Schwadron and Cravens, 2000; Kharchenko and Dalgarno, 2001; Bodewits et al., 2004). Several attempts were made to extract ionic abundances from the X-ray spectra.

The first generation spectral models have all made strong assumptions when modeling the X-ray spectra (Haberli et al., 1997; Wegmann et al., 1998; Kharchenko and Dalgarno, 2000; Schwadron and Cravens, 2000; Lisse et al., 2001; Kharchenko and Dalgarno, 2001; Krasnopolsky et al., 2002; Beiersdorfer et al., 2003; Wegmann et al., 2004; Bodewits et al., 2004; Krasnopolsky, 2004; Lisse et al., 2005). Here, we present a more elaborate and sophisticated procedure to analyze cometary X-ray spectra based on atomic physics input, which for the first time allows for a comparative study of all existing cometary X-ray spectra. In Chapter 8, our comet-wind interaction model was briefly introduced. In Section 10.1, it is demonstrated how cometary spectra are affected by the velocity and target dependencies of charge exchange reactions. In Section 10.2, the various existing observations performed with the *Chandra* X-ray Observatory, as well as the solar wind data available are introduced. Based upon our modeling, we construct an analytical method of which the details and results are presented in Section 10.3. In Section 10.4, we discuss our results in terms of comet and solar wind characteristics. Lastly, in Section 10.5 we summarize our findings. Details of the individual *Chandra* comet observations are given in Appendix A.

10.1 Model Results

10.1.1 Relative Contribution of Target Species

Fig. 10.1 shows the dominant collisions which underly the X-ray emission of comets. Shown is the total intensity projected on the sky, with increasing field of view. Within 10^4 km around the nucleus, water is the dominant collision partner. Farther outward ($\geq 2\times10^5$ km),

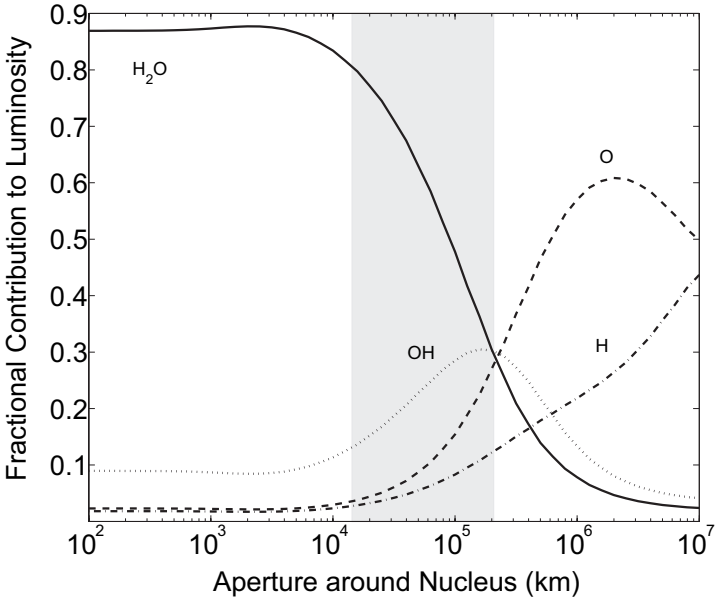

Figure 10.1: *Relative contribution of target species to the total intensity of OVII 570 eV emission complex with increasing field of view, for an active Q=10^{29} molecules s^{-1} comet, interacting with a 300 km s^{-1} solar wind at 1 AU from the Sun. The shaded area indicates the range of apertures used to obtain spectra discussed within this chapter.*

the atomic dissociation products of water take over, and atomic oxygen becomes the most important collision partner. When the field of view exceeds 10^7 km, atomic hydrogen becomes the sole collision partner. Note that collisions with water never account for 100% of the emission, even with very small apertures, due to the contribution of collisions with atomic hydrogen, OH and oxygen in the line of sight towards the nucleus.

The comets observed with *Chandra* are all observed with an aperture of approximately 7.5′ centered on the nucleus. This corresponds to a range of $1.6-22\times10^4$ km (as indicated in Fig. 10.1). Our model predicts that the emission from nearby comets will be dominated by CXE from water, but that for comets observed with a larger field of view, up to 60% of the emission can come from CXE interactions with the water dissociation products atomic oxygen and OH, and 10% from interactions with atomic hydrogen.

10.1.2 Solar Wind Velocity

To illustrate solar wind velocity induced variations in charge exchange spectra, we simulated charge exchange spectra following solar wind interactions between an equatorial wind and a $Q = 10^{29}$ molecules s^{-1} comet, and assumed the same solar wind composition in all cases. In Fig. 10.2, spectra resulting from collisional velocities of 300 km s^{-1} and 700 km s^{-1} are shown. In the spectrum from the faster wind, the CVI 367 eV and OVII

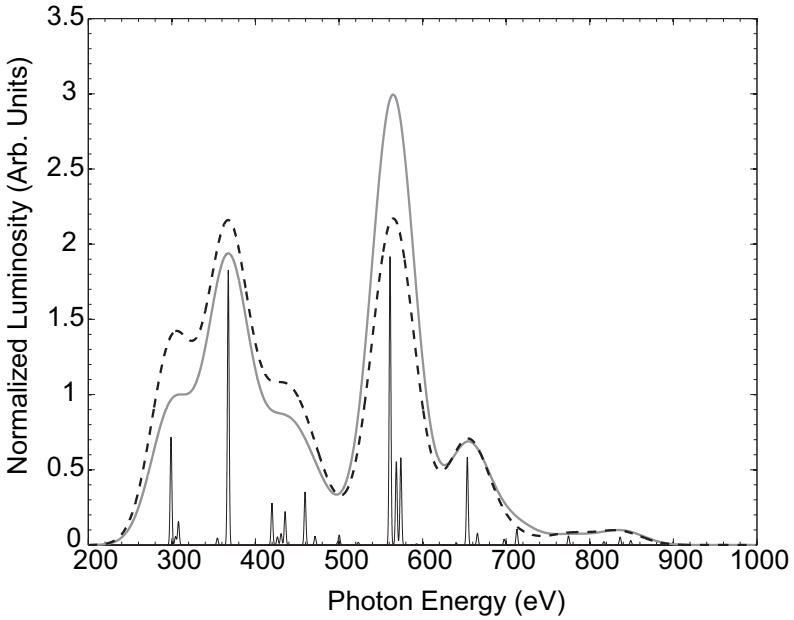

Figure 10.2: *Simulated X-ray spectra for a 10^{29} molecules s^{-1} comet interacting with an equatorial wind with velocities of 300 km s^{-1} (solid grey line) and 700 km s^{-1} (dashed black line). The spectra are convolved with Gaussians with a width of σ=50 eV to simulate the Chandra spectral resolution. To indicate the different lines, also the 700 km s^{-1} σ=1 eV spectrum is indicated (not to scale). A field of view of 10^5 km and 'typical' slow wind composition were used.*

570 eV emission features are roughly equally strong, whereas at 300 km s^{-1}, the oxygen feature is clearly stronger. Assuming the wind's composition remains the same, within the range of typical solar wind velocities (300 – 700 km s^{-1}), the cross section's dependence on solar wind velocity does not affect cometary X-ray spectra by more than a factor 1.5. In practice, the compositional differences between slow and fast wind will induce much stronger spectral changes.

10.1.3 Collisional Opacity

Many of the 20^+ comets that have been observed in X-ray display a typical crescent shape as the solar wind ion content is depleted via charge exchange. Comets with low outgassing rates around 10^{28} molecules s^{-1}, such as 2P/2002 (Encke) and 9P/2005 (Tempel 1), did not display this emission morphology (Lisse et al., 2005, 2007). Whether or not the crescent shape can be resolved depends mainly on properties of the comet (outgassing rate), but, to a minor extent, also on the solar wind (velocity dependence of cross sections). Other parameters (secondary, but important), are the spatial resolution of the instrument and the distance of the comet to the observer.

Initially, the charge state distribution depends on the solar wind state. For most sim-

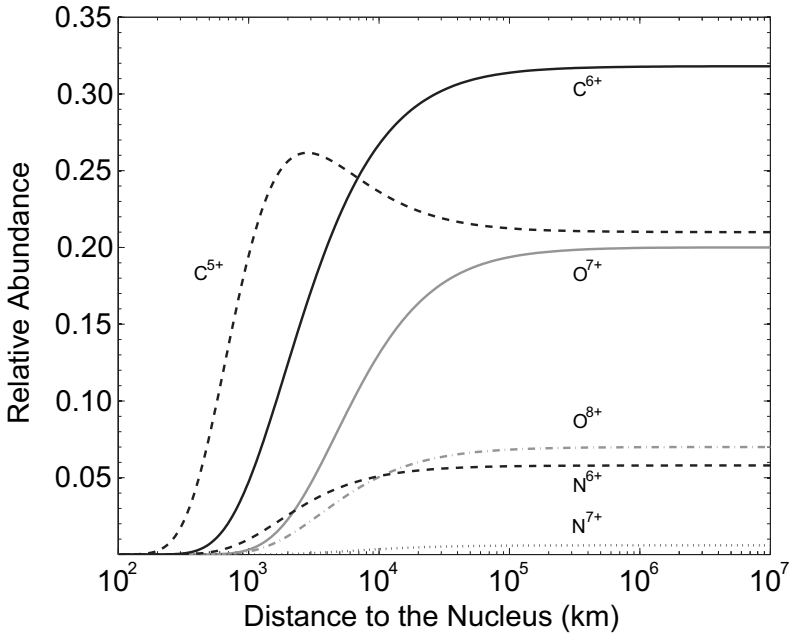

Figure 10.3: *Modelled charge state distribution along the comet-Sun line, assuming an equatorial 300 km s^{-1} wind interacting with a comet with outgassing rate Q=10^{29} molecules s^{-1} at 1 AU from the Sun. A composition typical for the slow, equatorial wind was assumed.*

ulation purposes, we will assume the 'average' ionic composition for the slow, equatorial solar wind as given by Schwadron and Cravens (2000). Using our compilation of charge changing cross sections, we can solve the differential equations that describe the charge state distribution in the coma in the 2D-geometry fixed by the comet-Sun axis. Fig. 10.3 shows the charge state distribution for a 300 km s^{-1} equatorial wind interacting with a comet with an outgassing rate Q of = 10^{29} molecules s^{-1} comet. From this charge state distribution, it can be seen that along the comet-Sun axis, the comet becomes collisionally thick between 3500 km (O^{8+}) to 2000 km (C^{6+}), depending on the cross section of the ions. A maximum in the C^{5+} abundance can be seen around 2,000 km, which is due to the relatively large initial C^{6+} population and the small cross section of C^{5+} charge exchange.

In a collisionally thin environment, the ratio between emission features is the product of the ion abundance ratios and the ratio between the relevant emission cross sections:

$$r_{thin} = \frac{n(A^{q+})}{n(B^{q+})} \cdot \frac{\sigma_{em}^{A^{q+}}(v)}{\sigma_{em}^{B^{q+}}(v)} \tag{10.1}$$

The flux ratio for a collisionally thick system depends on the charge states considered. In case of a bare ion A and a hydrogenic ion B, the ratio between the photon fluxes from A and B is given by the abundance ratio weighted by efficiency factors μ and η:

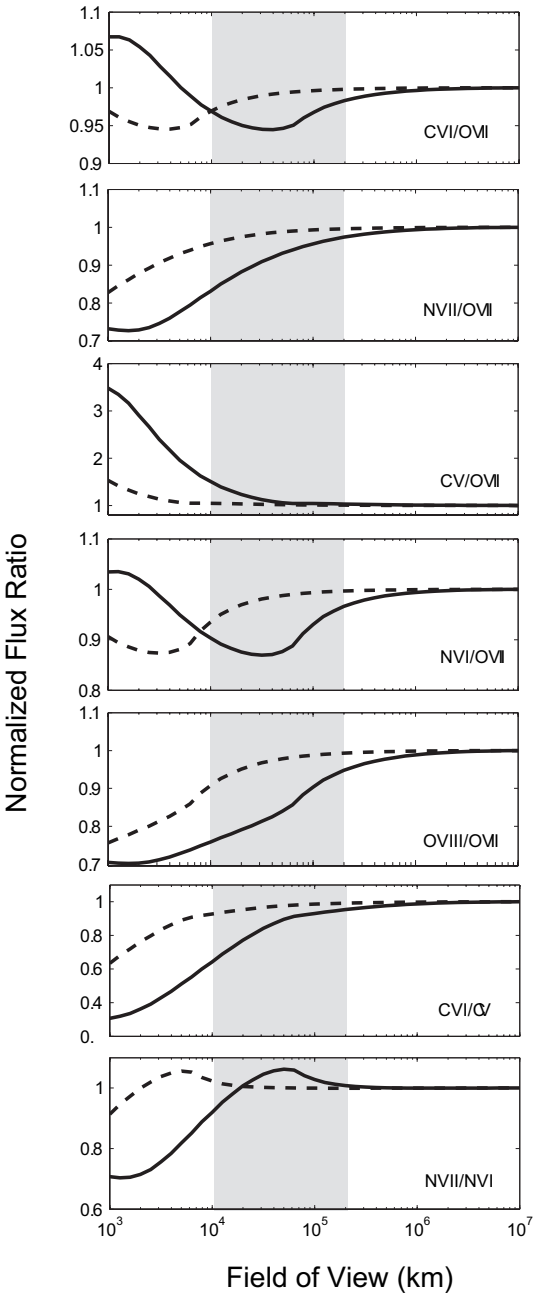

Figure 10.4: *Collisional opacity effects on flux ratios within the field of view. The outer bounds of the fields of view within this survey were between 10^4 – 10^5 km, as indicated by the shaded area. We considered a 500 km s^{-1} equatorial wind interacting with comets with different activities: Q=10^{28} molecules s^{-1} (dashed lines) and Q=10^{29} molecules s^{-1} (solid lines). All flux ratios are normalized to 1 at infinity.*

$$r_{thick} = \frac{n(A^{q+})}{n(B^{(r-1)+}) + \mu(B^{r+})n(B^{r+})} \cdot \frac{\eta(A^{q+})}{\eta(B^{(r-1)+})} \tag{10.2}$$

The efficiency factor μ is a measure of how much $B^{(r-1)+}$ is produced by charge exchange reactions by B^{q+}:

$$\mu = \frac{\sigma_{r,r-1}(v)}{\sigma_r(v)} \tag{10.3}$$

where σ_r is the total charge exchange cross section and $\sigma_{r,r-1}$ the one electron charge changing cross section. The efficiency factor η describes the emission yield per reaction and is given by the ratio between the relevant emission cross section σ_{em} and the total charge changing cross section σ_r:

$$\eta = \frac{\sigma_{em}(v)}{\sigma_r(v)} \tag{10.4}$$

To explore the effect of collisional opacity on spectra, we simulated two comets at 1 AU from the Sun, with gas production rates of 10^{28} and 10^{29} molecules s^{-1}, interacting with a solar wind with a velocity of 500 km s^{-1} and an averaged slow wind composition (Schwadron and Cravens, 2000). The results are summarized in Fig. 10.4 where different flux ratios are shown. The behavior of these ratios as a function of aperture is important because they can be used to derive relative ionic abundances. All ratios are normalized to 1 at infinite distance from the comet's nucleus. For low activity comets with $Q \leq 10^{28}$ molecules s^{-1}, the collisional opacity does not affect the comet's X-ray spectrum. Within typical field of views all line flux ratios are close to the collisionally thin value. For more active comets ($Q = 10^{29}$ molecules s^{-1}), collisional opacity can become important within the field of view. Observed flux ratios involving CV should be treated with care, see e.g. CV/OVII and CVI/CV, because the flux ratios within the field of view can be affected by almost 50% and 35%, respectively. The effect is the strongest in these cases because of the large relative abundance of C^{6+}, that contributes to the CVemission via sequential electron capture reactions in the collisionally thick zones. For NVII and OVIII, a small field of view of 10^4 km could affect the observed ionic ratios by some 20%.

To further illustrate these results, we show the resulting X-ray spectra in Fig. 10.5. There, we consider a $Q = 10^{29}$ molecules s^{-1} comet interacting with a 300 km s^{-1} wind and show the effect of slowly zooming from the collisionally thin to the collisionally thick zone around the nucleus. The field of view decreases from 10^5 to 10^3 km. At 10^5 km, the spectrum is not affected by collisionally thick emission, whereas the emission within an aperture of 1000 km is almost purely from the interactions within the collisionally thick zones of the comet, which can be most clearly seen by the strong enhancement of the CV emission around 300 eV.

The results of our model efforts demonstrate that cometary X-ray spectra reflect characteristics of the comet, the solar wind and the observational conditions. Firstly, charge exchange cross sections depend on the velocity of the solar wind, but its effects are the strongest at velocities below regular solar wind velocities. Secondly, collisional opacity can affect cometary X-ray spectra but mainly when an active comet ($Q = 10^{29}$ molecules s^{-1}) is observed with a small field of view ($\leq 5 \times 10^4$ km). The dominant factor however to explain differences in cometary CXE spectra is therefore the state and hence composition of the

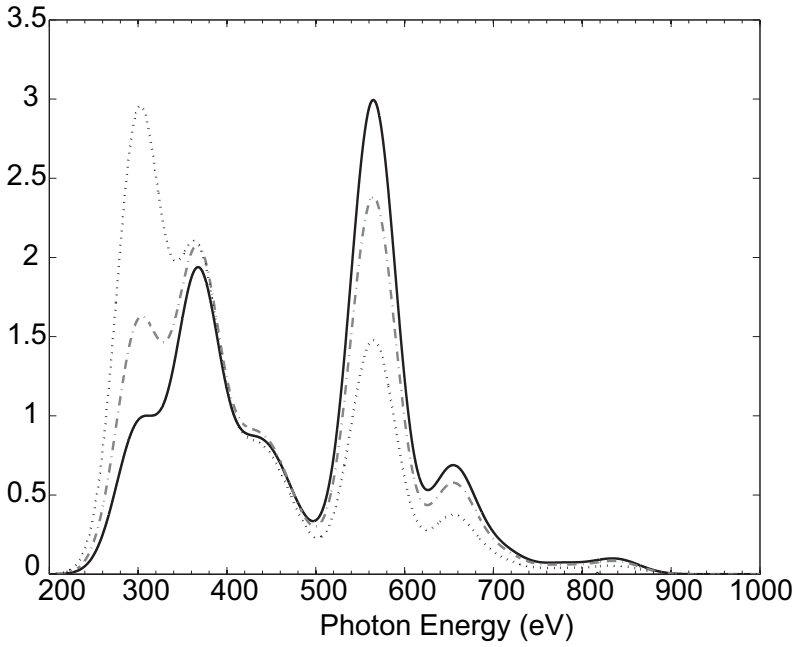

Figure 10.5: *Simulated X-ray spectra for a 10^{29} molecules s^{-1} comet interacting with an equatorial wind with a velocity of 300 km s^{-1} for fields of view decreasing from 10^5 km (solid line), 10^4 km (dashed line) and 10^3 km (dotted line).*

solar wind. This implies that the spectral analysis of cometary X-ray spectra can be used as a direct, remote quantitative and qualitative probe of the solar wind.

10.2 Observations

In this section, we will briefly introduce the different comet observations performed with *Chandra*. A summary of comet and solar wind parameters is given in Table 10.1. More observational details on the comet and a summary of the state of the solar wind at the location of the comet during the X-ray observations can be found in Appendix B.

10.2.1 Solar Wind Data

Our survey spans the whole period between solar maximum (mid 2000) and solar minimum (mid 2006), see Fig. 10.6. During solar minimum, the solar wind can be classified in polar- and equatorial streams, where the polar can be found at latitudes larger than 30° and the equatorial wind within 15° of the helioequator. Polar streams are fast (approximately 700 km s^{-1}) and show only small variations in time, in contrast to the irregular equatorial wind. Cold, fast wind is also ejected from coronal holes around the equator, and when these streams interact with the slower background wind corotating interaction regions (CIRs) are formed. As was illustrated by Schwadron and Cravens (2000), different wind types vary greatly in their compositions, with the cooler, fast wind consisting of on average lower charged ions than the hotter equatorial wind. This clear distinction disappears during solar maximum, when at all latitudes the equatorial type of wind dominates. In addition, coronal mass ejections are far more common around solar maximum.

There is a strong variability of heavy ion densities due to variations in the solar source regions and dynamic changes in the solar wind itself (Zurbuchen and Richardson, 2006). The variations mainly concern the charge state of the wind as elemental variations are only on the order of a factor of 2 (von Steiger et al. (2000), and references therein).

We obtained solar wind data from the online data archives of ACE (proton velocities and densities from the SWEPAM instrument, heavy ion fluxes from the SWICS and SWIMS instruments[1]) and SOHO (proton fluxes from the Proton Monitor Instrument[2]). Both ACE and SOHO are located near Earth, at its Lagrangian point L1. In order to map the solar wind from L1 to the position of the comets, we used the time shift procedure described by Neugebauer et al. (2000). The calculations are based on the comet ephemeris, the location of L1 and the measured wind speed. With this procedure, the time delay between an element of the corotating solar wind arriving at L1 and the comet can be predicted. A disadvantage of this procedure is that it cannot account for latitudinal structures in the wind or the magnetohydrodynamical behavior of the wind (i.e., the propagation of shocks and CMEs). These shortcomings imply that especially for comets that have large longitudinal, latitudinal and/or radial separations from Earth, the solar wind data is at best an estimate of the local wind conditions. The resulting proton velocities at the comets near the time of the *Chandra* observations are shown in Fig. 10.7.

Parallel to this helioradial and heliolongitudinal mapping, we compared our comet survey to a 3D MHD time-dependent solar wind model that was employed during most of Solar Cycle 23 (1997 - 2006) on a continuous basis when significant solar flares were observed. The model (reported by (Fry et al., 2003; McKenna-Lawlor et al., 2006) and

[1] http://www.srl.caltech.edu/ace/ASC/level2/index.html
[2] http://umtof.umd.edu/pm/crn/

Table 10.1: *Comet observation times and observing parameters. For comets McNaught-Hartley and Ikeya-Zhang, the parameters were averaged over the observation time span. Solar wind proton velocities and fluxes are measured in the ecliptic plane. Solar wind data for comets observed at large heliocentric latitudes are therefore highly uncertain and denoted within brackets. Comet labels refer to labels used in the figures in this paper.*

Parameter		C/1999 S4 (LINEAR)	C/1999 T1 (McNaught-Hartley)	C/2000 WM1 (LINEAR)	153P/2002 (Ikeya-Zhang)	2P/2003 (Encke)	C/2001 Q4 (NEAT)	9P/2005 (Tempel 1)	73P/2006 (SW3-B)
Comet Label		a.	b.	c.	d.	e.	f.	g.	h.
Observation Date		7/14/2000	1/8-15/2001	12/31/2001	4/15-16/2002	12/24/2003	5/12/2004	6/30/2005	5/23/2006
T_{exp}	(ksec)	9.4	16.9	35	24	54	10.51	52	20
r_h[a]	(AU)	0.80	1.26	0.75	0.81	0.89	0.96	1.51	0.97
Δ[a]	(AU)	0.53	1.37	0.68	0.45	0.28	0.38	0.88	0.10
Lon[a]	(Degrees)	312	185	70	206	51	211	245	247
ΔLon[b]	(Degrees)	20	73	-30	0.5	-11	-22	-34	5
Lat[a]	(Degrees)	24	15	-34	26	11	-3	0.8	0.5
Phase[a]	(Degrees)	98	62	87	102	103	86	41	114
S-O-T	(Degrees)	51	44	49	52	60	72	105	61
Q_{gas}	(10^{28} mol. s^{-1})	3[c]	6-20[d]	3-9[e]	20[f]	0.7[g]	13[h]	0.9[i]	2[j]
Wind		ICME	CIR/flare	ICME	ICME	Flare/PS[k]	Quiet	Quiet	CIR
v_p[l]	(km s^{-1})	(592)	353	(324)	(372)	583	352	402	449
Δt	(days)	1.09	6.63	-3.5	-0.73	-1.09	-1.80	-0.38	0.2
F_p[l,m]	(10^8 cm^{-2} s^{-1})	(2.9)	1.6	(1.4)	(3.8)	3.15	5.9	5.1	2.3
Radius FoV	(10^5 km)	0.86	2.24	1.66	0.73	0.46	0.62	1.44	0.16

[a] JPL-Horizons
[b] difference between heliocentric longitude of comet and earth Lon_c - Lon_e
[c] Bockelée-Morvan et al. (2001),Farnham et al. (2001)
[d] Mumma et al. (2001),Schleicher (2001),Weaver et al. (2002),Biver et al. (2006)
[e] Schleicher et al. (2002),Biver et al. (2006)
[f] dello Russo et al. (2004); Biver et al. (2006)
[g] Lisse et al. (2005)
[h] Friedel et al. (2005) and references therein
[i] Mumma et al. (2005),Schleicher et al. (2006)
[j] Schleicher, priv. communication
[k] PS - post shock flow
[l] ACE-SWEPAM and SOHO-CELIAS online data archives
[m] The proton flux was scaled by $1/r_h^2$ at the location of each comet to account for its density fall off due to radial expansion of the solar wind.

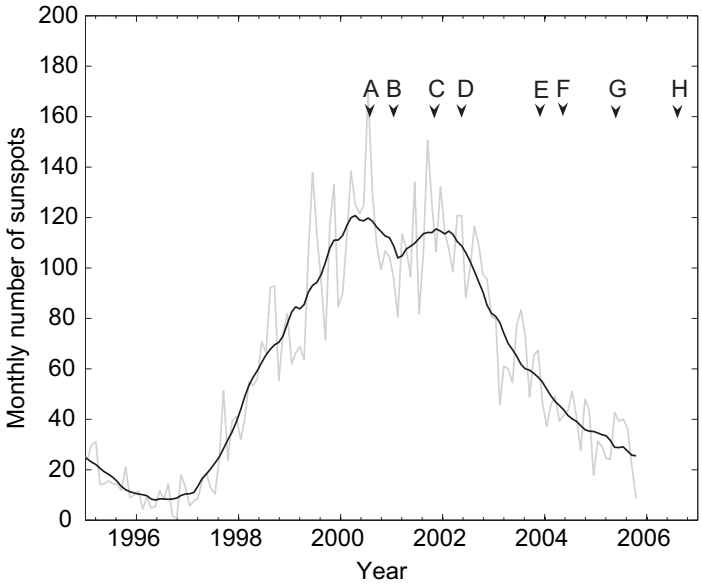

Figure 10.6: *Chandra comet observations during the descending phase of solar cycle # 23. Monthly sunspot numbers (grey line) and smoothed monthly sunspot number (black line) from the Solar Influences Data Analysis Center of the Department of Solar Physics, Royal Observatory of Belgium (http://sidc.oma.be/). Letters refer to the chronological order of observation.*

Z.K. Smith, private communication, for, respectively, the ascending, maximum, and descending phases) treats solar flare observations and maps the progress of interplanetary shocks and CMEs. The papers mentioned above provide an RMS error for "hits" of ±11 hours (Smith et al., 2000; McKenna-Lawlor et al., 2006). CIR fast forward shocks were also taken into account in order to differentiate between the co-rotating "quiet" and transient structures. It was important, in this differentiating analysis, to examine (as we have done here) the ecliptic plane plots of both of these structures as simulated by the deforming interplanetary magnetic field lines (see, for example, (Lisse et al., 2005, 2007) for several of the comets discussed here.) Therefore, the various comet locations (Table 10.1) were used to estimate the probability of their X-ray emission during the observations being influenced by either of these heliospheric situations.

10.2.2 X-ray Observations

After its launch in 1999, 8 comets have been observed with the *Chandra* X-ray Observatory and Advanced CCD Imaging Spectrometer (ACIS). Here, we have mainly considered observations made with the ACIS-S3 chip, which has the most sensitive low energy response and for which the majority of comets were centered. The *Chandra's* ACIS-S instrument provides moderate energy resolution ($\sigma \approx 50$ eV) in the 300 to 1500 eV energy range, the primary range for the relatively soft cometary emission. All comets in our sample were re-mapped

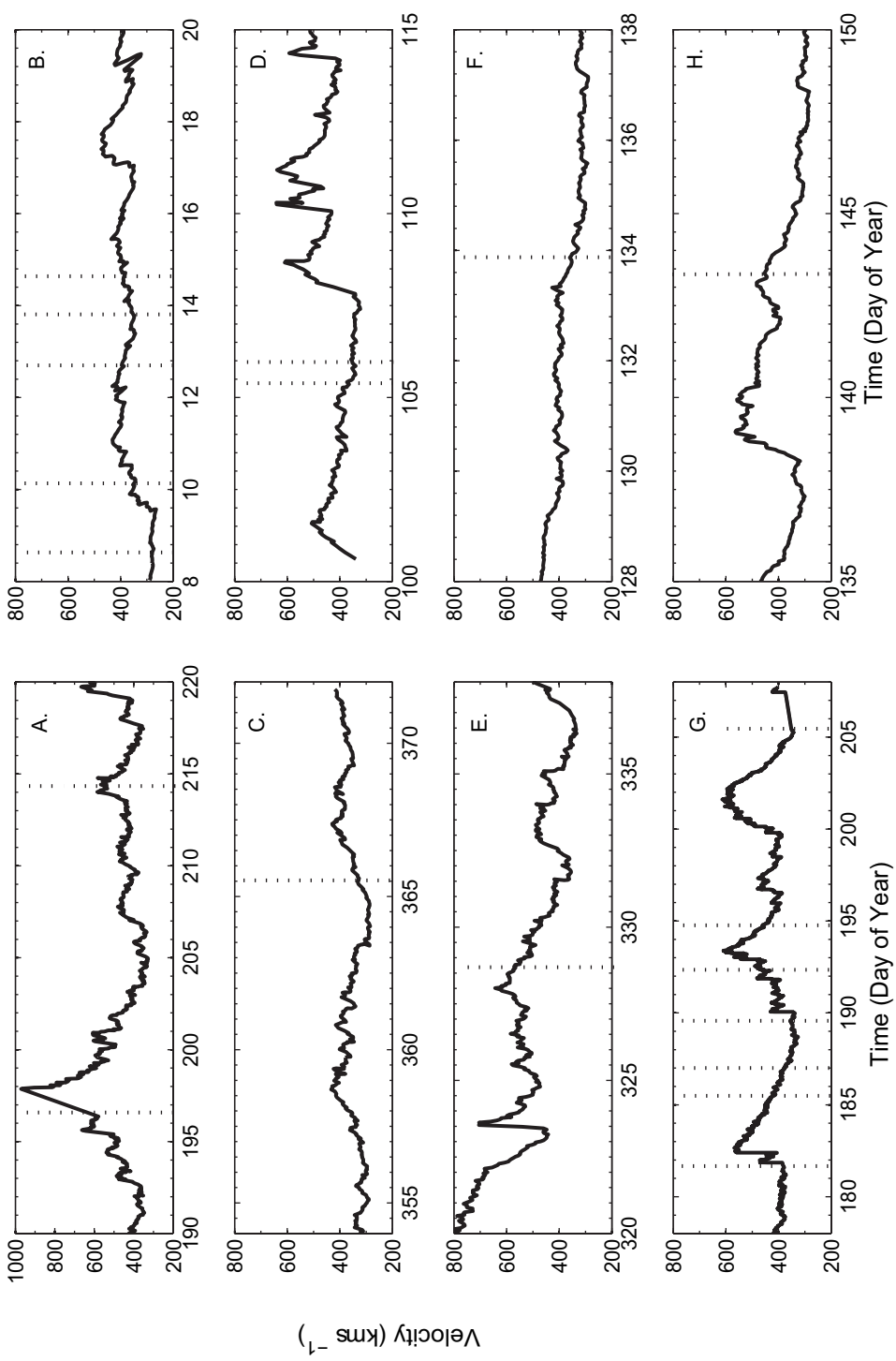

Figure 10.7: *Solar wind proton velocities estimated from ACE and SOHO data. For all comets, the time of the observations is indicated with a dotted line. Letters refer to the chronological order of observation.*

into comet-centered coordinates using the standard Chandra Interactive Analysis of Observations (CIAO v3.4) software 'sso_freeze' algorithm.

Comet source spectra were extracted from the S3 chip with a circular aperture with a diameter of 7.5′, centered on the cometary emission. The exception was comet C/2001 Q4, which filled the chip and a 50% larger aperture was used. ACIS' response matrices were used to model the instrument's effective area and energy dependent sensitivity matrices were created for each comet separately using the standard CIAO tools.

Due to the large extent of cometary X-ray emission, and *Chandra*'s relatively narrow field of view, it is not trivial to obtain a background uncontaminated by the comet and sufficiently close in time and viewing direction. We extracted background spectra using several techniques: spectra from the S3 chip in an outer region generally > 8′, an available ACIS S3 blank sky observation, and backgrounds extracted from the S1 CCD. For several comets there are still a significant number of cometary counts in the outer region of the S3 CCD. Background spectra taken from the S1 chip have the advantage of having been taken simultaneous with the S3 observation and thus having the same space environment as the S3 observation. In general the background spectra were extracted with the same 7.5′ aperture as the source spectra but centered on the S1 chip. For comet Encke, where the S1 chip was off during the observation the background from the outer region of the S3 chip was used. Comet C/2000 WM1 (LINEAR) was observed with the Low-Energy Transmission Grating (LETG) and ACIS-S array. For the latter, we analyzed the zero-th order spectrum, and used a background extracted from the outer region of the S3 chip. It is possible that the proportion of incident X-rays diffracted onto the S3 chip will vary with photon energy. Background-subtracted spectra generally have a signal-to-noise at 561 eV of at least 10, and over 50 for 153P/2002 C1 (Ikeya-Zhang).

10.3 Spectroscopy

The observed spectra are shown in Fig. 10.8. The spectra suggest a classification based upon three competing emission features, i.e. the combined carbon and nitrogen emission (below 500 eV), OVII emission around 565 eV and OVIII emission at 654 eV. Firstly, the C+N emission (<500 eV) seems to be anti-correlated with the oxygen emission. This clearly sets the spectra of 73P/2006 S.-W.3B and 2P/2003 (Encke) apart, as for those two comets the C+N features are roughly as strong as the OVII emission. In the spectra of the remaining five comets, oxygen emission dominates over the carbon and nitrogen emission below 500 eV. The OVIII/OVII ratio can be seen to increase continuously, culminating in the spectrum of 153P/2002 (Ikeya-Zhang) where the spectrum is completely dominated by oxygen emission with almost comparable OVIII and OVII emission features. From our modeling, we expect that the separate classes reflect different states of the solar wind, which imply different ionic abundances. To explore the obtained spectra more quantitatively, we will use a spectral fitting technique based on our CXE model to extract X-ray line fluxes.

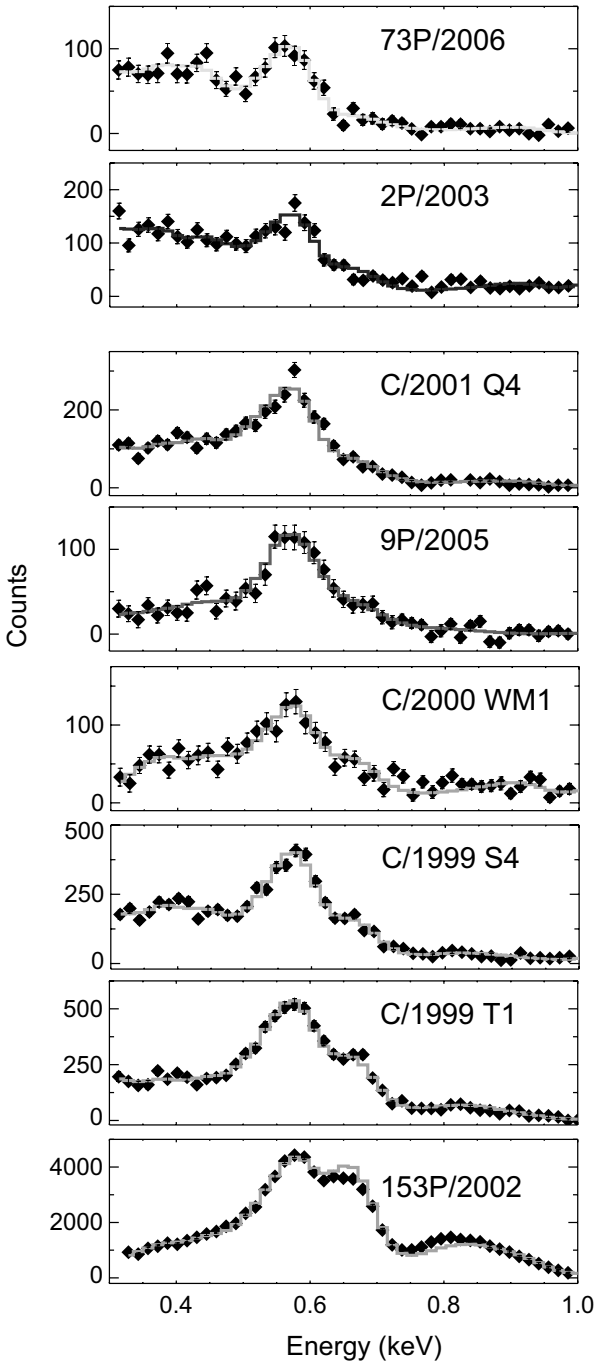

Figure 10.8: *Observed spectrum and fit of all 8 comets observed with Chandra, grouped by their spectral shape (see text). The histogram lines indicate the CXE model fit.*

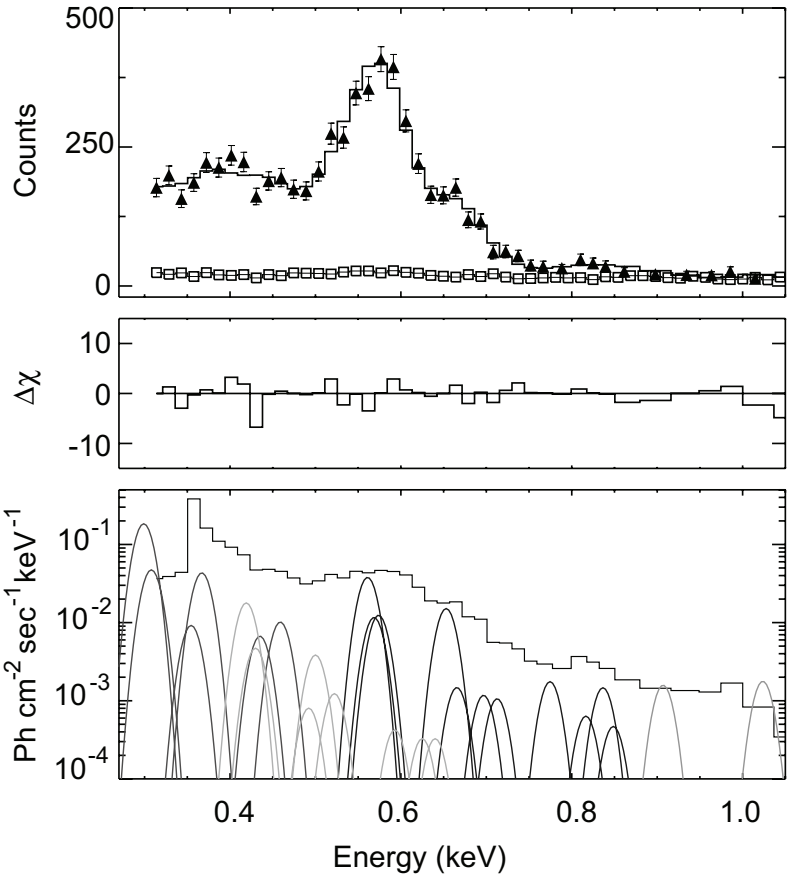

Figure 10.9: *Details of the CXE fit for the spectrum of comet 1999/S4 (LINEAR).* ***Top panel:*** *Comet (filled triangles) and background (open squares) spectrum.* ***Middle panel:*** *Residuals of CXE fit.* ***Bottom panel:*** *CXE model and observed spectrum indicating the different lines and their strengths. The unfolded model is scaled above the emission lines for the ease of presentation.*

10.3.1 Spectral Fitting

The charge exchange mechanism implies that cometary X-ray spectra result from a set of solar wind ions, which produce at least 35 emission lines in the regime visible with *Chandra*. As comets are extended sources, these lines cannot all be resolved. All spectra were therefore fit using the 6 groups of fixed lines of our CXE model (see Table 8.2) and spectral parameters were derived using the least squares fitting procedure with the XSPEC package. The relative strengths and the photon energies of all lines were fixed per ionic species, according to their velocity dependent emission cross sections. Thus, the free parameters were the interaction velocity and the relative fluxes of the C, N and O ions contained in our model.

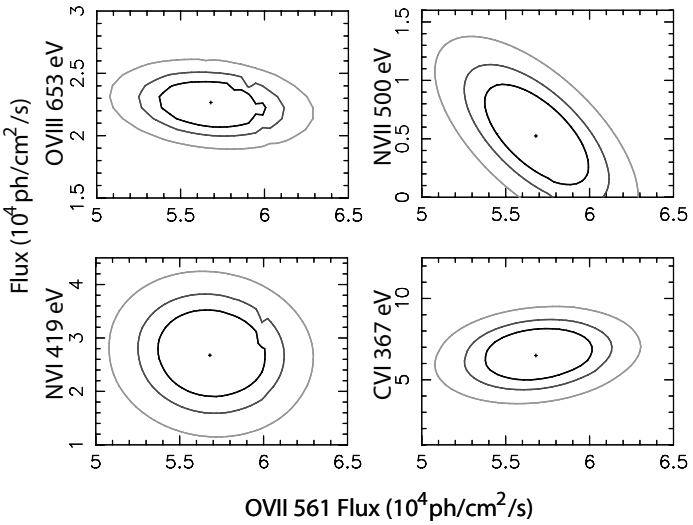

Figure 10.10: *Parameter sensitivity for the major emission features in the fit of C/1999 S4 (LINEAR), with respect to the OVII 561 eV feature. All units are 10^{-4} photons cm^{-2} s^{-1}. The contours indicate a χ^2_R of 9.2 (or 99% confidence, largest contour), a χ^2_R of 4.6 (90%, middle contour) and a χ^2_R of 2.3 (68%, smallest contour).*

Two additional Ne lines at 907 eV (NeIX) and 1024 eV (NeX) were also included, giving a total of 8 free parameters. All line widths were fixed at the ACIS-S3 instrument resolution.

The spectra were fit in the 300 to 1000 eV range. This provided 49 spectral bins, and thus 41 degrees of freedom. ACIS spectra below 300 eV are discarded because of the rising background contributions, calibration problems and a decreased effective area near the instrument's carbon edge.

As a more detailed example of the CXE model and comparison to the data, we show in Fig 10.9 the ACIS-S3 data for C/1999 S4 (LINEAR). The figure shows the background subtracted source spectrum over-plotted with the background spectrum, the difference between the model and data, and the model spectrum and data to indicate to contribution of the different ions. Only the emission lines with >3% strength of the strongest line in their species are shown for ease of presentation.

The fluxes obtained by our fitting are converted into relative ionic abundances by weighting them by their velocity dependent emission cross sections. For comets observed near the ecliptic plane (< 15°), solar wind conditions mapped to the comet were used (Section 2). For comets observed at higher latitudes, these data are most likely not applicable and a solar wind velocity of 500 km s^{-1} was assumed.

Table 10.2: *Results of the CXE-model fit for all cometary spectra. Fluxes are given in dimensions of 10^{-5} photons cm^{-2} s^{-1}. Errors are obtained by averaging over the calculated + and - 90% confidence contours and averaged those (corresponding to $\chi^2 = 2.7$ or 1.6 σ)*

Ion	Line (eV)	C/1999 S4 (LINEAR)	C/1999 T1 (McNaught-Hartley)	C/2000 WM1 (LINEAR)	153P /2002 (Ikeya-Zhang)	2P/2003 (Encke)	C/2001 Q4 (NEAT)	9P/2005 (Tempel 1)	73P/2006 (SW3-B)
OVIII	653	23 ± 2.0	25 ± 1.6	20 ± 3.9	357 ± 14	1.95 ± 0.36	9.7 ± 1.7	3.5 ± 0.98	1.5 ± 0.57
OVII	561	57 ± 3.4	47 ± 2.7	52 ± 7.1	296 ± 1.0	7.12 ± 0.84	52 ± 4.3	16 ± 1.6	11 ± 1.3
CVI	368	65 ± 17	36 ± 15	85 ± 40	288 ± 1.8	18 ± 7.0	47 ± 36	0.5 ± 7.0	21 ± 10
CV	299	276 ± 85	278 ± 90	62 ± 193	1052 ± 18	192 ± 62	809 ± 280	121 ± 89	326 ± 109
NVII	500	5.2 ± 4.7	11 ± 3.6	9.8 ± 9.2	98 ± 1.6	1.3 ± 1.2	17 ± 6.4	0 ± 0.98	0.1 ± 1.25
NVI	420	27 ± 8.5	17 ± 6.9	19 ± 19	123 ± 0.84	4.8 ± 3.3	36 ± 16	7.6 ± 5.0	13.0 ± 6.0
NeIX	907	2.4 ± 1.1	1.97 ± 0.67	6.7 ± 1.7	38 ± 0.11	0.68 ± 0.2	1.4 ± 0.54	0 ± 0.17	0.48 ± 0.24
NeX	1024	2.7 ± 1.2	0.41 ± 0.47	4.6 ± 2.1	8.2 ± 0.02	0.72 ± 0.24	0.8 ± 0.46	0.07 ± 0.22	0.02 ± 0.25
χ^2_R		1.4	1.1	1.4	1.7	1.4	1.4	0.91	1

Table 10.3: *Solar wind abundances relative to O^{7+}, obtained from the CXE-model fit.*

Ion	C/1999 S4 (LINEAR)	C/1999 T1 (McNaught-Hartley)	C/2000 WM1 (LINEAR)	153P /2002 (Ikeya-Zhang)	2P/2003 (Encke)	C/2001 Q4 (NEAT)	9P/2005 (Tempel 1)	73P/2006 (SW3-B)
O^{8+}	0.32 ± 0.03	0.42 ± 0.04	0.31 ± 0.07	0.96 ± 0.04	0.19 ± 0.04	0.17 ± 0.03	0.19 ± 0.06	0.10 ± 0.04
C^{6+}	1.4 ± 0.4	0.95 ± 0.4	2.0 ± 1.0	1.21 ± 0.0	2.9 ± 1.1	1.2 ± 0.9	0.0 ± 0.6	2.3 ± 1.1
C^{5+}	12 ± 3.8	15 ± 4.8	3.0 ± 9.3	8.9 ± 0.2	56 ± 19.3	49 ± 17.4	22 ± 15.9	71 ± 24.9
N^{7+}	0.07 ± 0.06	0.19 ± 0.06	0.14 ± 0.14	0.25 ± 0.00	0.14 ± 0.13	0.25 ± 0.10	0.00 ± 0.05	0.008 ± 0.08
N^{6+}	0.63 ± 0.21	0.47 ± 0.20	0.49 ± 0.49	0.56 ± 0.00	0.79 ± 0.55	1.1 ± 0.52	0.72 ± 0.48	1.5 ± 0.72
Ne^{10+}	0.02 ± 0.01	0.004 ± 0.005	0.044 ± 0.02	0.01 ± 0.0001	0.05 ± 0.02	0.008 ± 0.004	0.002 ± 0.007	0.001 ± 0.01

Table 10.4: *Solar wind abundances relative to O^{7+}, obtained for comet LINEAR S4. References: Bei '03 – Beiersdorfer et al. (2003), Kra '04 – Krasnopolsky et al. (2004a), Kra '06 – Krasnopolsky (2006), Otr '06 – Otranto et al. (2006) and S&C '00 – Schwadron and Cravens (2000). Dots indicate that an ion was included in the fitting, but no abundances were derived; dash means that an ion was not included in the fitting. Otranto et al. (2006) did not fit the observed spectrum, but used a combination of ACE-data and solar wind averages (Schwadron and Cravens, 2000) to compute a syntectic spectrum of the comet. Solar wind averages are given for comparison Schwadron and Cravens (2000).*

Ion	this work	Bei '03	Kra '04	Kra '06	Otr '06	S&C '00
O^{8+}	0.32 ± 0.03	0.13 ± 0.03	0.13 ± 0.05	0.15 ± 0.03	0.35	0.35
C^{6+}	1.4 ± 0.4	0.9 ± 0.3	0.7 ± 0.2	0.7 ± 0.2	1.02	1.59
C^{5+}	12 ± 4.0	11 ± 9	...	1.7 ± 0.7	1.05	1.05
N^{7+}	0.07 ± 0.06	0.06 ± 0.02	–	–	0.03	0.03
N^{6+}	0.63 ± 0.21	0.5 ± 0.3	–	–	0.29	0.29
Ne^{10+}	0.02 ± 0.01	–	–	–	–	–
Ne^{9+}	...	–	$(15 \pm 6) \times 10^{-3}$	$(20 \pm 7) \times 10^{-3}$	–	–

10.3.2 Spectroscopic Results

The fits to all cometary spectra are shown in Fig. 10.8 and the results of the fits are given in Table 10.2. For the majority of the comets, the model is a good fit to the data within a 95% confidence limit ($\chi^2_R \approx 1.4$). Results for comet 153P/2002 (Ikeya-Zhang) include an additional systematic error to account for its brightness and any uncertainties in the response.

The spectra for all comets are well reproduced in the 300 to 1000 eV range. The nitrogen contribution is statistically significant for all comets except the fainter ones, 2P/2003 (Encke) and 73P/2006 (S.-W.3B). For example, removing the nitrogen components from LINEAR S4's CXE model and re-fitting, increases χ^2_R to over 7.

χ^2 contours for C/1999 S4 (LINEAR) are presented in Fig 10.10. The line strengths for each ionic species are generally well constrained, except where spectral features overlap. This can be readily seen when comparing the contours for the NVII 500 eV and OVII 561 eV features where a strong anti-correlation exists (Fig. 12). Due to the limited resolution of ACIS an increase in the NVII feature will decrease the OVII strength. Similar anti-correlations exist between the nitrogen NVI or NVII and CV 299 eV lines. Since the line strength for the main line in each ionic species is linked to weaker lines, a range of energies can contribute and better constrain its strength. However with OVII as the strongest spectral feature the nitrogen and carbon components may be artificially lower as a result of the aforementioned anti-correlations. The lack of effective area due to the carbon edge in the ACIS response also may over-estimate the CV line flux. The neon features were well constrained for the brighter comets, but this is a region of lower signal and some caution must be taken when treating the neon line strengths. They are included here largely for completeness.

In the case of 153P/Ikeya-Zhang, $\chi^2_R > 1.4$. The main discrepancy is that the model produces not enough flux in the 700 to 850 eV range compared to the observed spectrum. This

may reflect an underestimation of higher OVIII transitions or the presence of species not (yet) included in the model, such as Fe. This will be discussed further in the last section of this paper and in a separate paper dedicated to the observations of this comet (K. Dennerl, private communication).

One of the best studied comets is C/1999 S4 (LINEAR), because of its good signal-to-noise ratio. To discuss our results, we will compare our findings with earlier studies of this comet. In general, the spectra analyzed here have more counts than earlier analyzes, because of improvements in the *Chandra* processing software and because we took special care to use a background that is as comet-free as possible. Previous studies appear to have removed true comet signal when the background subtraction was performed. In particular, both the Krasnopolsky (2004) and Lisse et al. (2001) studies used background regions from the outer part of the S3 chip and this may have still had true cometary emission. Krasnopolsky (2004) subtracted over 70% of the total signal as background. We find that using the S1-chip, the background contributes only 20% of the total counts.

Different attempts to derive relative ionic abundances from C1999/S4's X-ray spectrum are compared in Table 10.4. Our atomic physics based spectral analysis combines the benefits of earlier analytical approaches (Kharchenko and Dalgarno, 2000, 2001; Beiersdorfer et al., 2003). These methods were all applied to just one or two comets. Beiersdorfer et al. (2003) interpret C1999/S4's X-ray spectrum by fitting it with 6 experimental spectra obtained with their EBIT setup. The resulting abundances are very similar to ours. The advantage of their method is that it includes multiple electron capture, but in order to observe the forbidden line emission, the spectra were obtained with trapped ions colliding with CO_2, at collision energies of 200 to 300 eV or approximately 30 km s^{-1}. As was shown in Fig. 8.5, the CXE hardness ratio may change rapidly below 300 km s^{-1}, implying an overestimation of the higher order lines compared to the $n = 2 \rightarrow 1$ transition, which for OVII overlap with the OVIII emission. We therefore find higher abundances of O^{8+}.

Krasnopolsky (2004) and Krasnopolsky (2006) obtained fluxes and ionic abundances by fitting the spectrum with 10 lines of which the energies were semi-free. Their analysis thus does not take the contamination of unresolved emission into account, and NVI and NVII are not included in the fit. The line energies were attributed to CXE lines of mainly solar wind C and O but also to ions of Mg and Ne. The inclusion of the resulting low energy emission (near 300 eV) results in lower C^{5+} fluxes (see also Otranto et al., 2006).

Our results indicate unexpectedly high CV fluxes, or low low CVI/CV ratios. There are several factors that may contribute to this: 1) There may be a small contribution to the CV line from other ions in the 250 – 300 eV range (e.g. Si, Mg, Ne) that are currently not included in the model. Including these species in the model would lower the CV flux, but probably only with a small amount. 2) The low ACIS effective area in the 250-300 eV region allows the CV flux to be unconstrained, and this increases the uncertainty in the CV flux. We estimate that the uncertainty in the effective area, introduced by the carbon edge, can account for an uncertainty as large as a factor of 10 in the observed CV/CVI ratios.

We will not compare our results with measured ACE/SWICS ionic data. As discussed in section 10.2, the solar wind is highly variable in time and its composition can change dramatically over the course of less than a day. Variations in the solar wind's ionic composition are often more than 50% during the course of an observation. Data on N, Ne, and O^{8+} ions have not been well documented as the errors of these abundances are dominated

by counting statistics. As discussed above, latitudinal and corotational separations imply large inaccuracies in any solar wind mapping procedure. These conditions clearly disfavor modeling based on either average solar wind data or ACE/SWICS data.

10.4 Comparative Results

As noted in Section 10.3, the spectral differences are best visible in the behavior of the low energy C+N emission (< 500 eV), the OVII emission at 561 eV and the OVIII emission at 653 eV. Fig. 10.11 shows a color plot of the fluxes of these three emission features, and Fig. 10.12 the corresponding ionic abundances. There is a clear separation between the two comets with a large C+N contribution and the other 'oxygen-dominated' comets, which on their turn show a gradual increase in the oxygen ionic ratio. This sample of comet observations suggest that we can distinguish two or three spectral classes.

Table 10.5 surveys the comet parameters for the different spectral classes. The outgassing rate, heliocentric- or geocentric distance and comet family do not correlate to the different classes, in accordance with our model findings. The data does suggest a correlation between latitude and wind conditions during the observations. At first sight, the apparent correlation between latitude and oxygen ratio seems paradoxical. According to the bimodal structure of the solar wind, the fast, cold wind dominates at latitudes > 15°, implying less OVIII emission. In Fig. 10.6, the comet observations are shown with respect to the phase of the last solar cycle. Interestingly, we note that all comets that were observed at higher latitudes were observed around solar maximum. The solar wind is highly chaotic during solar maximum and the frequency of impulsive events like CMEs is much higher than during the descending and minimum phase of the cycle. This explains both why the comets observed in the period 2000 – 2002 encountered a disturbed solar wind and why our survey does not contain a sample of the cool fast wind from polar coronal holes.

The observed classification can therefore be fully ascribed to solar wind states. The first class is associated with cold, fast winds with lower average ionization. These winds are found in CIRs and behind flare related shocks. The spectra due to these winds are dom-

Table 10.5: *Correlation between classification according to spectral shape and comet/solar wind characteristics during the observations. Comet families from Marsden, B.G. and Williams, G.V. (2005). For other references, see Table 10.1.*

Class	#	Comet	Comet Family	Q (10^{28} mol. s^{-1})	Latitude	Wind Type
cold	H	73P/2006 (S.-W.3B)	Jupiter	2	0.5	CIR
	E	2P/2003 (Encke).....	Jupiter	0.7	11.4	Flare/PS
warm	F	C/2001 Q4 (NEAT)	*unknown*	10	-3	Quiet
	G	9P/2005 (Tempel 1)	Jupiter	0.9	0.8	Quiet
hot	C	C/2000 WM1 (LINEAR)	*unknown*	3-9	-34	PS
	A	C/1999 S4 (LINEAR)	*unknown*	3	24	ICME
	B	C/1999 T1 (McNaught-Hartley)	*unknown*	6-20	15	Flare/CIR
	D	C/2002 C1 (Ikeya-Zhang)	Oort	20	26	ICME

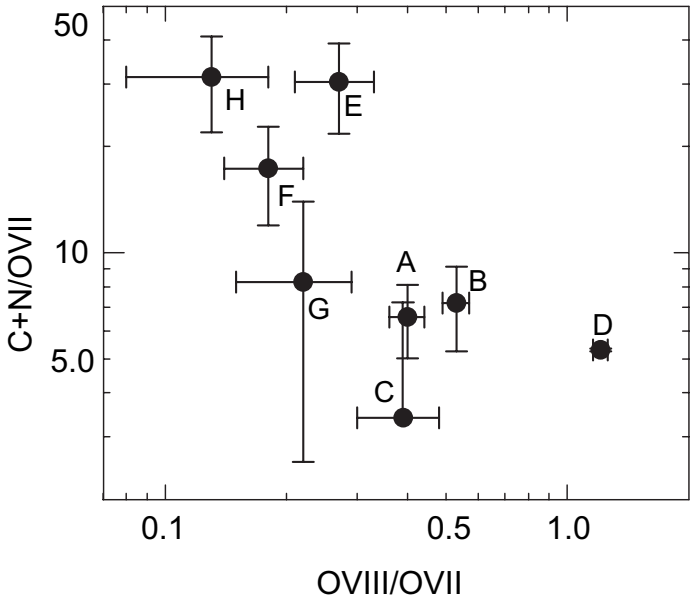

Figure 10.11: *Flux ratios of all observed comets. The low energy C+N feature is anti-correlated to the oxygen ionic ratio. Letters refer to the chronological order of observation.*

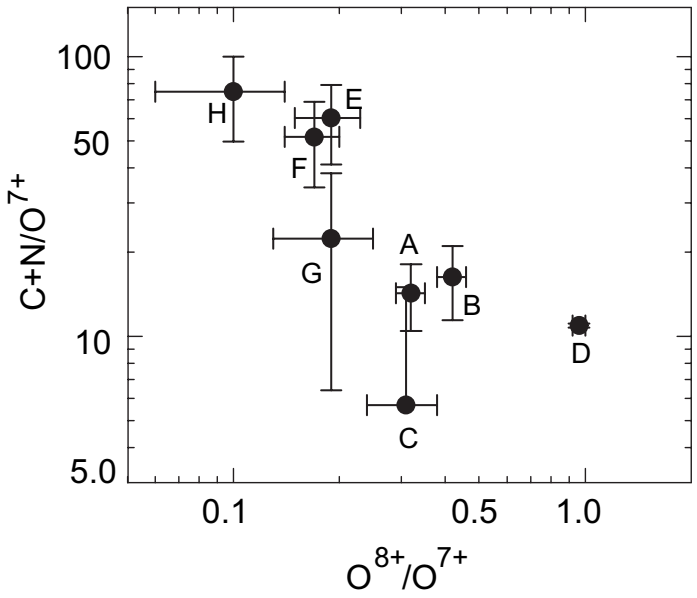

Figure 10.12: *Ion ratios of all observed comets. The C+N ionic abundance is anti-correlated to the oxygen ionic ratio. Letters refer to the chronological order of observation.*

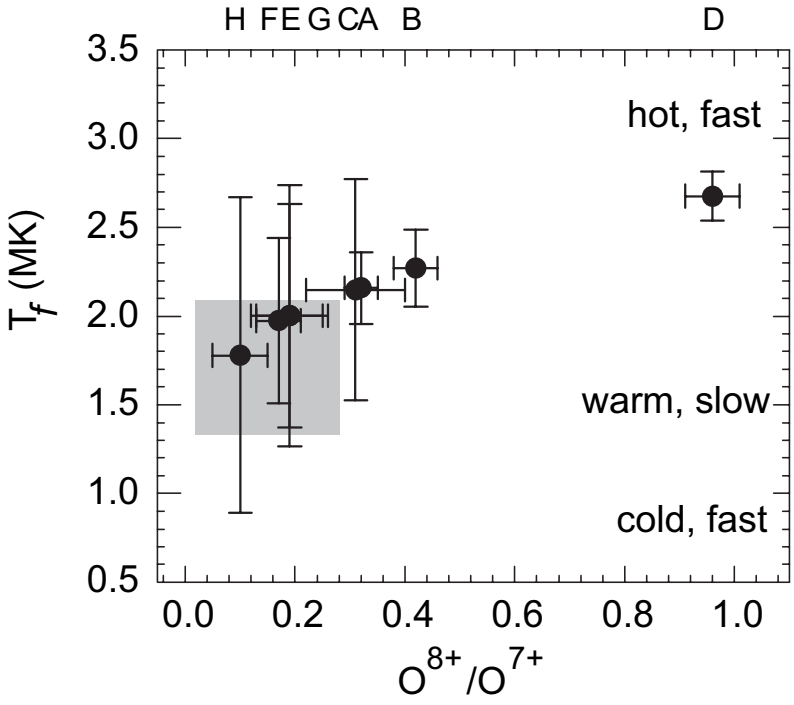

Figure 10.13: *Spectrum derived ionic oxygen ratios and corresponding freezing-in temperatures from Mazzotta et al. (1998). The shaded area indicates the typical range of slow wind associated with streamers. Letters refer to the chronological order of observation.*

inated by the low energy X-rays, because of the low abundances of highly charged oxygen. At the relevant temperatures, most of the solar wind oxygen is He-like O^{6+}, which does not produce any emission visible in the 300 – 1000 eV regime accessible with *Chandra*. Secondly, there is an intermediate class with two comets that were all observed during periods of quiet solar wind. These comets interacted with the equatorial, warm slow wind. The third class then comprises comets that interacted with a fast, hot, disturbed wind associated with ICMEs or flares. From the solar wind data, Ikeya-Zhang was probably the most extreme example of this case. This comet had 10 times more signal than any other comet in our sample and small discrepancies in the response may be important at this level. Extending into the 1-2 keV regime, a preliminary analysis indicates the presence of bare and H-like Si, Mg and FeXV-XX ions, in accordance with ACE measurements of ICME compositions (Lepri and Zurbuchen, 2004).

The variability and complex nature of the solar wind allows for many intermediate states in between these three categories (Zurbuchen et al., 2002), and is reflected in the gradual increase of the OVIII/OVII ratio that we observed in the cometary spectra. As the solar wind is a collisionless plasma, the charge state distribution in the solar wind is linked to the temperature in its source region. Ionic temperatures are therefore a good indicator

of the state of the wind encountered by a comet. The ratio between O^{7+} and O^{6+} ionic abundances has been demonstrated to be a good probe of solar wind states. Zurbuchen et al. (2002) observed that slow, warm wind associated with streamers typically lies within $0.1 < O^{7+}/O^{6+} < 1.0$, corresponding to freezing in temperatures of 1.3 – 2.1 MK. The corresponding temperature range is indicated in the Fig. 10.13. In the figure, we show the observed O^{8+} to O^{7+} ratios and the corresponding freezing-in temperatures from the ionizational/recombination equilibrium model by Mazzotta et al. (1998). Most observations are within or near to the streamer-associated range of oxygen freezing in temperatures. Four comets interacted with a wind significantly hotter than typical streamer winds, and in all four cases we found evidence in solar wind archives that the comets most likely encountered a disturbed wind.

10.5 Conclusions

Cometary X-ray emission arises from collisions between bare- and H-like ions (such as C, N, O, Ne, ...) with mainly water and its dissociation products OH, O and H. The manifold of dependencies of the CXE mechanism on characteristics of both comet and wind offers many diagnostic opportunities, which are explored in the first part of this paper. Charge exchange cross sections are strongly dependent on the velocity of the solar wind, and these effects are strongest at velocities below the regular wind conditions. This dependency might be used as a remote plasma diagnostics in future observations. Ruling out collisional opacity effects, we used our model to demonstrate that the spectral shape of cometary CXE emission is in the first place determined by local solar wind conditions. Cometary X-ray spectra hence reflect the state of the solar wind.

Based on atomic physic modeling of cometary charge exchange emission, we developed an analytical method to study cometary X-ray spectra. First, the data of 8 comets observed with *Chandra* were carefully reprocessed to avoid the subtraction of cometary signal as background. The spectra were then fit using an extensive data set of velocity dependent emission cross sections for eight different solar wind species. Although the limited observational resolution currently available hampers the interpretation of cometary X-ray spectra to some degree, our spectral analysis allows for the unraveling of cometary X-ray spectra and allowed us to derive relative solar wind abundances from the spectra.

Because the solar wind is a collisionless plasma, local ionic charge states reflect conditions of its source regions. Comparing the fluxes of the C+N emission below 500 eV, the OVII emission and the OVIII emission yields a quantitative probe of the state of the wind. In accordance with our modeling, we found that spectral differences amongst the comets in our survey could be very well understood in terms of solar wind conditions. We are able to distinguish interactions with three different wind types, being the cold, fast wind (I), the warm, slow wind (II); and the hot, fast, disturbed wind (III). Based on our findings, we predict the existence of even cooler cometary X-ray spectra when a comet interacts with the fast, cool high latitude wind from polar coronal holes. The upcoming solar minimum offers the perfect opportunity for such an observation.

11 Summary and Outlook

The interaction of the solar wind with the planets, moons and the interstellar medium has been of key importance for the evolution of our solar system. The interaction with Earth's atmosphere is best known for the Northern Lights. In case of Mars, the interaction with the solar wind might have lead to the erosion of its atmosphere. Solar wind-atmosphere interactions can be studied particularly well in cometary atmospheres, because in that case the solar wind flow is not attenuated by a planetary magnetic field and interacts directly with its atmosphere, the coma. The size of the cometary atmosphere (in the order of $10^4 - 10^5$ km) allows remote tracking of the ions as they penetrate into the comet's atmosphere, offering a unique window on the cometary atmosphere, the solar wind and the interaction of these two plasmas.

When solar wind ions fly through an atmosphere they are neutralized via charge exchange reactions with the neutral gaseous species. These reactions depend strongly on target species and collision velocity. The resulting X-ray and Far-UV emission can therefore be regarded as a fingerprint of the underlying reaction, with many diagnostic qualities.

To explore the diagnostics of this emission, I performed experimental studies of charge exchange reactions typical for cometary and planetary atmospheres by means of a technique called 'Photon Emission Spectroscopy'. Here, ions fly through a neutral gas jet. The velocity of the ions can be controlled via ion optics. The light emitted after electron capture is observed with an Extreme Ultraviolet spectrometer and this allows for the measurement of state-to-state charge transfer cross sections and the resulting emission cross sections. Among the typical experiments performed were collisions between solar wind ions (He^{2+}, O^{6-7+}, N^{7+}, ...) and target gases relevant for cometary- and planetary atmospheres, such as H_2O, CO_2, CO and CH_4, all at velocities typical for the solar wind (200 – 1500 km s^{-1}). These experiments were the first comprehensive study that was fully designed for its astronomical application. It showed that for velocities typical for the solar wind multiple electron capture, a process that thus far had not been accounted for, becomes the most important reaction channel in those comet-wind interactions where ion are severely decelerated.

Based upon the charge exchange cross sections measured in the lab, I have developed an astrophysical model that calculates cometary Far-UV spectra. This model was used to analyze existing observations by the *Extreme Ultraviolet Explorer* of the helium emission

lines of comets Hale-Bopp and Hyakutake. By combining the model with solar wind data from the instruments on board ACE and *Ulysses*, we were able to analyze the observations of these two comets in terms of solar wind and coma characteristics. In particular the case of Hale-Bopp was of great interest, as our results indicate severe post-bow shock cooling of the solar wind in this extraordinary large comet. As such, our studies were the first remote, quantitative observations ever of local plasma conditions like temperature and density in the interaction zone, which were thus far only accessible by in situ exploration.

The model was then further expanded to calculate the much more complex cometary X-ray emission, involving charge exchange of solar wind C, N, and O ions with cometary H, O, and H_2O species. Modern X-ray observatories, such as *Chandra* and XMM-*Newton* provide the observer with spatial, temporal and spectral data. Based on our charge exchange model, an analytical method to study cometary X-ray spectra was developed, which for the first time allowed a comparative study of all comets thusfar observed with *Chandra*. The spectra were fit using an extensive data set of velocity dependent emission cross sections for eight different solar wind species. It was demonstrated that a comparison of the fluxes of the carbon and nitrogen emission below 500 eV, the OVII emission and the OVIII emission yields a quantitative probe of the state of the wind. In accordance with our modeling, the analysis showed that spectral differences can be ascribed to different solar wind states, as such identifying comets interacting with (I) fast, cold wind, (II), slow, warm wind and (III) disturbed, fast, hot winds associated with interplanetary coronal mass ejections.

Last but not least, the model was also used to develop observational strategies and it served as the basis for successful proposals to observe comet Schwassmann-Wachmann 3 (SW3) with XMM-*Newton*, *Chandra* and *Swift*. SW3 is a unique comet, because both of its orbit and because of its state. In 1995, SW3 suddenly broke into three pieces and during its apparition in 2006, some of these cores fragmented even further. The comet's extremely close encounter (<0.07 AU) to Earth in May 2006 provided an unprecedented spatial resolution of up to 300 km in the areas around the nucleus. As charge exchange emission is excellent for tracing thin gas, this allowed for an unprecedented study of the interaction of the solar wind with the neutral coma, the macroscopic structure of the magnetohydrodynamic flow, and the microscopic physical processes. Even more, these observations allow for a direct comparison with independent, simultaneous in situ measurements of solar wind conditions measured by near-Earth satellites like SOHO and ACE. This study provides a test bed for our insight in such interactions not only for the solar-wind-coma case but also in the wider context of physical processes in wind-environment collisions.

Thus, my thesis studies have focussed on all aspects relevant for X-ray emission from comets: experimental studies of state-to-state charge exchange cross sections, observations of X-ray emission from comets using all X-ray satellites (*Chandra*, XMM-*Newton*, and *Swift*), and theoretical modeling of the interaction of solar wind ions with cometary gases and the resulting X-ray emission spectrum. Together, this has greatly improved our understanding of the interaction of the solar wind with solar system objects and in more general, of physical processes in wind-environment collisions. The thorough understanding of cometary charge exchange emission has opened the door to the direct observation of more complex solar wind interactions such as those with Mars and Venus.

11.1 Outlook

Where to go from here? All three aspects of the study of cometary X-rays mentioned above have their own challenges, and I will therefore give some suggestions for future work each of them separately.

11.1.1 Charge Exchange Data

Recent experiments of relevance to comet – solar wind interactions, including those described in this thesis, have mainly been focussed on water (see e.g. Chapters 5 – 7 and references therein). Based on our model however, we concluded that beyond some 10^5 km from the nucleus, the main electron donors in the coma will be the water dissociation products OH, H and O. Because of the difficulty of producing dense atomic oxygen targets only experiments have been performed with protons and He^{2+} ions (McCullough et al., 1992; Thompson et al., 1996a,b). Even this data covers only the high energy side of the relevant collision energies. For highly charged ions, no experimental data is available. For such complex many-electron targets as O, theory is also still lacking. Calculations of single- and multiple electron capture for the interaction of multiply charged ions with atomic oxygen with its four equivalent 2p electrons and open shell structure will be very involved. Therefore, experimental data is urgently required. Such data by itself may also serve as an important driver and benchmark for theoretical developments.

11.1.2 Comet Observations

It was demonstrated in this thesis that cometary X-ray spectra are complex but highly diagnostic. The current generation of slitless spectrometers cannot completely resolve these spectra due to the extent of the cometary emission. It was argued in Chapter 10 that cometary spectra in the 300 – 1000 eV consist of at least 35 emission lines from the 6 most abundant solar wind species, and many of these lines overlap. Potential diagnostics such as triplet-to-singlet ratios (Chapter 7) or hardness ratios (Chapter 10) are therefore not accessible observationally. This will change with next generation of X-ray observatories that will carry calorimeters, providing a spectral resolution better than 2 eV. After the unfortunate fate of the XRS calorimeters on board *Astro-E* and *Suzaku*, the next calorimeter missions are currently planned for launch after 2015 (XEUS and *Constellation-X*).

Interestingly, the observational sample of the *Chandra* comet survey (Chapter 10) did not seem to contain a comet interacting with the cool polar winds, as all comets observed at high latitudes were observed in solar maximum and therefore interacted with hot, disturbed winds. The upcoming solar minimum therefore provides an excellent opportunity for an observation of a comet interacting with the cool, polar wind. In particular, the orbit of comet 8P/Tuttle is well suited to test this idea, as its orbit is highly inclined with respect to the ecliptic. It is of note that such observations require careful planning, as the charge states in the polar wind are much lower. The comet will therefore be very faint above 500 eV.

Within the survey, the case of comet Ikeya-Zhang demonstrated that ICMEs leave unique fingerprints when interacting with neutral gas. The resulting CXE is characterized by

its enhanced X-ray brightness and the hot charge state distributions visible in the 0.2 – 2.0 keV spectrum, thus providing a very promising X-ray flashlight.

First, these features could be used to track the propagation of an ICME throughout the inner solar system as it interacts with different solar wind objects. After the disconnection event in the solar corona, ICMEs move away from the Sun with velocities of 1000 – 2000 km s^{-1}. At these velocities, it takes about 1 – 2 days to travel from the Sun to Earth, where many space-borne solar wind instruments are available (ACE, SOHO). Beyond 1 AU, ICMEs quickly decelerate when they plough through the much slower background solar wind. Current propagation models claim an accuracy of less than 11 hours, whereas a typical ICME event lasts for more than a day. These timescales allow for triggered X-ray observations. By combining solar observations (STEREO, SOHO) and solar wind measurements at L1 with triggered Swift observations it becomes possible to track an ICME as it interacts with various objects on its way. Targets of choice could be any planet or comet that is well aligned within the ICME propagation direction at the time of the observations.

Secondly, ICMEs can carry about an order of magnitude more heavy ions. Using ICMEs as X-ray flashlights might allow the study of CXE in objects that are not easily observable in X-ray under 'normal' conditions - for example Jupiter and Saturn.

11.1.3 CXE Emission around Young Stars

Charge exchange occurs whenever highly charged ions from a hot plasma collide with a neutral gas. Besides comets, there are many environments where such interactions occur, and the resulting emission might provide a power diagnostics of local conditions. A significant part of the diffuse X-ray background has been ascribed to the interaction between the solar wind ions and the in streaming neutral gas from the interstellar medium (Snowden et al., 2004; Pepino et al., 2004). From these observations, it is to be expected that charge exchange emission also occurs in astrospheres and disks around other stars. The strong forbidden line emission following charge exchange is distinctly different from typical stellar values and is therefore a good tracer of wind-disk interactions. A limited number of young stars have recently been observed with *Chandra*, XMM-*Newton* or even a combination of the two observatories. These high resolution X-ray spectroscopy observations resolved the very diagnostic OVII forbidden, resonance and intercombination lines (f, i and r, respectively). The observations showed very low f/i ratios for the four T Tauri stars observed (Robrade and Schmitt, 2006). Only one HAeBe star –AB Aur– has been studied with XMM-*Newton* and, interestingly, a high f/i ratio was found. The authors explored several X-ray emission mechanisms in their paper, and tentatively concluded that the X-ray production may be related to the stellar wind. Signatures of charge exchange might thus be found either directly in the spectra of young stellar objects, or by examining the behavior of the relative strengths of the f, i and r lines around stellar disks (as in the case of the XMM-Mars observations). The discovery of charge exchange emission in disks around young stars would provide an important new diagnostic, as both Doppler shifts of charge exchange emission lines and their absolute- and relative intensities can provide information on local plasma parameters such as temperatures, velocities, elemental abundances and charge state distributions of the interacting plasmas.

12 Samenvatting

De invloed van de zonnewind op planeten en het instellaire medium is van groot belang voor de evolutie van ons zonnestelsel. Op aarde is het noorderlicht de bekendste manifestatie van de zonnewind. In het geval van Mars heeft de interactie waarschijnlijk geleid tot de erosie van de atmosfeer van de planeet. Kometen zijn bij uitstek geschikt om de invloed van de zonnewind op atmosferen te bestuderen, omdat kometen geen magnetisch veld hebben. Dit betekent dat de zonnewind direct kan reageren met het gas in de komeetatmosfeer ('coma'). De relatief grote omvang van de coma (in de orde van een miljoen km) maakt het mogelijk de zonnewind te volgen tijdens hun interactie met het kometengas. Dit biedt een unieke kijk op de komeet, de zonnewind en de interactie tussen deze twee.

De zonnewind bestaat uit geladen deeltjes (ionen) die vanuit de buitenste lagen van de zonneatmosfeer (corona) de ruimte in schieten. Wanneer de ionen op een neutraal gas botsen, worden ze (deels) geneutraliseerd via elektronenvangst. De deeltjes zitten dan in aangeslagen toestanden. Via lichtemissie vervallen ze vervolgens naar de grondtoestand van de laagste interne energie. Dit soort processen is uitgebreid bestudeerd met het oog op diagnostische toepassingen in kernfusiereactoren zoals het toekomstige ITER. Bij elk invangstproces wordt één specifieke kleur licht uitgezonden; een 'spectraallijn'. De kleur van zo'n lijn ligt vaak ver buiten het zichtbare licht en wordt daarom aangegeven met de bijbehorende golflengte in nanometers (nm, zie Figuur 12.1). De golflengte van het uitgestraalde licht wordt bepaald door de eigenschappen van de botsende deeltjes. De straling kan daardoor gebruikt worden om van buitenaf processen, temperaturen en dichtheden in de reactor in kaart te brengen.

In 1996 werd tot grote verbazing van astronomen ontdekt dat kometen felle röntgenbronnen waren. Voor dergelijke straling zijn normaal gesproken temperaturen van miljoenen graden nodig, terwijl kometen bekend staan als 'vieze sneeuwballen'. De straling bleek te ontstaan als zonnewindionen elektronen vingen uit de komeetatmosfeer. Mijn onderzoeksvraag was dan ook of kometair röntgenlicht gebruikt kan worden om de interactie tussen kometen en de zonnewind op afstand te bestuderen. Dit proefschrift laat zien dat dit zeker mogelijk is door de resultaten van atoomfysische experimenten te koppelen aan astronomische waarnemingen. In deze samenvatting worden de belangrijkste resultaten kort aangestipt.

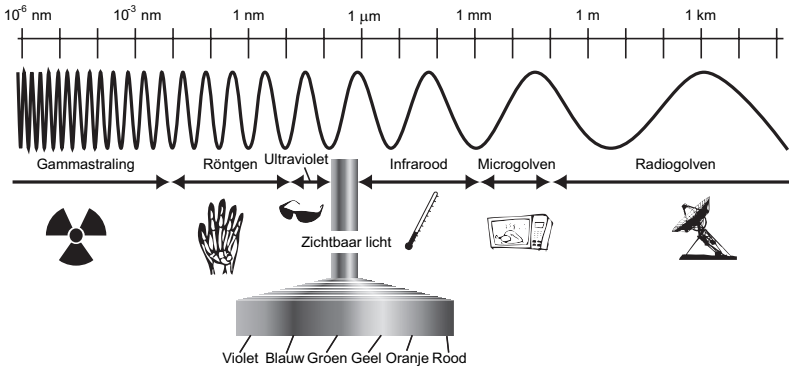

Figuur 12.1: *Zichtbaar licht is maar een klein deel van het elektromagnetisch spectrum. UV en röntgenlicht kunnen niet met het menselijk oog gezien worden en worden daarnaast tegengehouden door de atmosfeer van de aarde. Waarnemingen van dit licht moeten dus gedaan worden met ruimtetelescopen (Figuur door R. Boomsma).*

12.1 Kometen en de zonnewind

Komeetkernen zijn tussen de 1 en 10 km groot en zijn overblijfselen van het begin van het zonnestelsel (Figuur 12.2). In de buitenste regionen van het zonnestelsel zijn kometen diepgevroren mengsels van ijs en stof, maar dat verandert wanneer ze in de richting van de zon vliegen in lange, elliptische banen. Verwarming door de zon zorgt dat een komeet ter hoogte van de aarde enorme hoeveelheden gas produceert (duizenden liters per seconde!), voornamelijk water, maar ook CO (ongeveer 10%) en geringe concentraties van andere gassen (CO_2, CH_4, etc.). Dit gas spuit in krachtige stromen de komeetkern uit en sleurt daarbij grote hoeveelheden stof met zich mee. Het gas en stof vormen een grote wolk om de komeetkern, de 'coma' genaamd. De zwaartekracht van een komeetkern is te klein om de coma aan zich te binden waardoor deze zich uitspreidt. De grootte van de coma wordt slechts begrensd doordat moleculen in het gas worden afgebroken door zonlicht. Op zo'n 100 000 kilometer van de komeetkern zijn de meeste watermoleculen afgebroken in de fragmenten OH, H en O. Daardoor bevatten de buitenste regionen van de coma een relatief grote hoeveelheid CO en CO_2, moleculen die veel minder snel afgebroken worden door zonlicht.

Het stof uit de coma vormt een stofstaart in de richting van de baan van de komeet (zie Figuur 12.3). Geladen deeltjes van het gas worden juist opgeveegd door de zonnewind, die ze in een bijna rechte staart om de komeetkern blaast. Deze staart wijst dus altijd van de zon af, licht blauw op en kan meer dan een miljard kilometer lang worden.

De zonnewind is een stroom geladen deeltjes afkomstig uit de buitenste lagen van de zonneatmosfeer, de corona. Hij bestaat uit protonen, elektronen en een kleine hoeveelheid hooggeladen helium-, koolstof- en zuurstofionen. De zonnewind heeft rond de aarde een dichtheid van ongeveer tien deeltjes per cm^3, die langsrazen met een snelheid tussen de 100 tot 1000 km/s. De eigenschappen van de zonnewind zijn gekoppeld aan het gebied in de corona waar hij ontstaat. Tijdens het minimum van de 11-jarige cyclus van activiteit

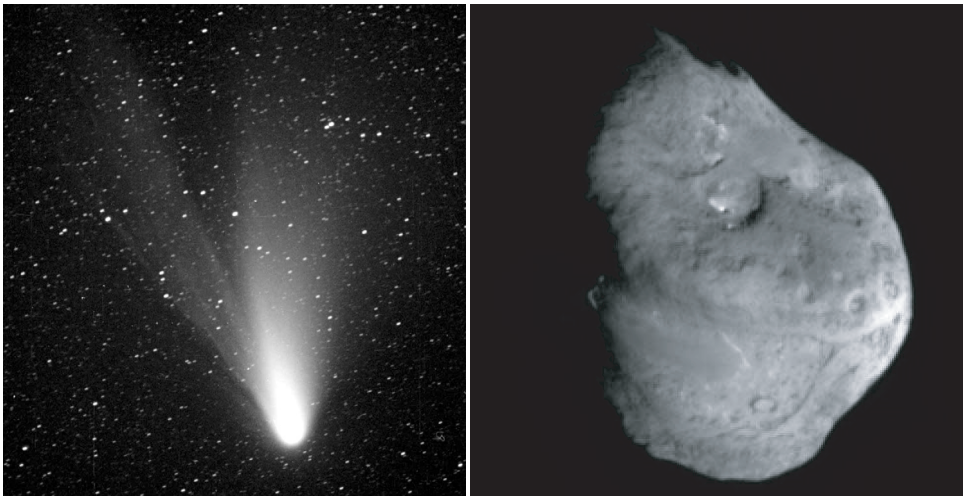

Figuur 12.2: ***Links:*** *Komeet Hale-Bopp in 1996. De twee staarten zijn duidelijk te zien, met links de ionenstaart en rechts de stofstaart.* ***Rechts:*** *De kern van komeet 9P/Tempel 1, vijf minuten voordat de Deep Impact-sonde er op insloeg.*

op de zon is de wind ruwweg in te delen in twee types. In het vlak van de ecliptica, waarin de banen van de aarde en de andere planeten liggen, is de wind langzaam (300 km s^{-1}), variabel (in snelheid, sterkte en lading) en bevat veel hooggeladen ionen. Wind afkomstig van de polen van de zon heeft een hogere snelheid (700 km s^{-1}) en komt uit koudere gebieden in de corona. Hierdoor zijn deze zonnewindionen doorgaans minder hooggeladen. Daarnaast zijn er verschillende onregelmatige structuren in de zonnewind, bijvoorbeeld snelle, zeer hete stromen wind ten gevolge van uitbarstingen op de zon (Coronal Mass Ejections). Tijdens het zonnemaximum verdwijnt de simpele indeling en is de zonnewind hoogst chaotisch.

Een komeet verstoort de zonnewind al op een afstand van ongeveer 100 000 km van de komeetkern. De geladen molecuulfragmenten van het kometengas worden opgepikt door de zonnewind waardoor de wind vertraagt. Dit veroorzaakt een soort boeggolf. Op deze grote afstanden is de coma nog erg ijl en het grootste deel van de zonnewind dringt verder de coma binnen. De zonnewindionen worden geneutraliseerd door middel van ladingsoverdracht met het kometengas (zie volgende sectie). Diep verscholen in de coma ligt het contactoppervlak, een door de hoge gasdichtheid voor de zonnewind ondoordringbare barrière. De neutralisatie van de wind gaat gepaard met het uitzenden van röntgen- en ultravioletlicht en is daarom rechtstreeks te volgen vanaf de aarde. Dit is overduidelijk eenvoudiger dan het ter plekke bestuderen van de wisselwerking met een ruimtemissie en biedt daarnaast de mogelijkheid verschillende kometen in verschillend ruimteweer te observeren.

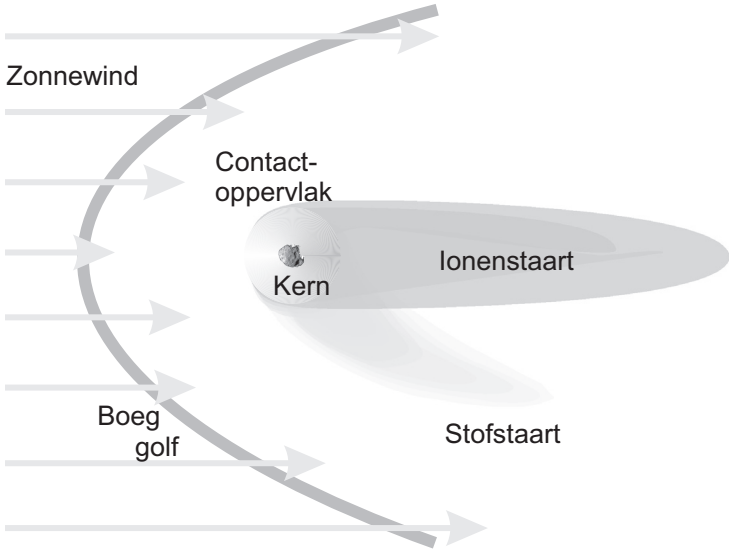

Figuur 12.3: *Schematisch overzicht van de wisselwerking tussen kometen en de zonnewind. De afbeelding is niet op schaal. De komeetkern is zo'n 10 km in doorsnee, het contactoppervlak bevindt zich op ongeveer 1000 km van de kern, de boeggolf op 100 000 km en de ionenstaart kan meer dan een miljard km lang worden.*

12.2 Ladingsoverdracht in het lab...

Wanneer een ion botst met een neutraal deeltje bestaat de kans dat het ion één of meer elektronen wegvangt van de botsingspartner. Ladingsoverdracht is een quasi-resonant proces. Dit betekent dat de energie waarmee het elektron gebonden wordt na invangst ongeveer gelijk is aan de energie waarmee het oorspronkelijk verbonden was aan een neutraal molecuul of atoom. In het geval van hooggeladen ionen betekent dit dat het elektron in een aangeslagen toestand terechtkomt. Het systeem zal vervolgens onder uitzending van licht naar de grondtoestand vervallen. De golflengte (kleur) van dit licht is daardoor een vingerafdruk voor specifieke ladingsoverdrachtprocessen en de omstandigheden waaronder zij plaatsvonden.

In de hoofdstukken 4 – 7 van dit proefschrift beschrijf ik de experimenten waarmee ik onderzocht heb hoe elektronenoverdrachtsprocessen afhangen van de botsingssnelheid van een ion. Deze experimenten waren de eerste in hun soort die volledig waren toegespitst op de astrofysische context. Hooggeladen ionen worden geproduceerd met een Electron Cyclotron Resonance-ionenbron. Vervolgens worden ze door een gasstraal geschoten en met behulp van een spectrometer wordt het licht dat hierbij vrijkomt geanalyseerd. Op deze wijze is het mogelijk ladingsoverdracht tussen verschillende ionen en moleculen te bestuderen bij botsingsnelheden die relevant zijn voor komeet-windinteracties (tussen de 200 en 1500 km s^{-1}).

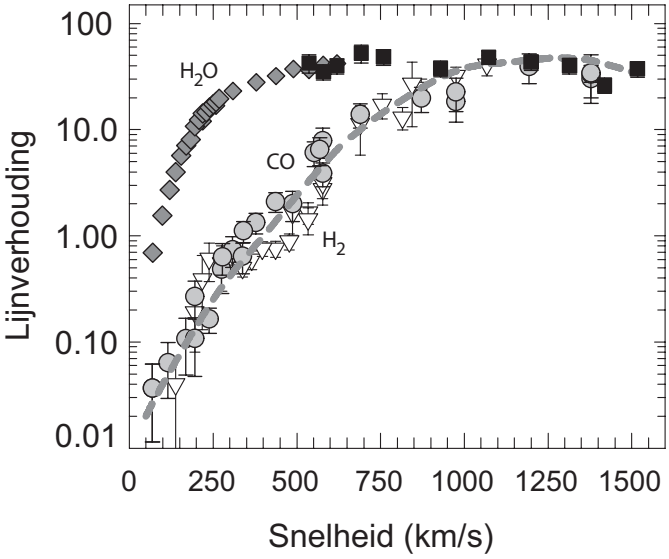

Figuur 12.4: *Verhouding tussen het licht afkomstig na enkel- en dubbelvoudige elektroneninvangst door He^{2+}, als functie van de snelheid. Aangegeven zijn bostingen met H_2, CO en watermoleculen.*

Een mooi voorbeeld om elektroneninvangst te illustreren zijn heliumionen. In het geval van botsingen tussen He^{2+} en kometaire moleculen (H_2O, CO, CO_2, CH_4) blijkt uit onze experimenten dat het spectrum bepaald wordt door twee sterke lijnen. De eerste bevindt zich op 30.4 nm en ontstaat wanneer He^+ van de eerste aangeslagen toestand vervalt naar de grondtoestand. De tweede bevindt zich op 58.4 nm en is afkomstig van neutraal helium. De lijn op 30.4 nm volgt na het invangen van één elektron; de tweede lijn is het resultaat van twee-elektroneninvangst. In Figuur 12.4 is de verhouding tussen beide lijnen weergegeven als functie van de snelheid. Te zien is dat de lijnverhouding meer dan duizendvoudig toeneemt, terwijl de snelheid met slechts een factor tien toeneemt. Dit gedrag suggereert dat het UV-licht directe informatie kan verschaffen over de snelheid van de zonnewind.

12.3 . . . en in kometen

De neutralisatie van de ionen hangt af van de verdeling van het gas rond de komeet en de kans op elektronenvangst. Hoe dit in zijn werk gaat, is goed te illustreren aan de hand van de heliumionen in de zonnewind. Alle heliumionen in de zonnewind zijn volledig ontdaan van hun elektronen door de hoge temperaturen in de corona. In de coma kunnen deze ionen één of twee elektronen invangen en ontstaat er een verdeling over de drie mogelijke ladingstoestanden (He^{2+}, He^+ en He^0). De heliumionen kunnen in één keer geneutraliseerd worden door twee-elektroneninvangst, of door twee opeenvolgende botsingen

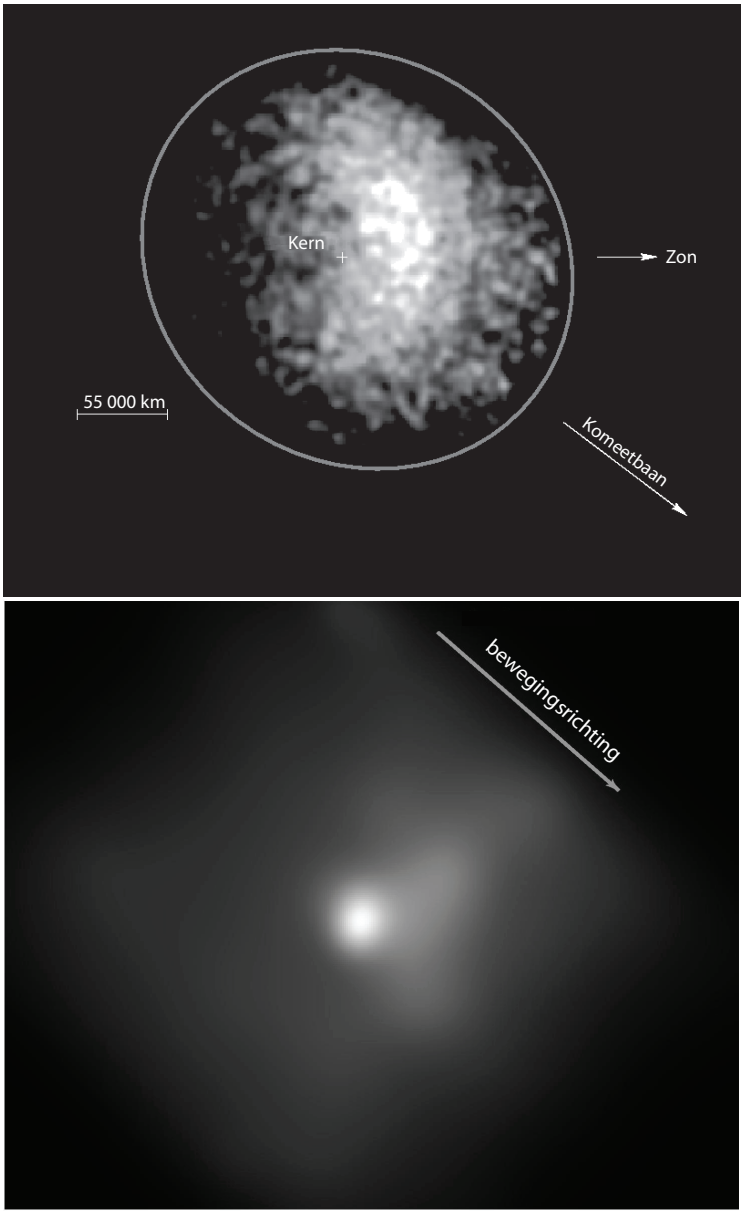

Figuur 12.5: ***Boven:*** *Komeet Hyakutake in 1996, waargenomen met* ROSAT*. De komeet produceerde enorme hoeveelheden gas, waardoor de röntgenstraling de typische halve-maanvorm aanneemt (originele figuur door C. Lisse).* ***Onder:*** *Komeet Encke in 2003, waargenomen met Chandra. Encke was veel minder actief en de zonnewind licht op wanneer zij botst op gasstructuren in de coma. De schaal van de bovenste afbeelding is approximately 7.5 keer groter dan de schaal van de onderste afbeelding. In beide gevallen staat de zon aan de rechterkant.*

waarbij twee keer één elektron ingevangen wordt. De zaak wordt gecompliceerd door de grote wolk atomair waterstof rondom de coma. Een waterstofatoom kan maar één elektron afstaan, waardoor het dubbelinvangstproces onmogelijk is.

De in het lab gemeten lijnverhouding (Figuur 12.4) is dus niet zomaar toe te passen op komeetwaarnemingen. Vandaar dat ik een computermodel ontwikkeld heb dat de komeetatmosfeer beschrijft en dat de ionen volgt tijdens hun vlucht door de coma. Dit model wordt beschreven in hoofdstuk 8. Met behulp van de experimenteel bepaalde werkzame doorsnedes kan zo de ladingsverdeling en de straling van heliumionen op iedere plaats in de coma bepaald worden, wat een gedetailleerde vergelijking met astronomische waarnemingen mogelijk maakt.

In hoofdstuk 9 wordt het model gebruikt om waarnemingen van de Extreme Ultraviolet Explorer (EUVE) te analyseren. De EUVE werd in 2001 uitgeschakeld maar heeft daarvoor twee bekende kometen waargenomen, namelijk Hale-Bopp en Hyakutake. In beide gevallen was de heliumemissie sterk en duidelijk te zien, maar in het geval van Hale-Bopp kon men alleen de 58.4 nm lijn zien en in het geval van Hyakutake slechts de 30.4 nm lijn. Het was een groot raadsel waarom er in beide gevallen maar één van de twee verwachte heliumlijnen te zien was. Met mijn model zijn de waarnemingen goed te verklaren: de verschillen bleken afkomstig van de verschillen in de snelheid en dichtheid van de zonnewind. De waarnemingen van komeet Hale-Bopp bleek helemaal spectaculair. Doordat de zonnewindsatelliet *Ulysses* toevallig in de buurt van de komeet was, kon een goede schatting gemaakt worden van het ruimteweer rond de komeet. De komeet bevond zich op een relatief hoge breedtegraad, middenin de snelle, polaire zonnewind. Toch wezen onze resultaten op een lage ionensnelheid onder de 200 km s^{-1}. Op grote afstand kon gezien worden hoe zonnewindionen sterk vertraagd en afgekoeld waren door de wisselwerking met de komeet. De UV waarnemingen zijn daarmee de eerste kwantitatieve mogelijkheid om de interactie tussen kometen en de zonnewind op afstand te bestuderen.

12.3.1 Kometen als ruimteweersondes

Met slechts 3 mogelijke ladingstoestanden en 2 emissielijnen is de heliumstraling in het UV relatief eenvoudig te interpreteren. Kometaire röntgenstraling is afkomstig van minstens 8 verschillende ionen, en het spectrum bevat meer dan 35 lijnen die elkaar deels overlappen. De bijbehorende spectra zijn daarom veel complexer, maar daar staat tegenover dat hierin een schat van informatie verborgen ligt. Het laatste hoofdstuk van mijn proefschrift beschrijft dan ook de toepassing van het interactiemodel op waarnemingen gedaan met de *Chandra* röntgentelescoop.

Sinds zijn lancering in 1999 heeft de *Chandra*-röntgentelescoop 8 verschillende kometen waargenomen, een rijke verzameling van compleet verschillende kometen in steeds andere ruimteweercondities (zie Figuur 12.5). Om deze waarnemingen te kunnen interpreteren heb ik het heliummodel uitgebreid met zuurstof-, koolstof en stikstofionen. Met dit model heb ik vervolgens onderzocht hoe kometaire röntgenspectra beïnvloed worden door de eigenschappen van de zonnewind (windsnelheid, type) en de komeet (gasproductie). Hieruit kwam naar voren dat het type zonnewind bepalend is voor het spectrum.

Vanuit het model is een methode ontwikkeld die voor het eerst de röntgenwaarnemingen van verschillende kometen kan vergelijken. Met deze methode kon uit ieder waargenomen

spectrum de compositie van de zonnewind afgeleid worden, een belangrijke maat voor de soort wind. Op deze wijze bleek het inderdaad mogelijk de spectra kwantitatief in te delen naargelang het ruimteweer waar de komeet zich in bevond tijdens de waarneming. Een grote verrassing daarbij was dat de komeet Ikeya-Zhang tijdens de *Chandra*-waarnemingen getroffen werd door een Coronal Mass Ejection, de gevolgen van een zonsuitbarsting. Vervolgstudies van deze waarnemingen zullen een unieke kijk bieden op de gevolgen van dit soort geweldadige processen.

Concluderend heb in mijn proefschrift verschillende aspecten van kometaire röntgenemissie onderzocht. Dit omvat onder andere experimenteel onderzoek naar toestandselectieve elektroninvangst, röntgenwaarnemingen met ruimtetelescopen als *Chandra*, XMM-*Newton*en *Swift*, en computersimulaties van de wisselwerking tussen kometen en zonnewind. Dit onderzoek heeft geleid tot een veel beter begrip van de invloed van de zonnewind op verschillende lichamen in ons zonnestelsel en in het algemeen van de fysische processen die verantwoordelijk zijn voor deze wisselwerking.

12.4 Toekomstperspectief

Overal waar heet, geladen gas op een kouder, neutraal gas botst, vindt ladingsoverdracht plaats. Er zijn veel verschillende astrofysische omgevingen waar dit soort botsingen plaats vindt. Net als in het geval van kometen kan de vrijkomende röntgen en UV-straling ook daar een waardevolle diagnostiek bieden.

Planeten worden gevormd uit het gas rond jonge sterren. Stormachtige uitbarstingen van deze sterren hebben een enorme invloed op dit gas en bepalen het lot van toekomstige planetenstelsels. De interactie tussen ster en de omringende gaswolk bepaalt in hoeverre er een planetenstelsel gevormd kan worden. Uit de röntgenastronomie is bekend dat de interactie tussen de zonnewind en neutraal gas dat van buiten het zonnestelsel binnenvliegt achtergrondstraling oplevert. Het valt daarom te verwachten dat planetenstelsels rond andere sterren ook ladingsoverdrachtsstraling uitzenden. Met de technieken die in dit proefschrift gepresenteerd zijn, zou het dus mogelijk kunnen zijn interactie tussen sterrewind en het gas rond jonge sterren te bestuderen. Dit zou unieke kennis over de temperatuur, snelheid en samenstelling van de wind van jonge sterren kunnen opleveren.

A Atomic Units

The atomic unit system is based on the following definitions:

$$\hbar = m_e = e = 4\pi\epsilon_0 = 1, \tag{A.1}$$

where $\hbar$ is Plancks constant divided by 2π, m_e and $-e$ are the mass and the charge of the electron, respectively, and ϵ_0 the permittivity of free space. From the dimensionless fine structure constant $\alpha = e^2/4\pi\epsilon_0 c = 1/137$ one directly sees that the speed of light c in this unit system has a numerical value of 137.

With these definitions all physical quantities are related to that of the hydrogen atom, giving a natural scale in atomic physics. As an example, the Bohr radius a_0, being the radius of the electron in the hydrogen ground state in Bohr's atomic model, is given by $a_0 = 4\pi\epsilon_0\hbar^2/m_e e^2 = 1$. An overview of the most important quantities is given in table A.1.

Throughout this thesis both the projectile velocity and kinetic energy are used. For non-relativistic collision energies the relation between them is given by:

$$\mathrm{v(km\ s^{-1})} = 438\sqrt{E(\mathrm{keV/amu})} \tag{A.2}$$

It is of note that 1 atomic mass unit (amu) is 1/12 of the mass ^{12}C, which is different from one unit of mass in atomic units.

Table A.1: *Overview of the most important physical quantities, giving the SI values related to 1 atomic unit of the corresponding quantity.*

Quantity	SI value	non-SI value	definition
length	$5.29177249 \times 10^{-11}$ m	0.529 Å	a_0
time	$2.41888433 \times 10^{-17}$ s		$a_0(\alpha c)^{-1}$
velocity	2.18769142×10^{6} m s^{-1}		αc
mass.....	$9.1093897 \times 10^{-31}$ kg	511 keV c^{-2}	m_e
energy	4.3593×10^{-18} J	27.2 eV	$m_e(\alpha c)^2$
charge	$1.6021773 \times 10^{-19}$ C		e
momentum	$1.99285337 \times 10^{-24}$ kg m s^{-1}		$m_e\alpha c$
angular momentum	$1.0545887 \times 10^{-34}$ J s		$\hbar = m_e\alpha c a_0$

B Observational Details of the Chandra Comet Survey

This appendix presents the observational details of the *Chandra* data and the corresponding solar wind state. The prefix 'FF' (fearless forecast) used in this appendix refers to the real time forecasting of coronal mass ejection shocks arrivals at Earth. The numbers were so-named for flare/coronal shock events during solar cycle #23.

C/1999 S4 (LINEAR)

X-rays. The first *Chandra* cometary observation was of comet C/1999 S4 (LINEAR) (Lisse et al., 2001), with observations being made both before and after the breakup of the nucleus. Due to the low signal-to-noise ratio of the second detection, only the July 14th 2000 pre-breakup observation is discussed here. Summing the 8 pointings of the satellite gave a total time interval of 9390 s. In this period, the ACIS-S3 CCD collected a total of 11 710 photons were detected in the range 300–1000 eV. Detections out side this range or on other ACIS-CCDs were not attributed to the comet. As a result, data from the S1-CCD (which is configured identically to S3) may be used as an indicator of the local X-ray background.

The morphology can be described by a crescent shape, with the maximum brightness point 24 000 km from the nucleus on the Sun-facing side. The brightness dims to 10% of the maximum level at 110 000 km from the nucleus.

Solar wind. A large velocity jump can be seen around DoY 199, which was due to the famous 'Bastille Day' flare on 14 July (FF#153, Dryer et al., 2001; Fry et al., 2003). This flare reached the comet only after the first observation. At July 12, 2017 UT a solar flare started at N17W65 (FF#152), which was nicely placed to hit this comet with a very high probability during the first observations (Fry et al., 2003). As for the second observation, there was another flare on July 28, S17E24, at 1713 UT (FF#164) and there was a high probability that its shock's weaker flank hit the comet.

C/1999 T1 (McNaught–Hartley)

X-rays. The allocated observing time of comet McNaught-Hartley was partitioned into 5 one-hour-slots between January 8th and January 15th, 2001 (Krasnopolsky et al., 2002). The strongest observing period was on January 8th, when $\Delta = 1.37$ AU and $r_h = 1.26$ AU.

There were 15 000 total counts observed by the ACIS-S3 CCD between 300 and 1000 eV. The emission region can be described by a crescent, with the peak brightness is at 29 000 km from the nucleus. The brightness dims to 10% of the maximum at a cometocentric distance of 260 000 km. Again, the ACIS-S1 CCD may be used to indicate the local background signal.

Solar wind. The comet was not within the heliospheric current/plasma sheet (HCS/HPS). Two corotating CIRs are probably associated with the first two observations. Two flares (FF#233 and #234) took place; however, another corotating CIR more likely arrived before the flare's transient shock's effects did (McKenna-Lawlor et al., 2006).

C/2000 WM1 (LINEAR)

X-rays. The only attempt to use the high-resolution grating capability of the ACIS-S array was made with comet C/2000 WM1 (LINEAR). Here, the Low-Energy Transmission Grating (LETG) was used. The dimness of the observed X-rays, and the extended nature of the emitting atmosphere meant that the grated spectra did not yield significant results. It is still possible to extract a spectrum based on the pulse-heights generated by each X-ray detection on the ACIS-S3 chip, although the morphology is not recorded. 6300 total counts were recorded for the pulse-height spectrum of the S3 chip in the 300 to 1000 eV range.

Solar wind. Comet WM1 was observed at the highest latitude available within this survey, and at a latitude of 34 degrees, it was far outside the HCS. During the observations, this comet might have experienced the southerly flank of the shock of a strong X3.4 flare at S20E97 and its ICME and shock on December 28, 2001 (FF#359) (McKenna-Lawlor et al., 2006).

153P/2002 (Ikeya–Zhang)

X-rays. The brightest X-ray comet in the Chandra archive is 153P/2002 (Ikeya–Zhang). The heliographic latitude, geocentric distance and heliocentric distance were comparable to those for comet C/1999 S4 (LINEAR), with a latitude of 26°, $\Delta = 0.457$ AU and $r_h = 0.8$ AU. Rather than periodically re-point the detector to track the comet, the pointing direction was fixed and the comet was monitored as it passed through the field of view, thus increasing the effective FoV. There were two observing periods on April 15th 2002, each lasting for approximately 3 hours and 15 minutes. In both periods, a strong cometary signal is detected on all of the activated ACIS-CCDs. Consequently, a background signal cannot be taken from the observation. A crescent shape on the Sun side of the comet is observed over all of the CCD array. Over 200 000 total counts were observed from the S3 chip in the 300 to

1000 eV range. The time intervals for each observing period are 11 570 and 11 813 seconds.

Solar wind. Like C/2000 WM1, this comet was observed at a relatively high heliographic latitude. Solar wind data obtained in the ecliptic plane can therefore not be used to determine the wind state at the comet. 153P/2002 (Ikeya–Zhang) was well-positioned during the first observation on 15 April 2002 for a flare at N16E05 (FF#388) on 12 April 2002. During the second observation on 16 April, there was an earlier flare on 14 April at N14W57, but this flare was probably too far to the west to be effective (McKenna-Lawlor et al., 2006). The comet was observed at a high latitude, and hence ACE solar wind data is most likely not applicable.

2P/2003 (Encke)

X-rays. The Chandra observation of Encke took place on the 24th of November 2003 (Lisse et al., 2005), when the comet had a heliocentric distance of $r_h = 0.891$ AU and a geocentric distance of $\Delta = 0.275$ AU and a heliographic latitude of 11.4 degrees. The comet was continuously tracked for over 15 hours, resulting in a useful exposure of 44 000 seconds. The ACIS-S3 CCD counted 6140 X-rays in the range 300–1000 eV.

The brightest point was offset from the nucleus by 11 000 km, dimming to 10% of this value at a distance of 60 000 km.

The ACIS-S1 CCD was not activated in this observation. The low quantum efficiency of the other activated CCDs below 0.5 keV makes them unsuitable as background references.
Solar wind. The proton velocity decreased during observations from 600 to 500 km s^{-1}. A flare on 20 November 2003, at N01W08 (FF#525), was well-positioned to affect the observations on 23 November (data from work in progress by Z.K. Smith et al.). The comet most likely interacted with the overexpanded, rarified plasma flow that followed the earlier hot shocked and compressed flow behind the flare's shock.

C/2001 Q4 (NEAT)

X-rays. A short observation of comet C/2001 Q4 was made on May 12 2004, when the geocentric and heliocentric distances were $\Delta = 0.362$ AU and $r_h = 0.964$ AU respectively. With a heliographic latitude of 3 degrees, the comet was almost in the ecliptic plane. From 3 pointings, the useful exposure was 10 328 seconds. The ACIS-S3 chip detected 6540 X-rays in between 300 and 1000 eV. The ACIS-S1 was used as a background signal.

Solar wind. There was no significant solar activity during the observations (Z.K. Smith et al., ibid.). From solar wind data, the comet interacted with a quiet, slow 352 km s^{-1} wind.

9P/2005 (Tempel 1)

X-rays. The observation of comet 9P/2005 (Tempel 1) was designed to coincide with the *Deep Impact* mission (Lisse et al., 2007). The allocated observation time of 291.6 ks was

split into 7 periods, starting on June 30th, July 4th (encompassing the Deep Impact collision), July 5th, July 8th, July 10th, July 13th and July 24th. The brightest observing periods were June 30th and July 8th. The focus here is on the June 30th observation. On this date, $r_h = 1.507$ AU and $\Delta = 0.872$ AU.

The useful exposure was 50 059 seconds, with a total of 7300 counts, 4000 from the June 30th flare alone, were detected in the energy range of 300–1000 eV.

The brightest point for the June 30th observation was located 11 000 km from the nucleus. The morphology appears to be more spherical than in other comet observations.

Solar wind. Observations were taken over a long time span covering different solar wind environments. There was no significant solar activity during the 30 June 2005 observations (Z.K. Smith et al., ibid. Lisse et al., 2007). From the ACE data, it can be seen that at June 30, the comet most likely interacted with a quiet, slow solar wind.

73P/2006 (Schwassmann–Wachmann 3B)

X-rays. The close approach of comet 73P/2006 (Schwassmann–Wachmann 3B) in May 2005 ($\Delta = 0.106$ AU, $r_h = 0.965$ AU) provided an opportunity to examine cometary X-rays in high spatial resolution. *Chandra* was one of several X-ray missions to focus on one of the large fragments of the comet. Between 300 and 1000 eV, 6285 counts were obtained in a useful exposure of 20 600 seconds.

Solar wind. There was a weak flare on 22 May 2006 (FF#655, Z.K. Smith, priv. comm.). A sequence of three high speed coronal hole streams passed the comet in the period around the observations and a corotating CIR might have reached the comet in association with the observations on 23 May, which is confirmed by the mapped solar wind data.

Dankwoord

Vijf jaar geleden stond ik voor de moeilijke keus of ik wilde afstuderen in de experimentele natuurkunde of in de sterrenkunde. Ronnie Hoekstra van de atoomfysicagroep had wel een suggestie: ladingsoverdracht in kometen. Xander Tielens, al eerder mijn begeleider bij mijn sterrenkundig klein onderzoek, was wel in voor een wild idee en was bereid dit onderzoek vanuit de sterrenkunde te begeleiden. Van kometen wisten we alledrie toendertijd overigens niets.

'Catching Some Sun' was uiteindelijk een ontzettend interessant afstudeerproject waarin ik al mijn energie kwijt kon. Het absolute hoogtepunt was voor mij de Oortworkshop in Leiden, georganiseerd door Ewine van Dishoeck ter ere van haar promotor Alex Dalgarno. Het onderwerp van deze bijeenkomst was 'X-rays in the Solar System' en het was mijn eerste kennismaking met de verschillende kopstukken in mijn vakgebied. Deze meeting in het bijzonder overtuigde mij ervan dat het onderzoek naar kometaire röntgenemissie nog lang niet af was.

Ik wil op deze plaats graag iedereen bedanken die op enige wijze heeft bijgedragen aan dit proefschrift en mijn onderzoek. Een aantal mensen wil ik hier in het bijzonder noemen.

Natuurlijk was het onderzoek nooit mogelijk geweest zonder mijn beide promotores, Ronnie Hoekstra en Xander Tielens. Vanaf het begin heb ik van hen veel ruimte gekregen om zelf vorm en richting te geven aan het onderzoek. Ronnie, mijn zelfverklaard 'microscopisch geweten', wil ik bedanken voor de steun, de aanmoedigingen en het vaak nodige afremmen. De belangrijkste lessen waren misschien dat koffie en bier zittend gedronken dienen te worden, en dat de weg vinden met behulp van de sterren niet weggelegd is voor astrofysici die denken in factoren tien. Xander stond de laatste tijd wat meer op de achtergrond, maar hielp daarmee juist dingen in perspectief te zien. Jouw wijze raad en kritische vragen waren onmisbaar, hoewel ik tijdens mijn onderzoek vaak de 'Wet van Tielens' verzuchtte (één uur gesprek met Xander = één week werk). Ook wil ik Ewine van Dishoeck, Reinhard Morgenstern en Bob McCullough danken voor de kritische lezing van mijn proefschrift.

Natuurlijk was mijn onderzoek niet zo leuk geweest zonder de atoomfysicagroep en haar vaste regels en gebruiken. Koffie om 10:00, lunchen om 12:00, weer koffie om 15:00. Ook de vele lange etentjes en lange avonden in binnen- en buitenland zorgden voor een

ontspannen atmosfeer waarbinnen we naar hartenlus konden kibbelen om bundeltijd. Ik wil jullie, Steven Knoop, Mirko Unipan, Fresia Alvarado, Sadia Bari, Zoltan Juhasz, Albert Mollema, Abel Robin, Thomas Schlathölter, Gabriel Hasan en Jos Postma dan ook graag bedanken voor de leuke tijd. In het bijzonder wil ik de studenten bedanken die gedurende mijn promotieperiode aan het experiment hebben meegewerkt, namelijk Ymkje Huismans en Judith Brouwer.

Experimenteel onderzoek is slechts mogelijk bij de gratie van velen. In de eerste plaats wil ik Otto Dermois bedanken voor het ontwikkelen van de ionenoptica waarmee het mogelijk werd ionen van de bron te vertragen tot typische zonnewindsnelheden. Met veel geduld heb je me dikwijls geholpen. Ook Jans Sijbring ben ik veel dank verschuldig. Ik ben er zeker van dat men jouw instant-oplossingen en geheime voorraden zal missen! Voor de technische ondersteuning en hulp wil graag de technische afdelingen van het KVI bedanken.

In the second year of my research, I suddenly got an email from the fouding father of my field, Casey Lisse. In response to my first article in ApJ he wrote, “Nice work, but can you do this for X-rays as well?". “Of course", I replied, and this resulted in a roller-coaster ride of X-ray observations. We have worked together on many different studies and you have introduced me to the world as well as the people of the planetary sciences, for which I am most thankful. I would like to thank all the colleagues and friends I have worked with the last years, Damian Christian, Konrad Dennerl, Murray Dryer, Martin Torney, Bob McCullough, Bohdan Seredyuk, Scott Wolk, Vasili Kharchenko, Alex Dalgarno, Peter Beiersdorfer, Greg Brown, Ron Elsner, Thomas Zurbuchen, and Geraint Jones. This thesis is build on our discussions and your critical ideas.

I would like to thank the different institutes and people that gave me the financial means for extensive travelling. Besides the KVI, I wish to acknowledge the Leids Kerkhoven-Bosscha foundation, NWO, SRON, as well as the host institutes of many of the colleagues mentioned above.

Het AGORA experiment is ondertussen afgekoppeld en een hele zwerm aasgieren heeft zich op de overblijfselen gestort. Toch heb ik een beetje een opvolger: Erwin, ik wens je veel succes bij je promotieonderzoek en hoop dat op de voorkant van je proefschrift een mooie trampolinefoto komt te staan. Mijn ouders wil ik graag bedanken voor alle steun en geduld en het simpele feit dat ze het voor mij mogelijk gemaakt hebben te studeren.

Tenslotte bedank ik Veerle, voor alles.

Groningen, Mei 2007

List of Publications

1. D. Bodewits, Z. Juhász, R. Hoekstra and A.G.G.M. Tielens, 2004, Catching Some Sun: Probing the Solar Wind with Cometary X-ray and Far-Ultraviolet Emission, *ApJ.Lett.* **606**: L81

2. D. Bodewits, R.W. McCullough, A.G.G.M. Tielens and R. Hoekstra, 2004, X-ray and Far-Ultraviolet Emission from Comets: Relevant Charge Exchange Processes., *Phys. Scr. C* **70**: 17

3. D. Bodewits, A.G.G.M. Tielens, R. Morgenstern and R. Hoekstra, 2005, Fingerprints of Charge Exchange between He^{2+} and Water Molecules, *NIMB*, **235**: 358

4. B. Seredyuk, R.W. McCullough, H. Tawara, H.B. Gilbody, D. Bodewits, R. Hoekstra, A.G.G.M. Tielens, P. Sobocinski, D. Pesic, R. Hellhammer, B. Sulik, N. Stolterfoht, O. Abu-Haija and E.Y. Kamber, 2005, Charge Exchange and Dissociative Processes in Collisions of Slow He^{2+} Ions with H_2O Molecules, *Phys. Rev. A* **71**: 022705

5. C.M. Lisse, D.J. Christian, K. Dennerl, S.J. Wolk, D. Bodewits, R. Hoekstra, M.R. Combi, T. Mäkinen, M. Dryer, C.D. Fry and H. Weaver, 2005, Chandra Observations of Comet 2P/Encke 2003: First Detection of a Collisionally Thin, Fast Solar Wind Charge Exchange System, *ApJ.*, **635**: 1329

6. D. Bodewits, R. Hoekstra, B. Seredyuk, R.W. McCullough, G.H. Jones and A.G.G.M. Tielens, 2006, Charge Exchange Emission from Solar Wind Helium Ions, *ApJ.*, **642**: 593

7. R. Hoekstra, D. Bodewits, S. Knoop, R. Morgenstern, L. Mendez, L.F. Errea, C. Illecas, A. Macias, B. Pons, A. Riera, F. Aumayr and HP. Winter, 2006, Charge exchange data for alpha particles interacting with atoms and molecules, *Atomic and Plasma-Material Interaction Data for Fusion*, in press

8. C.M. Lisse, D.J. Christian, S.J. Wolk, K. Dennerl, D. Bodewits, T.H. Zurbuchen, K.C. Hansen, R. Hoekstra, M. Combi, C.D. Fry, M. Dryer, T. Mäkinen, W. Sun, 2007, Chandra Observations of Comet 9P/Tempel 1 During the Deep Impact Campaign , *Icarus*, *in press*

9. D. Bodewits, D.J. Christian, M. Torney, M. Dryer, C.M. Lisse, K. Dennerl, T.H. Zurbuchen, S.J. Wolk, A.G.G.M. Tielens and R. Hoekstra, Spectral Analysis of the Chandra Comet Survey, *A&A, in press*

10. D. Bodewits & R. Hoekstra, Electron Capture Channels in Collisions between O^{6+} and H_2O, *in prep.*

11. S.J. Wolk, C.M. Lisse, D. Bodewits, D.J. Christian, and K. Dennerl, Chandra's Close Encounter with the Disintegrating Comet 73P/2006 (Schwassmann-Wachmann 3B), *in prep.*

References

Abramov, V. A., Baryshnikov, F. F., and Lisitsa, V. S.: 1978, *Soviet Journal of Experimental and Theoretical Physics Letters* **27**, 464

Abu-Haija, O., Kamber, E. Y., and Ferguson, S. M.: 2003, *NIMB* **205**, 634

A'Hearn, M. F.: 2005, *Science* **310**, 258

Ali, R., Neill, P. A., Beiersdorfer, P., Harris, C. L., Raković, M. J., Wang, J. G., Schultz, D. R., and Stancil, P. C.: 2005, *ApJ. Lett.* **629**, L125

Alvarado, F., Hoekstra, R., and Schlathölter, T.: 2005, *J. Phys. B* **38**, 4085

Anderson, H., von Hellermann, M., Hoekstra, R., Horton, L., Howman, A., Konig, R., Martin, R., Olson, R., and Summers, H.: 2000, *Plasma Phys. Controll. Fusion.* **40**, 781

Axford, W. and McKenzie, J.: 1997, *The Solar Wind*

Baede, A. P. M.: 1975, *Adv. in Chem. Phys.* **30**, 463

Beiersdorfer, P.: 2003, *ARA&A* **41**, 343

Beiersdorfer, P., Boyce, K. R., Brown, G. V., Chen, H., Kahn, S. M., Kelley, R. L., May, M., Olson, R. E., Porter, F. S., Stahle, C. K., and Tillotson, W. A.: 2003, *Science* **300**, 1558

Beiersdorfer, P., Lisse, C. M., Olson, R. E., Brown, G. V., and Chen, H.: 2001, *ApJ. Lett.* **549**, L147

Beijers, J. P. M., Hoekstra, R., and Morgenstern, R.: 1996, *J. Phys. B* **29**, 1397

Beijers, J. P. M., Hoekstra, R., Schlatmann, A. R., Morgenstern, R., and de Heer, F. J.: 1992, *J. Phys. B* **25**, 463

Biermann, L.: 1951, *Zeitschrift fur Astrophysik* **29**, 274

Bingham, R., Dawson, J. M., Shapiro, V. D., Mendis, D. A., and Kellet, B. J.: 1997, *Science* **275**, 49

Biver, N., Bockelee-Morvan, D., Colom, P., Crovisier, J., Davies, J. K., Dent, W. R. F., Despois,

D., Gerard, E., Lellouch, E., Rauer, H., Moreno, R., and Paubert, G.: 1997, *Science* **275**, 1915

Biver, N., Bockelée-Morvan, D., Crovisier, J., Davies, J. K., Matthews, H. E., Wink, J. E., Rauer, H., Colom, P., Dent, W. R. F., Despois, D., Moreno, R., Paubert, G., Jewitt, D., and Senay, M.: 1999, *AJ* **118**, 1850

Biver, N., Bockelée-Morvan, D., Crovisier, J., Lis, D. C., Moreno, R., Colom, P., Henry, F., Herpin, F., Paubert, G., and Womack, M.: 2006, *A&A* **449**, 1255

Bliek, F. W., Woestenenk, G. R., Hoekstra, R., and Morgenstern, R.: 1998, *Phys. Rev. A* **57**, 221

Bockelée-Morvan, D., Biver, N., Moreno, R., Colom, P., Crovisier, J., Gérard, É., Henry, F., Lis, D. C., Matthews, H., Weaver, H. A., Womack, M., and Festou, M. C.: 2001, *Science* **292**, 1339

Bodewits, D., Hoekstra, R., Seredyuk, B., McCullough, R. W., Jones, G. H., and Tielens, A. G. G. M.: 2006, *ApJ* **642**, 593

Bodewits, D., Juhász, Z., Hoekstra, R., and Tielens, A. G. G. M.: 2004, *ApJ. Lett.* **606**, L81

Bodewits, D., Tielens, A. G. G. M., Morgenstern, R., and Hoekstra, R.: 2005, *NIMB* **235**, 358

Bohr, N. and Lindhard, K.: 1954, *K. Dan. Vidensk. Selsk. Mat. Fys. Medd.* **28**, 1

Brown, G. V., Bodewits, D., Willingale, R., Porter, F. S., and Beiersdorfer, P.: in prep.

Burgdörfer, J., Morgenstern, R., and Niehaus, A.: 1986, *J. Phys. B* **19**, L507

Cadez, I., Greenwood, J. B., Chutjian, A., Mawhorter, R. J., Smith, S. J., and Niimura, M.: 2002, *J. Phys.B.* **35**, 2515

Combi, M. R., Harris, W. M., and Smyth, W. H.: 2004, *Comets II* p. 523

Cravens, T. E.: 1997, *Geophys. Res. Lett.* **24**, 105

dello Russo, N., Disanti, M. A., Magee-Sauer, K., Gibb, E. L., Mumma, M. J., Barber, R. J., and Tennyson, J.: 2004, *Icarus* **168**, 186

Dennerl, K., Englhauser, J., and Trümper, J.: 1997, *Science* **277**, 1625

Dennerl, K., Lisse, C. M., Bhardwaj, A., Burwitz, V., Englhauser, J., Gunell, H., Holmström, M., Jansen, F., Kharchenko, V., and Rodríguez-Pascual, P. M.: 2006, *A&A* **451**, 709

Dere, K. P., Landi, E., Mason, H. E., Monsignori Fossi, B. C., and Young, P. R.: 1997, *Astron. Astrop. Suppl.* **125**, 149

Dijkkamp, D., Ciric, D., de Boer, A., de Heer, F. J., and Vlieg, E.: 1985, *J. Phys. B* **18**, 4763

Dones, L., Weissman, P. R., Levison, H. F., and Duncan, M. J.: 2004, *Comets II* p. 153

Drake, G. W.: 1988, *Can. J. Phys.* **66**, 586

Drentje, A. G.: 1985, *NIMB* **9**, 526

Dryer, M., Fry, C. D., Sun, W., Deehr, C., Smith, Z., Akasofu, S.-I., and Andrews, M. D.: 2001, *Sol. Phys.* **204**, 265

Errea, L. F., Illescas, C., Méndez, L., Pons, B., Riera, A., and Suárez, J.: 2004, *J. Phys.B.* **37**, 4323

Farnham, T. L., Schleicher, D. G., Woodney, L. M., Birch, P. V., Eberhardy, C. A., and Levy, L.: 2001, *Science* **292**, 1348

Festou, M. C.: 1981, *A&A* **95**, 69

Forsyth, R. J., Balogh, A., Smith, E. J., and Gosling, J. T.: 1997, *Geophys. Res. Lett.* **24**, 3101

Friedel, D. N., Remijan, A. J., Snyder, L. E., A'Hearn, M. F., Blake, G. A., de Pater, I., Dickel, H. R., Forster, J. R., Hogerheijde, M. R., Kraybill, C., Looney, L. W., Palmer, P., and Wright, M. C. H.: 2005, *ApJ* **630**, 623

Fritsch, W. and Lin, C. D.: 1984, *Phys. Rev. A* **29**, 3039

Fritsch, W. and Lin, C. D.: 1986, *J. Phys. B* **19**, 2683

Fritsch, W. and Lin, C. D.: 1991, *Phys. Rep.* **202**, 1

Fry, C. D., Dryer, M., Smith, Z., Sun, W., Deehr, C. S., and Akasofu, S.-I.: 2003, *J. Geophys. Res.* **108**, 5

Fuselier, S. A., Shelley, E. G., Goldstein, B. E., Goldstein, R., Neugebauer, M., Ip, W.-H., Balsiger, H., and Reme, H.: 1991, *ApJ* **379**, 734

Gabriel, A. H. and Jordan, C.: 1969, *MNRAS* **145**, 241

Garcia, J. D. and Mack, J. E.: 1965, *J. Opt. Soc. Am.* **55**, 654

Geiss, J., Gloeckler, G., von Steiger, R., Balsiger, H., Fisk, L. A., Galvin, A. B., Ipavich, F. M., Livi, S., McKenzie, J. F., Ogilvie, K. W., and Wilken, B.: 1995, *Science* **268**, 1033

Goldstein, B. E., Neugebauer, M., Balsiger, H., Drake, J., Fuselier, S. A., Goldstein, R., Ip, W. H., Rettenmund, U., Rosenbauer, H., Schwenn, R., and Shelley, E. G.: 1987, *A&A* **187**, 174

Green, T. A., Shipsey, E. J., and Browne, J. C.: 1982, *Phys. Rev. A* **25**, 1364

Greenwood, J. B., Mawhorter, R. J., Cadez, I., Lozano, J., Smith, S. J., and Chutjian, A.: 2004, *Physica Scripta* **110**, 358

Greenwood, J. B., Williams, I. D., Smith, S. J., and Chutjian, A.: 2000, *ApJ. Lett.* **533**, L175

Greenwood, J. B., Williams, I. D., Smith, S. J., and Chutjian, A.: 2001, *Phys. Rev. A* **63(6)**, 062707

Haberli, R. M., Gombosi, T. I., DeZeeuw, D. L., Combi, M. R., and Powell, K. G.: 1997, *Science* **276**, 939

Hasan, A. A., Eissa, F., Ali, R., Schultz, D. R., and Stancil, P. C.: 2001, *ApJ. Lett.* **560**, L201

Haser, L.: 1957, *Bulletin de la Societe Royale des Sciences de Liege* **43**, 740

Hodgkinson, J. M., McLaughlin, T. K., McCullough, R. W., Geddes, J., and Gilbody, H. B.: 1995, *J. Phys.B.* **28**, L393

Hoekstra, R., Anderson, H., Bliek, F. W., von Hellermann, M., Maggi, C. F., Olson, R. E., and Summers, H. P.: 1998, *Plasma Phys. Controll. Fusion.* **40**, 1541

Hoekstra, R., Beijers, J. P. M., Schlatmann, A. R., Morgenstern, R., and de Heer, F. J.: 1990, *Phys. Rev. A* **41**, 4800

Hoekstra, R., de Heer, F. J., and Morgenstern, R.: 1991, *J. Phys.B.* **24**, 4025

Hoekstra, R., Folkerts, H. O., Beijers, J. P. M., Morgenstern, R., and de Heer, F. J.: 1994, *J. Phys.B.* **27**, 2021

Hoekstra, R., Čirič, D., de Heer, F. J., and Morgenstern, R.: 1989, *Physica Scripta Volume T* **28**, 81

Huebner, W. F., Keady, J. J., and Lyon, S. P.: 1992, *Ap&SS* **195**, 1

Hundhausen, A. J., Gilbert, H. E., and Bame, S. J.: 1968, *ApJ. Lett* **152**, L3

Ishii, K., Okuno, K., and Kobayahi, N.: 2002, *Physica Scripta* p. 176

Isler, R. C.: 1994, *Plasma Physics and Controlled Fusion* **36**, 171

Janev, R. K., Belic, D. S., and Bransden, B. H.: 1983, *Phys. Rev. A* **28**, 1293

Janev, R. K. and Winter, H.: 1985, *Phys. Rep.* **117**, 265

Juhász, Z.: 2004, *Ph.D. thesis*, Rijks*universiteit* Groningen

Kamber, E. Y., Abu-Haija, O., and Ferguson, S. M.: 2002, *Phys. Rev. A* **65(6)**, 062717

Kearns, D. M., Gillen, D. R., Voulot, D., Greenwood, J. B., McCullough, R. W., and Gilbody, H. B.: 2001, *J. Phys.B.* **34**, 3401

Kearns, D. M., McCullough, R. W., and Gilbody, H. B.: 2002, *J. Phys. B* **35**, 4335

Kearns, D. M., McCullough, R. W., Trassl, R., and Gilbody, H. B.: 2003, *J. Phys. B* **36**, 3653

Keller, H. U., Arpigny, C., Barbieri, C., Bonnet, R. M., Cazes, S., Coradini, M., Cosmovici, C. B., Delamere, W. A., Huebner, W. F., Hughes, D. W., Jamar, C., Malaise, D., Reitsema, H. J., Schmidt, H. U., Schmidt, W. K. H., Seige, P., Whipple, F. L., and Wilhelm, K.: 1986, *Nature* **321**, 320

Kharchenko, V. and Dalgarno, A.: 2000, *J. Geophys. Res.* **105**, 18351

Kharchenko, V. and Dalgarno, A.: 2001, *ApJ. Lett.* **554**, L99

Kharchenko, V., Liu, W., and Dalgarno, A.: 1998, *J. Geophys. Res.* **103**, 26687

Knoop, S., Hasan, V. G., Morgenstern, R., and Hoekstra, R.: 2006, *Europhysics Letters* **74**, 992

Knoop, S., Keim, M., Lüdde, H. J., Kirchner, T., Morgenstern, R., and Hoekstra, R.: 2005, *J. Phys. B* **38**, 3163

Krasnopolsky, V.: 1997, *Icarus* **128**, 368

Krasnopolsky, V. A.: 2004, *Icarus* **167**, 417

Krasnopolsky, V. A.: 2006, *J. Geophys. Res.* **111**, 12102

Krasnopolsky, V. A., Christian, D. J., Kharchenko, V., Dalgarno, A., Wolk, S. J., Lisse, C. M., and Stern, S. A.: 2002, *Icarus* **160**, 437

Krasnopolsky, V. A., Greenwood, J. B., and Stancil, P. C.: 2004, *Space Science Reviews* **113**, 271

Krasnopolsky, V. A. and Mumma, M. J.: 2001, *ApJ* **549**, 629

Krasnopolsky, V. A., Mumma, M. J., Abbott, M., Flynn, B. C., Meech, K. J., Yeomans, D. K., Feldman, P. D., and Cosmovici, C. B.: 1997, *Science* **277**, 1488

Kuiper, G. P.: 1951, in J. A. Hynek (ed.), *Proceedings of a topical symposium, commemorating the 50th anniversary of the Yerkes Observatory and half a century of progress in astrophysics, New York: McGraw-Hill, 1951, edited by Hynek, J.A., p.357*, p. 357

Landi, E., Del Zanna, G., Young, P. R., Dere, K. P., Mason, H. E., and Landini, M.: 2006, *Ap J. Supp.* **162**, 261

Lepri, S. T. and Zurbuchen, T. H.: 2004, *J. Geophys. Res.* **109**, 1112

Lisse, C. M., Bodewits, D., Christian, D. J., Wolk, S. J., Dennerl, K., Zurbuchen, T. H., Hansen, K. C., Hoekstra, R., Combi, M., Fry, C. D., Dryer, M., Mäkinen, T., and Sun, W.: 2007, *Icarus* in press

Lisse, C. M., Christian, D. J., Dennerl, K., Meech, K. J., Petre, R., Weaver, H. A., and Wolk, S. J.: 2001, *Science* **292**, 1343

Lisse, C. M., Christian, D. J., Dennerl, K., Wolk, S. J., Bodewits, D., Hoekstra, R., Combi, M. R., Mäkinen, T., Dryer, M., Fry, C. D., and Weaver, H.: 2005, *ApJ* **635**, 1329

Lisse, C. M., Cravens, T. E., and Dennerl, K.: 2004, *Comets II* p. 631

Lisse, C. M., Dennerl, K., Englhauser, J., Harden, M., Marshall, F. E., Mumma, M. J., Petre, R., Pye, J. P., Ricketts, M. J., Schmitt, J., Trumper, J., and West, R. G.: 1996, *Science* **274**, 205

Liu, W. and Schultz, D. R.: 1999, *Ap.J.* **526**, 538

Lubinski, G., Juhász, Z., Morgenstern, R., and Hoekstra, R.: 2000, *J. Phys. B* **33**, 5275

Lubinski, G., Juhász, Z., Morgenstern, R., and Hoekstra, R.: 2001, *Phys. Rev. Lett.* **86**, 616

Marsden, B.G. and Williams, G.V.: 2005, *Catalogue of Cometary Orbits 2005*, Cambridge: Smithson. Astrophys. Obs., xx-th edition

Mawhorter, Chutjian, A., Cravens, T., Djuric, N., Hossain, S., Lisse, C., MacAskill, J., Smith, S. J., and Williams, I.: 2007, *Phys. Rev. A* 75

Mazzotta, P., Mazzitelli, G., Colafrancesco, S., and Vittorio, N.: 1998, *A&AS* **133**, 403

McCullough, R. W., McLaughlin, T. K., Koizumi, T., and Gilbody, H. B.: 1992, *J. Phys. B* **25**, L193

McKenna-Lawlor, S. M. P., Dryer, M., Kartalev, M. D., Smith, Z., Fry, C. D., Sun, W., Deehr, C. S., Kecskemety, K., and Kudela, K.: 2006, *J. Geophys. Res.* **111**, 11103

Mumma, M. J., Dello Russo, N., DiSanti, M. A., Magee-Sauer, K., Novak, R. E., Brittain, S., Rettig, T., McLean, I. S., Reuter, D. C., and Xu, L.-H.: 2001, *Science* **292**, 1334

Mumma, M. J., DiSanti, M. A., Magee-Sauer, K., Bonev, B. P., Villanueva, G. L., Kawakita, H., Dello Russo, N., Gibb, E. L., Blake, G. A., Lyke, J. E., Campbell, R. D., Aycock, J., Conrad, A., and Hill, G. M.: 2005, *Science* **310**, 270

Mumma, M. J., Krasnopolsky, V. A., and Abbott, M. J.: 1997, *ApJ. Lett.* **491**, L125

Neubauer, F. M., Glassmeier, K. H., Pohl, M., Raeder, J., Acuna, M. H., Burlaga, L. F., Ness, N. F., Musmann, G., Mariani, F., Wallis, M. K., Ungstrup, E., and Schmidt, H. U.: 1986, *Nature* **321**, 352

Neugebauer, M., Cravens, T. E., Lisse, C. M., Ipavich, F. M., Christian, D., von Steiger, R., Bochsler, P., Shah, P. D., and Armstrong, T. P.: 2000, *J. Geophys. Res.* **105**, 20949

Neugebauer, M., Forsyth, R. J., Galvin, A. B., Harvey, K. L., Hoeksema, J. T., Lazarus, A. J., Lepping, R. P., Linker, J. A., Mikic, Z., Steinberg, J. T., von Steiger, R., Wang, Y.-M., and Wimmer-Schweingruber, R. F.: 1998, *J. Geophys. Res.* **103**, 14587

Niehaus, A.: 1986, *J. Phys.B.* **19**, 2925

Northrop, T. G., Lisse, C. M., Mumma, M. J., and Desch, M. D.: 1997, *Icarus* **127**, 246

Oort, J. H.: 1950, *Bull. Astron. Inst. Ned.* **11**, 91

Otranto, S., Olson, R. E., and Beiersdorfer, P.: 2006, *Phys. Rev. A* **73(2)**, 022723

Owens, A., Parmar, A. N., Oosterbroek, T., Orr, A., Antonelli, L. A., Fiore, F., Schultz, R., Tozzi, G. P., Maccarone, M. C., and Piro, L.: 1998, *ApJ. Lett.* **493**, L47

Pepino, R., Kharchenko, V., Dalgarno, A., and Lallement, R.: 2004, *ApJ.* **617**, 1347

Porquet, D. and Dubau, J.: 2000, *A&AS* **143**, 495

Porquet, D., Mewe, R., Dubau, J., Raassen, A. J. J., and Kaastra, J. S.: 2001, *A&A* **376**, 1113

Robrade, J. and Schmitt, J. H. M. M.: 2006, *A&A* **449**, 737

Rudd, M. E., Goffe, T. V., and Itoh, A.: 1985a, *Phys. Rev. A* **32**, 2128

Rudd, M. E., Goffe, T. V., Itoh, A., and Dubois, R. D.: 1985b, *Phys. Rev. A* **32**, 829

Rudd, M. E., Itoh, A., and Goffe, T. V.: 1985c, *Phys. Rev. A* **32**, 2499

Ryufuku, H., Sasaki, K., and Watanabe, T.: 1980, *Phys. Rev. A* **21**, 745

Savukov, I. M., Johnson, W. R., and Safronova, U. I.: 2003, *Atomic Data and Nuclear Data Tables* **85**, 83

Schlathölter, T., Alvarado, F., Bari, S., and Hoekstra, R.: 2006, *Phys. Scr.* **73**, 113

Schleicher, D.: 2001, *IAU Circ.* **7558**, 2

Schleicher, D. G., Barnes, K. L., and Baugh, N. F.: 2006, *AJ* **131**, 1130

Schleicher, D. G., Woodney, L. M., and Birch, P. V.: 2002, *Earth Moon and Planets* **90**, 401

Schmidt, H. U. and Wegmann, R.: 1982, in L. L. Wilkening (ed.), *IAU Colloq. 61: Comet Discoveries, Statistics, and Observational Selection*, p. 538

Schulz, R., Stüwe, J. A., Tozzi, G. P., and Owens, A.: 2000, *A&A* **361**, 359

Schwadron, N. A. and Cravens, T. E.: 2000, *ApJ* **544**, 558

Seredyuk, B., McCullough, R., Tawara, H., Gilbody, H., Bodewits, D., Hoekstra, R., Tielens, A., Sobocinski, P., Pesic, D., Hellhammer, R., Sulik, B., Stolterfoht, N., Abu-Haija, O., and Kamber, E.: 2005a, *Phys. Rev. A* **71(2)**, 022705

Seredyuk, B., McCullough, R. W., and Gilbody, H. B.: 2005b, *Phys. Rev. A* **71(2)**, 022713

Seredyuk, B., McCullough, R. W., and Gilbody, H. B.: 2005c, *Phys. Rev. A* **72(2)**, 022710

Shah, M. B. and Gilbody, H. B.: 1974, *J. Phys.B.* **7**, 630

Shah, M. B. and Gilbody, H. B.: 1978, *J. Phys.B.* **11**, 121

Shimakura, N., Sato, H., Kimura, M., and Watanabe, T.: 1987, *J. Phys. B* **20**, 1801

Shipsey, E. J., Green, T. A., and Browne, J. C.: 1983, *Phys. Rev. A* **27**, 821

Smith, Z., Dryer, M., Ort, E., and Murtagh, W.: 2000, *J. Atm. Ter. Phys.* **62**, 1265

Snow, M., Brandt, J. C., Yi, Y., Petersen, C. C., and Mikuz, H.: 2004, *Planet. Space Sci.* **52**, 313

Snowden, S. L., Collier, M. R., and Kuntz, K. D.: 2004, *ApJ* **610**, 1182

Stancil, P. C., Zygelman, B., Clarke, N. J., and Cooper, D. L.: 1997, *Phys. Rev. A* **55**, 1064

Stern, S. A.: 2003, *Nature* **424**, 639

Sunshine, J. M. e. a.: 2006, *Science* **311**, 1453

Suraud, M. G., Hoekstra, R., de Heer, F. J., Bonnet, J. J., and Morgenstern, R.: 1991, *J. Phys.B.* **24**, 2543

Thompson, W. R., Shah, M. B., and Gilbody, H. B.: 1996a, *J. Phys. B* **29**, 2847

Thompson, W. R., Shah, M. B., and Gilbody, H. B.: 1996b, *J. Phys. B* **29**, 725

Turkstra, J. W., Hoekstra, R., Knoop, S., Meyer, D., Morgenstern, R., and Olson, R. E.: 2001, *Phys. Rev. Lett.* **87(12)**, 123202

Uchida, M., Morikawa, M., Kubotani, H., and Mouri, H.: 1998, *ApJ* **498**, 863

Vainshtein, L. A. and Safronova, U. I.: 1985, *Phys. Scr.* 31(519)

von Hellermann, M., Mandl, W., Summers, H. P., Boileau, A., Hoekstra, R., de Heer, F. J., and Frieling, G. J.: 1991, *Plasma Phys. Controll. Fusion.* **33**, 1805 1

von Steiger, R., Schwadron, N. A., Fisk, L. A., Geiss, J., Gloeckler, G., Hefti, S., Wilken, B., Wimmer-Schweingruber, R. F., and Zurbuchen, T. H.: 2000, *J. Geophys. Res.* **105**, 27217

Waite, Jr., J. H., Bagenal, F., Seward, F., Na, C., Gladstone, G. R., Cravens, T. E., Hurley, K. C., Clarke, J. T., Elsner, R., and Stern, S. A.: 1994, *J. Geophys. Res.* **99**, 14799

Wang, J. G., Turner, A. R., Cooper, D. L., Schultz, D. R., Rakovic, M. J., Fritsch, W., Stancil, P. C., and Zygelman, B.: 2002, *J. Phys. B* **35**, 3137

Weaver, H. A., Feldman, P. D., Combi, M. R., Krasnopolsky, V., Lisse, C. M., and Shemansky, D. E.: 2002, *ApJ. Lett.* **576**, L95

Wegmann, R. and Dennerl, K.: 2005, *A&A* **430**, L33

Wegmann, R., Dennerl, K., and Lisse, C. M.: 2004, *A&A* **428**, 647

Wegmann, R., Schmidt, H. U., Lisse, C. M., Dennerl, K., and Englhauser, J.: 1998, *Planet. Space Sci.* **46**, 603

Wickramasinghe, N. C. and Hoyle, F.: 1996, *Astroph. Space Sci.* **239**, 121

Willingale, R., O'Brien, P. T., Cowley, S. W. H., Jones, G. H., McComas, D. J., Mason, K. O., Osborne, J. P., Wells, A., Chester, M., Hunsberger, S., Burrows, D. N., Gehrels, N., Nousek, J. A., Angelini, L., Cominsky, L. R., Snowden, S. L., and Chincarini, G.: 2006, *ApJ* **649**, 541

Zurbuchen, T. H., Fisk, L. A., Gloeckler, G., and von Steiger, R.: 2002, *Geophys. Res. Lett.* **29**, 66

Zurbuchen, T. H. and Richardson, I. G.: 2006, *Space Science Reviews* p. 55